MATERIAL PRE-STRAINING EFFECTS ON FATIGUE AND FRACTURE BEHAVIOUR OF OFFSHORE WIND MONOPILE STRUCTURES

Thesis for the Degree of Engineering Doctorate in Renewable Energy Marine Structures (REMS)

by

SATYA GAYATHRI ANANDAVIJAYAN

October 2021

School of Water, Energy and Environment

Supervisors: Dr Ali Mehmanparast & Professor Feargal Brennan

Abstract

An important issue to be considered in the structural integrity assessment of offshore wind monopile structures is the influence of material pre-straining on the fracture toughness and fatigue crack initiation and growth behaviour of the material. Material pre-straining can be introduced into monopile cans during the three-roll bending fabrication process. Literature has shown that in certain steels, this pre-straining effect can affect the behaviour of the material, causing it to behave differently to the parent material. A finite element model has been developed to predict the level of plastic strain present in the material after undergoing the three-roll bending process, with a parametric study conducted to determine the effects of fabrication and geometry factors on plastic strain, which may potentially aid fabricators to control the behaviour of the material when in operation. Thus, the main aim of this project is to investigate the effects of material pre-conditioning on the mechanical response, fatigue, and fracture behaviour of an offshore structural steel. S355 steel which is widely used in offshore wind industry for foundation structures such as monopiles has been used in the experimental test programme involving specimens pre-tensioned to 0%, 5% and 10% to investigate the potentially beneficial or detrimental effects. In addition to this, an experimental study on the effect of fatigue damage on the mechanical properties of S355, across varying levels of pre-straining, has been conducted. The results from this study have been employed in the remaining life analysis of monopile structures, such as failure assessment diagrams, to determine appropriate inspection intervals and recommendations necessary to avoid catastrophic failure.

EngD Researcher: Satya Gayathri Anandavijayan

Principal Supervisor: Dr. Ali Mehmanparast

Co-supervisor: Prof. Feargal Brennan

Acknowledgements

I would like to express my sincere gratitude to my supervisor Dr Ali Mehmanparast for his continuous guidance, motivation, and constructive feedback over the duration of this EngD. Without his consistent enthusiasm, passion, and push to see the results of this project I would have found it very difficult to finish this thesis in this current global pandemic.

I would like to extend my thanks to Prof. Feargal Brennan for his support, knowledge, and perspective throughout this project. Being a part of the REMS CDT programme has taught me so much more than just technical knowledge and has equipped me with skills I will take forward throughout my career and life.

A special thanks to Dr Amir Chahardehi of Atkins for his constructive comments, feedback, and invaluable industrial insight. Without his patience and commitment to this project I would have struggled to understand the relevance of the project outside an academic setting.

I would also like to extend my appreciation to Jarryd Braithwaite for his invaluable help, support, and training during the experimental phase of this project. His dedication to the Structural Integrity lab has been vital.

Above all, I am sincerely grateful to my friends and family who have supported me during the good and bad times. Without their words of encouragement and unwavering support over the years I may not have been able to reach the end. A special thanks to my brothers for their constant reassurance and continuous belief over the past four years, even if I made life very difficult for them. Last but not least, I would like to thank my parents and grandparents for raising me to fulfil my potential, and for developing my curiosity and thirst for knowledge which I have carried on to my adult years. Without them I do not think I would have been able to start or complete this doctorate.

Table of Contents

List of Figures:

List of Tables:

List of Equations:

List of Symbols

a	Crack length
a_0	Initial crack length before pre-cracking
a_i	Crack length after pre-cracking
a_f	Final crack length after fracture toughness testing
Δa	Increment of crack growth
Δa_{max}	Maximum allowable crack extension in fracture toughness tests
B	Specimen thickness
B_e	Effective thickness
B_n	Specimen net thickness between side grooves
b_0	Uncracked ligament, (W-a_0)
C_0	Unloading compliance
C	Paris constant C
c	Length of plate
d	deflection
D	Fatigue damage
E_M	Effective Young's modulus
f	Frequency
G	Griffith's energy release rate
H	C(T) specimen height
J_e	J-integral
J_{el}	Value of J using elastic analysis
Jp_l	Value of J using plastic analysis
K_{Lmax}	Maximum curvature
K^*_L	Residual curvature
K_r	Fracture ratio
K_I	Stress intensity factor
K_{IC}	Fracture toughness taking into account ductile tearing
K_{max}	Stress intensity factor at maximum load
K_{min}	Stress intensity factor at minimum load

ΔK	Stress intensity factor range
L_r	Load ratio
m	Paris constant m
M_{max}	Maximum bending moment
N	Number of fatigue cycles
N_f	Number of cycles to failure in uniaxial fatigue tests
P_{max}	Maximum Load
P_{min}	Minimum Load
R	Load ratio in fatigue tests (P_{max}/P_{min})
t	Monopile thickness
U	Area under P vs LLD curve
Y	Shape function
W	Specimen width
η	Factor relating J to load and displacement measurements
$\sigma_{0.2}$	0.2 % proof stress
σ_{UTS}	Ultimate tensile stress
σ_y	Yield stress
$\Delta\sigma$	Stress range
$\sigma\|_0$	yield stress
σ_{max}	Maximum stress
σ_{min}	Minimum stress
σ_{ref}	Reference stress
σ_{true}	True stress
ε_f	Tensile strain at failure
ε_p	Plastic strain
$\varepsilon_{plastic}$	Plastic strain
$\varepsilon_{elastic}$	Elastic strain
ε_{true}	True strain
$\varepsilon_{pl,true}$	True plastic strain
ξ	Ratio of maximum bending moment to maximum elastic moment

μ	Poisson's ratio
γ	material coefficient

1. Introduction

1.1 Background and Motivation

Climate change is a serious global issue, compelling many governments to explore cleaner energy alternatives. The EU aims for Europe to reach 240GW of offshore wind capacity by 2030, with the UK aiming to power all homes via offshore wind by 2030 (1–5). In 2019, wind energy became the UK's second leading source of electricity, with clear yearly growth being recorded (6). Despite a pandemic, the global offshore wind capacity has increased by 15% in 2020, with an expected 37% growth in the year 2021 (7). With the industry growing at such exponential rates, manufacturers such as Siemens have been considering the production of offshore turbines as large as 14MW to account for this demand (8). This push for offshore wind has resulted in the offshore wind industry developing newer technologies and installing more wind farms of higher capacities in deeper waters (9). As these capacities increase, there is a need for larger foundation structures, with 10MW turbines and XXL monopiles potentially becoming more mainstream in the future (10). With foundation structures of offshore wind farms accounting for 25% of the overall costs, there is a need to adopt less conservative solutions to reduce the overall costs (11). New research led by Orsted has shown that the over conservativeness in the design of monopile structures, due to the use of outdated offshore oil and gas methods, has led to rising monopile costs, and thus more accurate design methods could cut the overall costs by up to 30% (12).

There are many different types of foundation structures available, each tailored for the individual water depth and location of the wind farm. One of the most commonly used foundation structures in offshore wind farms, especially in Europe, are monopile structures – due to their ease of production and simple design, leading to lower unit costs, while not sacrificing performance (13). The monopile structure consists of a single cylindrical steel pile, which is driven into the seabed. Monopiles are fabricated via the three-roll bending process; a cold forming process which involves plastically deforming hot rolled structural steel plates to form cylindrical "cans", before being longitudinally welded shut. These cans are then welded together circumferentially to the desired length required. Considering the shallower waters and economical feasibility of monopiles, it is

of no wonder that 91% of European offshore wind farms in 2014 have adopted this type of foundation structure (14).

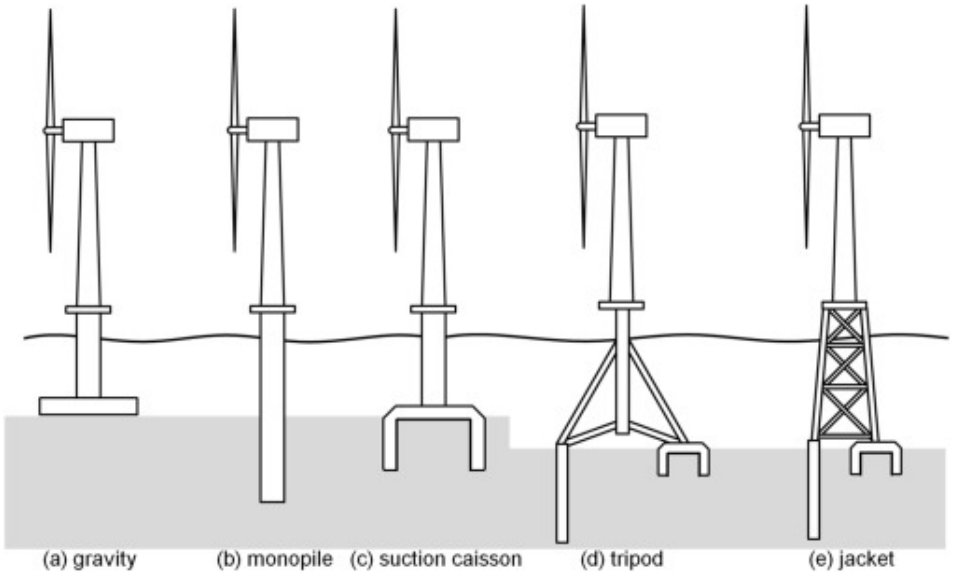

Figure 1 – Offshore wind foundation structures (15)

1.2 Problem Statement

Literature has shown that material pre-straining in materials can result in behavioural changes in its mechanical, fracture, and fatigue behaviour. Material pre-straining can be introduced into materials during fabrication processes such as bending and rolling, which induce plastic deformation and thus plasticity into the material. In the offshore wind industry, S355 structural steel is commonly used for offshore structures such as monopiles for offshore wind turbine foundation structures.

Material data used in the design and lifetime expectancy and fitness for service assessments are based on base metal. Since the material would have undergone considerable pre-straining effects prior to installation and service, the material properties would be altered and thus all prior calculations may be considered moot. Foundation structures are considered as critical components as they cannot be easily replaced compared to other components, and therefore the cost implications are high. Although these are designed for 25 years of service, such components can fail due to fatigue, cracking, and fault conditions (16,17). Therefore, it is of utmost importance to understand the behaviour of S355 structural steel post fabrication, in order to accurately predict fatigue and fracture of the monopile structures.

1.3 Aims and Objectives

The main aim of this study is to investigate the impact of fabrication processes on the life assessment of offshore wind monopile structures. To achieve this, the effects of material pre-strain on the mechanical response, fatigue, and fracture behaviour of S355 (an offshore structural steel) will be investigated.

The objectives of this thesis are:

- To determine the influence of material pre-straining on the fracture toughness, mechanical properties, fatigue crack growth, and S-N fatigue (in air)
- To determine the influence of fatigue damage on mechanical properties of S355
- To develop and validate finite element models to predict plastic pre-strain for monopiles
- To employ the obtained understanding of material pre-straining effects in engineering critical assessments of renewable energy marine structures

1.4 Structure of Thesis

The structure of this thesis has been laid out in the format of a portfolio of published and/or pending peer reviewed papers. The thesis will start with a brief literature review (chapter 2) to highlight and summarise the theoretical background relevant to fracture and fatigue; the current work which has been studied by previous researchers thus far; and identifying the gaps in knowledge which will be filled by the work in this present study. Each chapter is prefaced with a short literature review to highlight previous work and methodologies relevant to the study of each chapter, with references presented at the end of each chapter.

An overall discussion collating all experimental test result outcomes has been presented in chapter 3, with recommendations for future work. The conclusions from this study and the contributions to knowledge have been outlined in chapter 4.

Chapter 5 presents the numerical finite element work undertaken to predict plastic pre-straining levels during the fabrication of monopile structures. All methodology, results and discussion have been presented. This publication highlights that material pre-straining is induced during forming, and the effects of various configurations and fabrication factors on the level of pre-straining present.

Experimental test result methodologies, results and analysis and discussion have been presented in chapters 6 and 7. Chapter 6 focuses on material pre-straining effects on the mechanical and fracture toughness properties of S355. Tensile and fracture toughness test results on pre-tensioned S355 have been presented and compared to results for as received base metal. Material pre-straining effects on the fatigue properties of S355 have been investigated in chapter 7. Uniaxial fatigue, fatigue crack growth, and fatigue damage testing have been conducted on 0%, 5% and 10% pre-strained specimens and experimental test results have been compared to determine the consequences of the monopile fabrication process.

The results from the previous experimental test results in chapters 6 and 7 have been used as the basis of relevant engineering critical assessments from BS7910, and the outcomes of these have been presented in chapter 8. Comparisons have been made to fitness for service assessment results using test data from the present study as well as the SLIC interlaboratory testing programme derived from literature.

Appendices have been included at the end of the thesis. All test matrices for numerical and experimental work, specimen geometries and pre-straining conditions have been provided. R curves from fracture toughness tests at lower levels of side grooving have been included, for comparison to those presented in chapter 6 for reference.

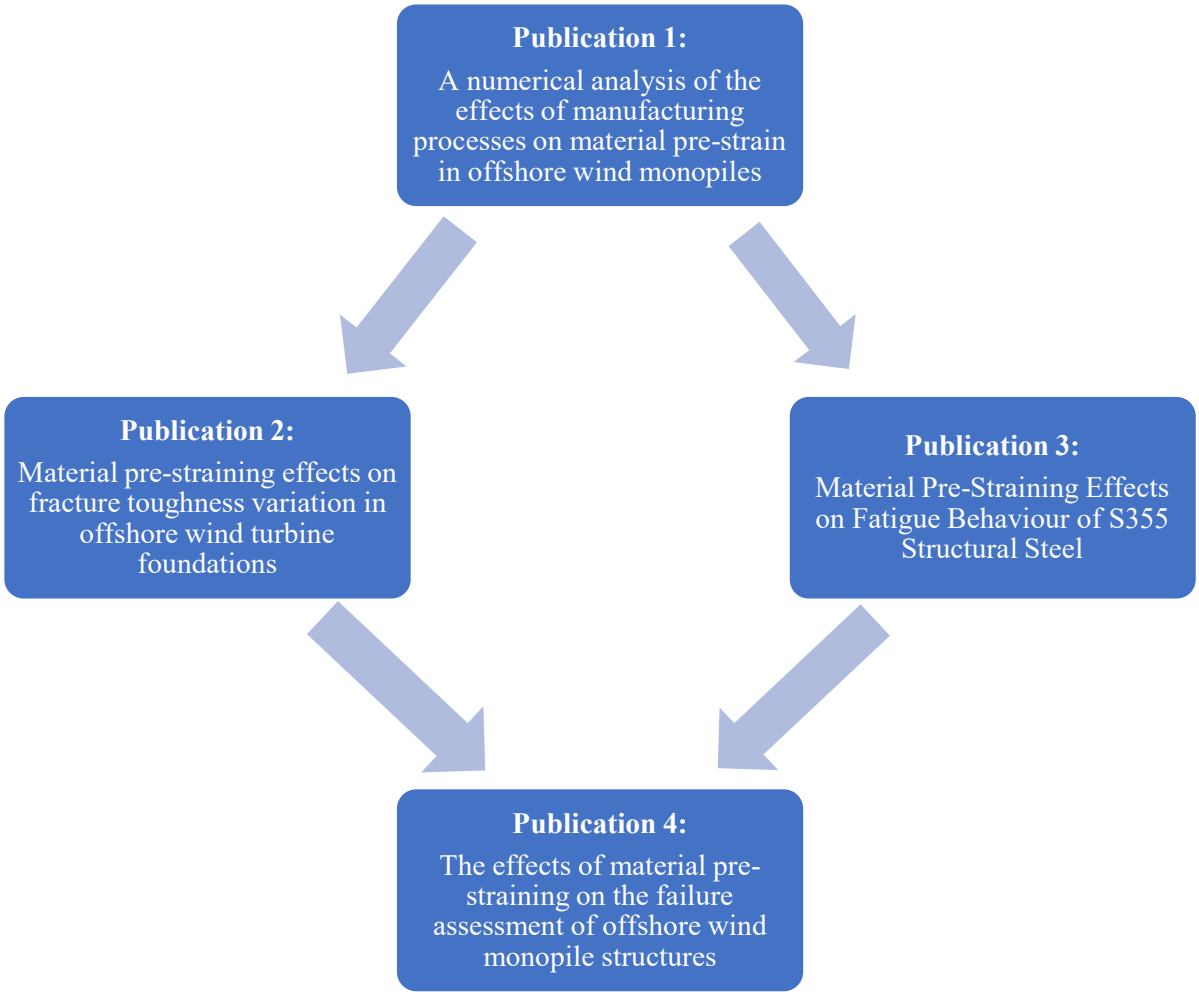

Figure 2 - Interconnection of Publications

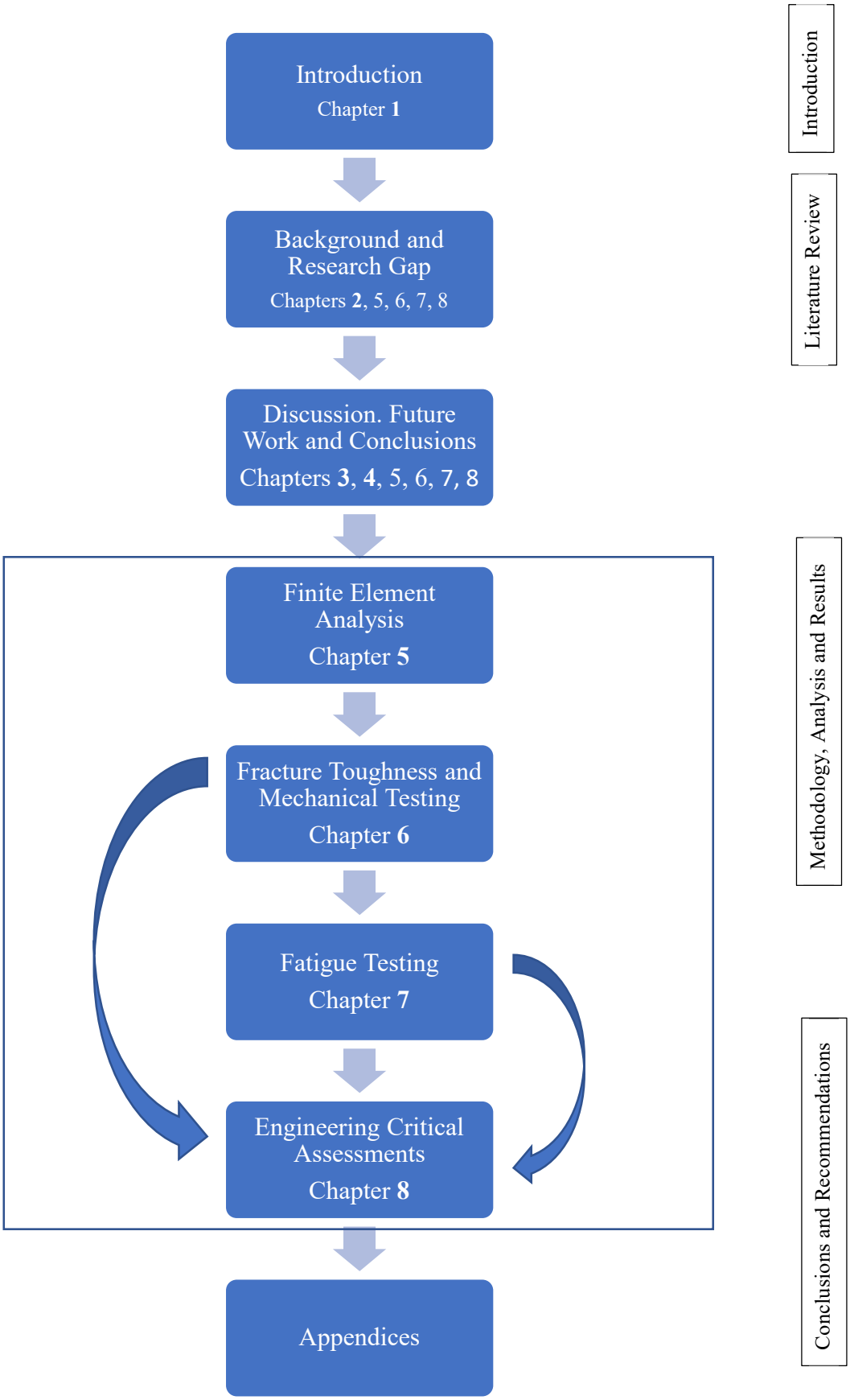

Figure 3 - Structure of Thesis (main relevant chapters highlighted in bold)

References

1. Soares-Ramos EPP, de Oliveira-Assis L, Sarrias-Mena R, Fernández-Ram\'\irez LM. Current status and future trends of offshore wind power in Europe. Energy [Internet]. 2020 Jul;202:117787. Available from: https://doi.org/10.1016%2Fj.energy.2020.117787

2. Spring MJJ. Global Expansion of Offshore Wind Power Depends on Overcoming Significant Challenges Facing Floating Wind Turbines. In: Offshore Technology Conference [Internet]. Offshore Technology Conference; 2020. Available from: https://doi.org/10.4043%2F30524-ms

3. Darwish AS. Wind Energy in the {UK}: Progress and Future Expectations. In: The Age of Wind Energy [Internet]. Springer International Publishing; 2019. p. 193–204. Available from: https://doi.org/10.1007%2F978-3-030-26446-8_11

4. Henderson AR, Morgan C, Smith B. Offshore Wind Energy in Europe. Wind Energy. 2001;(October):1–6.

5. Office PM. New plans to make UK world leader in green energy. Press Release. 2020.

6. UK Government. Wind powered electricity in the UK. 2019;(March 2015):59–66.

7. Agency A. Global Offshore Wind Capacity to Grow 37% in 2021 [Internet]. 2021. Available from: https://www.iene.eu/global-offshore-wind-capacity-to-grow-37-in-2021-p6127.html

8. Deloitte. 2021 renewable energy industry outlook Accelerating energy industry convergence. 2021;

9. Velarde J, Kramhøft C, Sørensen JD, Zorzi G. Fatigue reliability of large monopiles for offshore wind turbines. International Journal of Fatigue [Internet]. 2020 May;134:105487. Available from: https://doi.org/10.1016%2Fj.ijfatigue.2020.105487

10. Nordenham S. Beyond XXL - Slim Monopiles for Deep-Water Wind Farms [Internet]. 2020. Available from: https://www.offshorewind.biz/2020/05/11/beyond-xxl-slim-monopiles-for-deep-water-wind-farms/

11. Trojnar K. Simplified design of new hybrid monopile foundations for offshore wind turbines. Ocean Engineering [Internet]. 2020;219(July 2020):108046. Available from: https://doi.org/10.1016/j.oceaneng.2020.108046

12. Snieckus D. Monopiles' steel cost could be slashed "by 30%" after design debunk [Internet]. 2020. Available from: https://www.rechargenews.com/wind/monopiles-steel-cost-could-be-slashed-by-30-after-design-debunk/2-1-760798

13. Oh KY, Kim JY, Lee JS. Preliminary evaluation of monopile foundation dimensions for an offshore wind turbine by analyzing hydrodynamic load in the frequency domain. Renewable Energy [Internet]. 2013;54:211–8. Available from: http://dx.doi.org/10.1016/j.renene.2012.08.007

14. Broadbent I, Strachan P. UK government puts offshore wind at risk. Energy Post [Internet]. 2015;(January). Available from: http://www.energypost.eu/sea-uk-government-putting-future-offshore-wind-risk/%5Cnpapers3://publication/uuid/BF07BB82-E4DE-44F7-9069-3A86CBED6D17

15. Oh KY, Nam W, Ryu MS, Kim JY, Epureanu BI. A review of foundations of offshore wind energy convertors: Current status and future perspectives. Renewable and Sustainable Energy Reviews. 2018;88(April 2016):16–36.

16. Luengo MM, Kolios A. Failure mode identification and end of life scenarios of offshore wind turbines: A review. Energies. 2015;8(8):8339–54.

17. Márquez-Domínguez S, Sørensen JD. Fatigue reliability and calibration of fatigue design factors for offshore wind turbines. Energies. 2012;5(6):1816–34.

2. Literature Review

2.1 Mechanical Properties of Materials

Metals can be characterised easily by undertaking a simple tension test to generate a tensile stress-strain curve. A stress-strain curve can indicate important material parameters such as the Young's Modulus, yield strength, ultimate tensile strength, and engineering strain at failure. Figure 4 illustrates a typical stress strain curve for metals. The linear portion of the curve may be referred to as the elastic region; the region in which any deformation is reversible (known as elasticity). The point at which this region ends is referred to as the yield point, or yield stress. Stresses beyond the yield stress may enter the plastic region; and in this region any deformation or damage is irreversible (known as plasticity). The highest value of stress on the curve is commonly known as the ultimate tensile strength, beyond which necking of the material and eventual failure will occur. Between the regions of yield strength and ultimate tensile strength, a visible increase in strength can be observed. This is known as hardening behaviour, which is due to the dislocation generation and movement resulting in an increase in strength.

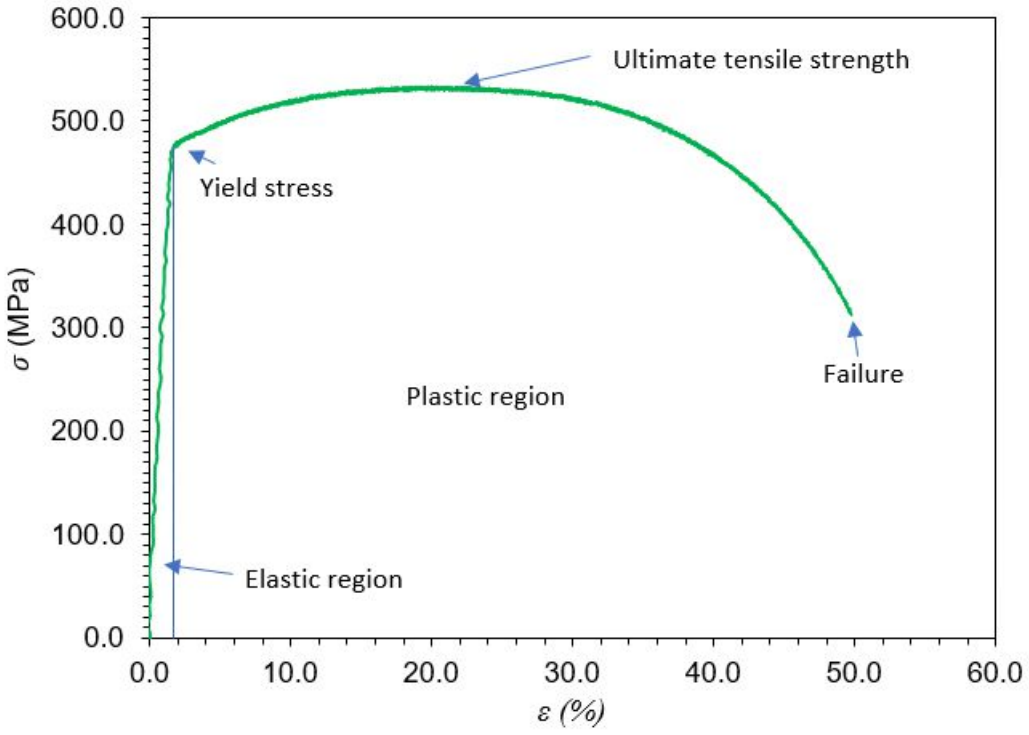

Figure 4 – Typical stress-strain curve for metals

The concept of pre-strain arises from the aforementioned idea of plasticity. Beyond this elastic region, the level of plastic strain present in a material may be referred to as inelastic damage, or pre-straining. This can be expressed as a percentage of plastic strain or dimensionless, which can be calculated by:

$$\varepsilon_{plastic} = \varepsilon_{total} - \varepsilon_{elastic}$$ Equation 1 – Calculation of plastic strain

Where $\varepsilon_{plastic}$ is the plastic strain, ε_{total} is the total strain, and $\varepsilon_{elastic}$ is the elastic strain.

In some cases, it may be more meaningful to present the instantaneous stress-strain behaviour, known as true stress and true strain. These can be related by (1):

$$\sigma_{true} = \sigma(1 + \varepsilon)$$ Equation 2 – Calculation of True stress

$$\varepsilon_{true} = \ln(1 + \varepsilon)$$ Equation 3 – Calculation of True Strain

Where σ is the engineering stress, and ε is the engineering strain.

In cases such as in applications in finite element analysis, it is necessary to define plasticity in terms of true stress and true plastic strain. True plastic strain can be defined as:

$$\varepsilon_{pl,true} = \varepsilon_{true} - \frac{\sigma_{true}}{E}$$ Equation 4 – Calculation of true plastic strain

2.2 Fracture Mechanics Fundamentals

2.2.1 Modes of Cracking

A structure or body containing a crack can be loaded in one of three displacement modes, or a combination of two modes. These are known as mode 1 (opening mode), mode II (sliding mode), and mode III (tearing mode) (see Figure 5). In mode 1 fracture, the crack faces move apart, as a result of tensile stresses normal to the crack plane. Mode II involves the crack faces sliding away from each other, with mode III involving sliding in the direction parallel to the leading edge. Both of these latter modes are due to shear loading in different directions. Of these loading modes, mode I is the most commonly used for the determination of fracture toughness during fracture toughness testing.

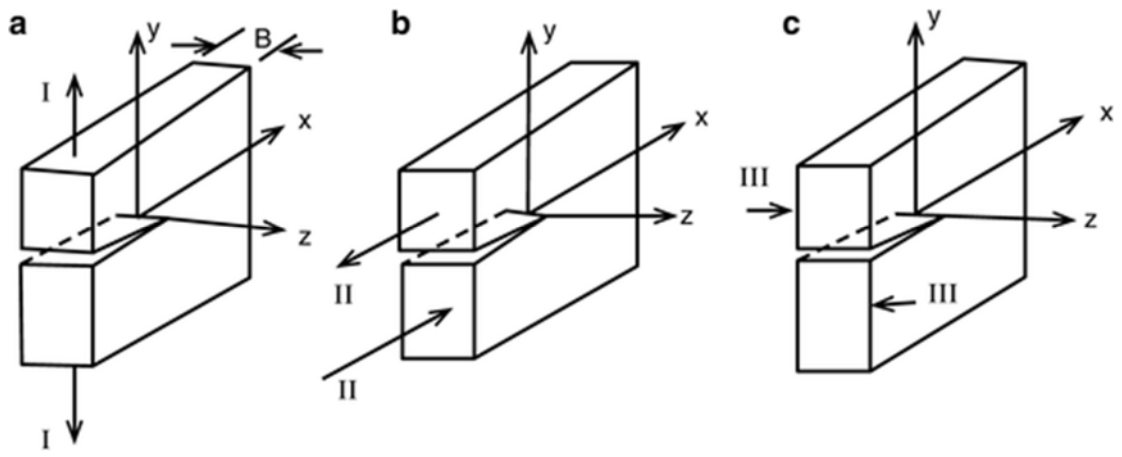

Figure 5 - Displacement modes for cracks in a solid body (3)

2.2.2 Linear Elastic Fracture Mechanics

Linear elastic fracture mechanics is the study of cracks when stresses are within the elastic region, thus any deformation is not permanent. Small scale yielding can occur; however, these amounts of yielding are considered negligible. A.A. Griffith was considered the leader of this area of study in the 1920s, where early tests were performed on glass (4). As previously mentioned in 2.2.1, fracture mechanics tests commonly take place under mode I fracture, where stresses are normal to the crack plane. The stress intensity factor, K, is a commonly used fracture mechanics parameter which defines the magnitude of stresses in front of a sharp crack tip. As the crack tip is dependent on factors such as geometry and loading, etc, the stress intensity factor is therefore a function of these conditions. In infinitely large plates, a through thickness Griffith's crack of length $2a$ subjected to a nominal stress under mode 1 loading can be defined as:

$$K = \sigma\sqrt{\pi a}$$ Equation 5 – Calculation of stress intensity factor

Where σ is the nominal stress, and a is the half crack length

However, as test specimens and structures are of finite sizes, and cracks may not necessarily be through thickness (such as the case of surface cracking), the K solutions may differ for various configurations and loading conditions. Therefore, the aforementioned expression in equation 5 may be rewritten as:

$$K = Y\left(\frac{a}{W}\right)\sigma\sqrt{\pi a}$$

Equation 6 – Rewritten stress intensity factor equation

where Y is a dimensionless shape correction factor, and W is the width of the test specimen. Solutions for $Y(a/W)$ for standard geometries such as compact tension (C(T) specimens (a standard notched specimen geometry recommended for fracture toughness testing in ASTM and ISO standards), and flat plates can be found in literature and relevant codes and standards.

Griffith's derived the energy release rate, G, defined as the energy for an increment of crack extension, and is based on strain energy. G (J/m^2) can be simplified as:

$$G = \frac{\pi\sigma^2 a}{E}$$

Equation 7 – Griffith's energy release rate calculation

Combining the equation for K, the relationship between G and K can be written as (5):

$$G = \frac{K^2}{E'}$$

Equation 8 – Relationship between G and K

where E' is E in plane stress conditions, or $E' = E(1-\nu^2)$ in plane strain conditions.

2.2.3 Non-Linear Fracture Mechanics

The Griffith's criterion and stress intensity factor are not as relevant for materials exhibiting plastic behaviour, as the plastic zone size ahead of the crack tip becomes too large for small scale yielding to be considered negligible. Therefore, the stress intensity factor cannot be used to define the amplitude of stresses at the crack tip. In non-linear fracture mechanics, the J integral is used to describe the behaviour at the crack front. This integral was developed by James Rice in 1968 (6), by defining a path independent strain energy release rate of a crack to characterise the stress-strain fields around a crack tip. Thus, this parameter both defines energy and stress intensity, and can both be used for linear and non-linear elastic materials and is defined as (7,8):

$$J = \int_r \left(W dy - T_i \frac{\partial u_i}{\partial x} ds\right)$$

Equation 9 – Calculation of J integral

Where W is the strain energy density, u is the displacement vector, T is the traction vector bounder by I', s is the arc length, and I' is the anticlockwise contour around the crack tip.

J can be split into elastic $J_{elastic}$ and plastic $J_{plastic}$ and expressed as:

$$J_{total} = J_{elastic} + J_{plastic}$$ Equation 10 – Equation for J total

where the $J_{elastic}$ is defined simply as:

$$J_{elastic} = \frac{K^2}{E'}$$ Equation 11 – Definition of J elastic

For ductile materials, ESIS P2-92 (a common fracture toughness testing standard) states that R curves are created by calculating the fracture resistance J, and plotting it against the Δa (crack length) (9)

$$J_{plastic} = \frac{U}{B_n(W - a_0)}\eta$$ Equation 12 – Calculation of J plastic

Where $\eta = 2+0.522\ (1-a_0/W)$

W is the specimen width, a_0 is the initial crack length, B_n is the net thickness between side grooves on the C(T) specimen (to ensure equal crack propagation along the crack front), and U is the area under the P vs LLD (load vs load line displacement) plot. Section 6.4.1 gives further explanation on fracture toughness testing and the generation of *P vs LLD* plots. Δa can be calculated by the unloading compliance technique; a technique which involves calculating the inverse of the slope of the elastic unloading part of the P vs LLD to determine the crack size. The crack length corresponding to a specimen compliance C determined from the load line displacement is given by:

$$\frac{a}{W} = 1.000196 - 4.06319\mu + 11.242\mu^2 - 106.043\mu^3 + 464.335\mu^4 - 650.677\mu^5$$ Equation 13 – Calculation of a via unloading compliance

Where

$$\mu = \frac{1}{[B_{eff}E_M C]^{1/2} + 1}$$

Equation 14 – Calculation of μ

$$B_{eff} = B - (B - B_n)^2/B$$

Equation 15 – Calculation of B_{eff}

And E_M, the effective Young's Modulus, is determined from:

$$E_M = \frac{1}{C_0 B_{eff}}\left(\frac{W + a_0}{W - a_0}\right)^2 [2.163 + 12.219 + \left(\frac{a_0}{W}\right) - 20.065\left(\frac{a_0}{W}\right)^2 - 0.9925\left(\frac{a_0}{W}\right)^3 + 20.609\left(\frac{a_0}{W}\right)^4 - 9.9314\left(\frac{a_0}{W}\right)^5$$

Equation 16 – Calculation of Effective Young's Modulus

C_0 is the average compliance determined from the unloadings performed in the elastic regime.

2.3 Introduction to Fatigue

Structures are subjected to repeated stress cycles and can induce materials to fail by introducing damage into materials. S-N curves are plotted as a function of the stress range against a corresponding number of cycles. This phenomenon has been researched for over 150 years, with some of the earliest fatigue tests conducted by Wöhler in 1870, where it was concluded that stress range was the critical factor in determining the failure of a material. The higher the stress range, the lower the number of cycles to failure. This conclusion is still valid in the present era, and still plays a key role in design codes for the design of steel structures.

2.3.1 SN Fatigue

Testing to determine the slope of the number of cycles to failure vs the stress range can be conducted to plot a stress-life curve, also commonly known as the S-N curve. S-N fatigue testing can involve cycles of stress being applied between a minimum and maximum value, also known as the stress range:

$$\Delta\sigma = \sigma_{max} - \sigma_{min}$$ Equation 17 – Calculation of stress range

The mean stress can be calculated as:

$$\sigma_{mean} = \frac{\sigma_{min} + \sigma_{min}}{2}$$ Equation 18 – Mean stress calculation

The stress amplitude can be calculated by:

$$\sigma_{amplitude} = \frac{\Delta\sigma}{2} = \frac{\sigma_{max} - \sigma_{min}}{2}$$ Equation 19 – Stress amplitude calculation

The *R* ratio is another important component in the fatigue testing of metals. *R* is known as the stress ratio, and is calculated by:

$$R = \frac{\sigma_{min}}{\sigma_{max}}$$ Equation 20 – Calculation of R ratio

Since the stress life can change with stress level over several orders of magnitude, S-N curves are usually plotted on log-log axes. The resulting S-N curve can then be fitted to the following linear mathematical expression:

$$Log_{10}N = A - Blog_{10}\Delta\sigma$$ Equation 21 – Linear expression for S-N curve

It can also be fitted with the Wohler relationship, a power law equation:

$$N = A(\Delta\sigma)^{B}$$ Equation 22 – Wohler's equation

It is common for many steels to reach a fatigue limit – a stress range below which fatigue failure is never expected to occur. The number of cycles required to determine a stress range as a fatigue limit can differ, in most cases this is assumed to be around 10^7.

However, studies by Wang suggest that this limit may not come into play until 10^9 cycles (10).

The Palmgren-Miner law linear damage rule is used to predict the fatigue life in the case of variable loading (11):

$$D_f = \sum \frac{N_i}{N_{fi}}$$

Equation 23 – Palmgren-Miner rule for damage

Where N_i is the number of cycles at a given stress range, N_{fi} is the number of cycles to failure at this stress range, and D is the damage variable. Using this rule, the damage caused by a certain number of stress cycles can be calculated. Failure is expected to occur when $D = 1$.

2.3.2 Fatigue Crack Growth

Fatigue crack growth behaviour can be described by the Paris equation – an equation correlating the cyclic crack growth rate da/dN with the stress intensity range ΔK. The constants C and m can be identified by plotting test data on a log-log axis and by using a power law data fit the constants can be established. The Paris relationship is described as (12):

$$\frac{da}{dN} = C(\Delta K)^m$$

Equation 24 – Paris equation

Where m is the gradient of the line, and C is a constant.

This equation can be integrated to calculate the number of cycles required to propagate a crack. Integrating the Paris equation gives:

$$\frac{da}{dN} = C\Delta K^m = C\left(Y\Delta\sigma\sqrt{\pi a}\right)^m$$

$$\int_0^{N_f} dN = \int_{a_i}^{a_f} \frac{da}{CY^m\Delta\sigma^m(\pi a)^{\frac{m}{2}}}$$

Equation 25 – Integration of Paris law

$$N_f = \frac{1}{CY^m \Delta\sigma^m \pi^{\frac{m}{2}}} \int_{a_i}^{a_f} \left[\frac{a^{-\frac{m}{2}+1}}{-\frac{m}{2}+1} \right]$$

$$= \frac{1}{CY^m \Delta\sigma^m \pi^{\frac{m}{2}}} \left[\frac{a_f^{1-\frac{m}{2}} - a_i^{1-\frac{m}{2}}}{1-\frac{m}{2}} \right]$$

Where a_f is the final crack length, a_f is the initial crack length, and Y is a dimensionless shape factor.

2.4 The Effects of Size on Material Properties

Size effects can influence the behavioural properties of high strength steels. Ultrasonic gigacycle fatigue tests at a frequency of 20kHz were conducted on high strength steels. The round bars used in the testing were of varying diameters, ranging from 3mm to 14mm. From the experimental results, it was observed that the fatigue strength of the material decreased with respect to an increase in diameter. This was believed to be due to an increase in inclusion size as the specimen sizes increased, resulting in a reduction in fatigue strength (46). Table 1 outlines the mechanical properties of S355 for the design of structures. From the table it can be observed that as the thickness increases, the yield stress decreases, in addition to a reduction in ultimate tensile strength (25). Such reduction in material properties would thus have an effect on the failure assessment of monopiles using failure assessment diagrams, as this can affect the L_r value that is calculated. Thickness effects have been believed to have an effect on the fracture toughness of metals. A study conducted on steel alloy GOST 08Ch22N6T showed that R curves for thinner specimens had a steeper R curve than those of thicker specimens. This could be due to lower degrees of stress triaxiality at the crack tip of thinner specimens (47).

2.5 Material Pre-Straining Effects on Metals

During fabrication processes, material pre-straining can be introduced into materials via plastic deformation. The effects of this pre-conditioning have been observed in many materials such as 316H, 4350 and 7050-T7451. 316H is widely used in advanced gas cooled reactors in the power industry, and a test programme of tensile, fracture toughness and fatigue crack growth testing on pre-compressed 316H samples were conducted by

Mehmanparast et al (13). Samples of 316H were pre-compressed to 0%, 4%, 8% and 12% plastic strain prior to testing. From the tensile test results, it was observed that the mechanical properties of the material exhibited significant changes as the pre-straining increased. It could be seen that the tensile curve of 12% pre-compression material compared to as received, had a yield strength of almost double that of the base metal, with a significant reduction in strain at failure, but there was no significant change in the ultimate tensile strength (14). Experimental test results on fatigue crack growth behaviour showed that material pre-straining had no significant effect on the Paris law constants derived from the test results (13).

From fracture toughness testing of 316H, a reduction in J_{IC} was noticed with increasing pre-straining, and this behaviour has been observed in other studies on the same material (15). In a study by Liaw and Landes, experiments to capture the fracture toughness and mechanical properties of 4340 and 316 steels were conducted, comparing base metal to 2% and 5% pre-strained material. Results showed that the yield and ultimate tensile strength increased with pre-tension for 316 steel, with a decrease in elongation percentage. It was also noted that fracture toughness properties of 316 and 4340 decreased with increasing pre-straining percentage (16). In low alloy steels, it has been observed that the fracture toughness properties of a low alloy steel similar to AISI 4340 pre-tensioned from 0% to 15% exhibited a reduction in fracture toughness (17).

Pre-straining effects on the fatigue behaviour of 7050-T7451 aluminium alloy, commonly used in the aviation industry, have previously been studied. From the test programme, S-N curves of unnotched 7050-T7451 pre-tensioned to 1%, 3%, 5% and 7% were studied and compared to that of base metal, with results showing a decrease in fatigue life with increasing pre-straining level (18). Similar trends have been observed in the case of line pipe steels such as HSLA-80 and HSLA-100, where fracture toughness was seen to deteriorate at pre-straining levels above 2% (19).

X65 line pipe steels were pre-strained up to 10% (0%, 1.5%, 5%, 10% pre-tension conditions). From tensile testing, monotonic stress-strain curves were obtained, and it was observed that an increase in pre-straining resulted in a higher yield strength, increases in ultimate tensile strength and a reduction in engineering strain at failure. CTOD (crack tip opening displacement) tests showed that up to 5% pre-straining had an insignificant effect

on CTOD values, but pre-straining above 5% had a detrimental effect on fracture toughness (48).

2.6 S355 Structural Steel

European Standard EN10025 steel is widely used in the offshore wind industry, where its main challenges are fatigue and corrosion damage, which pose great difficulties in the life cycle estimation of monopile structures (20) (21). At room temperature it has an elastic modulus of 190 to 210 GPa, minimum yield strength of 355 MPa, and ultimate strength of between 470 and 630 MPa (22–24). The material properties can vary slightly with thickness, and recommended values from DNV for design have been outlined in Table 1 (25). Literature has shown that its material properties change with temperature, such as ultimate tensile strength, uniform strain, fracture strength and fracture strain, effective yield strength and reduction of area. Up to temperatures of 400-500°C the material increases strength, however, once it reaches temperatures of 90°C the strength will decrease. This phenomenon is a common occurrence in carbon steels, also known as blue brittleness. Blue brittleness occurs due to dislocation motion and dependence on interstitial atoms. At around 550°C, an increase in strength is seen as well as reduction in total elongation (26). Tensile tests were conducted on S355 specimens at temperatures corresponding to the ductile to brittle transition temperatures of SENB specimens, at a range of -120 to 20°C. Results showed that as the temperature increased, there was a visible reduction in yield strength, ultimate tensile strength, and an increase in engineering strain at failure (49) This illustrates that temperature does have a significant effect on the mechanical properties of S355. In the context of offshore wind monopiles, this may be worth noting as various environmental climates (such as colder regions) may impact the mechanical behaviour of offshore wind monopile structures.

Table 1 – Recommended mechanical properties of S355 for design of structures

Thickness (mm)	**$t \leq 16$**	**$16 \leq t \leq 40$**	**$40 \leq t \leq 63$**
E (MPa)	210000		
σ_{yield}	355	345	335
σ_{UTS}	470	470	450
ε_{p_yield}	0.004		
ε_{p_UTS}	0.15		

Comparisons of tensile data of S355 and S690 have previously been made in literature, to allow comparison of the yield regions and initial strain hardening behaviour. S355 has been known to achieve a yield plateau, after which, significant strain hardening can be observed. This is known as discontinuous yielding, and for this study the yield stress has been determined as the maximum stress within the yield plateau (27). S355 has been seen to keep its strain capacity with increasing strain rate, however, at high strain rates displays instability (such as lower and upper yield strengths). This is due to the dependence on dislocation density, velocity, and loading rate.

Testing on samples of S355 were conducted in a study by Pawliczek and Prazmowski, to determine changes in material structure and strengthening behaviour after being subjected to a set number of cycles. In this study, this number of cycles was set at 15,000. Bending fatigue testing was conducted under a block load with varying mean load values, which was then followed by tensile and metallographic tests. Each block was split into three parts – each 5000 cycles long. Each third was cycled at a load level of 200, 300 or 400 MPa. A set of tests were run increasing the load incrementally from 200 to 400Mpa, and vice versa for the next set. These stress values allowed for plastic deformation to occur during testing, while ensuring the specimen was not fully damaged. It was observed that higher values of mean loading at the beginning of the block load resulted in hardening behaviour, and thus it was noted that pre-strain can induce hardening in the material. The samples subjected to the cyclic loading showed an increase in material resistance. From tensile tests, the maximum tensile force showed a 16% increase when the average value of block sequences was reduced, and so material strengthening could be observed. However, microstructural analysis showed no difference in microstructure before and after testing (28).

Low cycle fatigue testing has previously been conducted on S355 in controlled strain conditions. Hysteresis loops for 0.3% and 1.2% strain were presented, with maximum and minimum stress levels decreasing with the number of loading cycles at 0.3%. The opposite trend was observed in tests conducted at 1.2% strain. From the results of the study, it was concluded that S355 undergoes three stages of change during strain-controlled fatigue testing. During stage one, the material is seen to get weaker, and the length of this stage is strain level dependent. Stage two is also strain level dependent – with lower strain levels showing further material weakening, and higher strain levels

exhibiting material strengthening behaviour. At stage three, the strain level is no longer a factor, and the material gets weaker regardless and fatigue cracking will initiate (29).

High cycle S-N curves in literature for base metal S355 have been sourced and are presented in Figure 6, with specimens taken at 2 different orientations from a rolled block of S355, tested at an R ratio of -1 (30,31). Design curves for steel structures recommended by DNV, Eurocode, NORSOK, BS 7608 and IIW have also been plotted for comparison purposes (32). From the comparison it would appear that the design codes predict a lower number of cycles to failure compared to the actual literature results for S355.

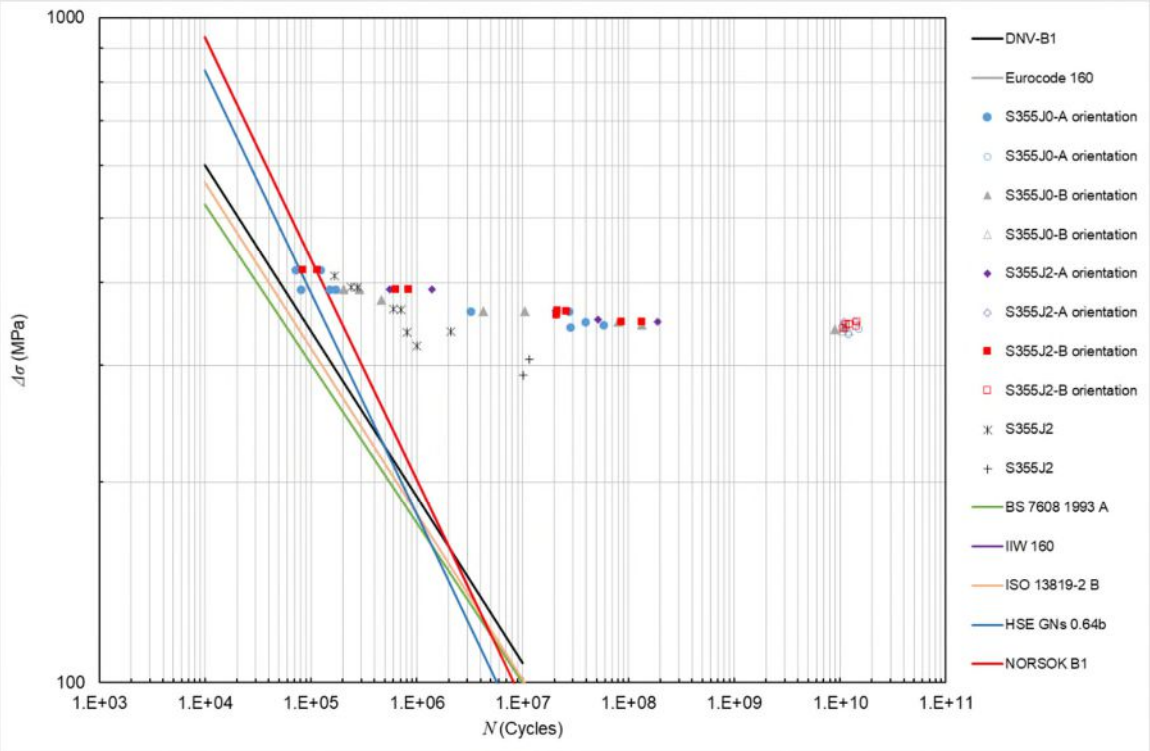

Figure 6 - Comparisons of S355 data in literature to design standards

An interlaboratory testing programme involving characterisation of the mechanical, fatigue crack growth and fracture properties of S355 was conducted as part of the SLIC project. The results of this project showed that the yield stress of S355 increased from base metal, to heat affected zone, to weld metal (33). These results could suggest that pre-straining of the material can happen via processes such as bending, forging, and welding during the fabrication process (51). Fatigue crack growth tests were conducted in air and seawater with S355 base metal and heat affected zone C(T) specimens, and from the results it was observed that the *da/dN* for seawater condition was twice that of air

conditions, for both base metal and heat affected zone material. This was seen to be less than the crack acceleration factor that is recommended by BS7910. However, it was seen that BS7910 2 stage Paris law based trends gave an acceptable estimate for fatigue crack growth behaviour of base metal in both environmental conditions (34).

Although fatigue testing on S355 has been conducted, there is very little data on the effects of material pre-straining on the fatigue behaviour of S355. In addition, no damage level has been calculated to correlate the results with regard to fatigue damage. Fatigue crack growth and fracture data for base metal is available for S355, however the impact of material pre-straining on these results is currently unknown and will be investigated in this study.

2.7 Three Roll Bending Manufacturing Process

Roll bending, also known as three-roll forming (called the pyramid type) or plate bending, is the process of giving a curvature to a sheet/bar/shaped section by bending it between two or three adjustable cylindrical rolls. Common applications of this procedure are in making cylinders for pressure tanks, monopile cans, boilers, corrugate pipe, cones for hoppers, structural sections for submarines, aircraft, and nuclear reactors (35).

This process is known as a continuous manufacturing process, meaning that local deformation is moving over the entire plate, and at any instant only a small region is being formed. It is suitable for small batch or single products due to its low set-up cost. However, it is time consuming. To overcome this, three rollers were introduced into the process to manufacture a doubly curved sheet. This ensures that the deformation is within a local contact region below the centre roll, and the plate is rolled within one pass (36).

The rollers used for this process are of the same diameter. Two of the rollers are held in a fixed position while the other is adjustable. The metal plate passes through the rolls, and its final diameter is dictated by the position of the adjustable roller. The closer the roller is moved to the other rolls, the smaller the diameter. Such machines are made in capacities ranging from small gauge thicknesses to others which can form heavy plates up to 30mm in thickness (37).

The roll bending process is divided into three steps:

1. Positioning the blank plate

2. Lowering the centre roller
3. Feeding in the plate

In step one, the blank plate is fed into the machine via two side rollers until the plate is positioned properly. In step two, the centre roller is lowered onto the plate, thus bending it. The third step involves the two side rollers rotating so that the plate is being bent continuously. During this step, it is ensured the whole plate is bent equally through the rollers to ensure all points undergo the same stress and strain history (38)(50).

The rolls are employed as a forming tool to generate curvature in the longitudinal and transverse directions simultaneously. The metal sheet is bent by the configuration of the rollers. In the longitudinal direction, the upper and lower rollers bend the sheet downwards (36).

The longitudinal deformation is dependent upon the vertical positioning of the upper roller in relation to the lower rollers and thus the basic forming principle is the three-point bending of a plate. As the plate moves from right to left, it forms contact points with the three rollers. Thus, the plate can be split into three regions by their contact points: the formed region, the deformation region, and undeformed region. In Figure 7 the deformation region AC is a sheet metal and includes a loading region AB and unloading section BC. In the loading area, the bending moment increases from zero (at point A) to its maximum M_{max} at point B. During this, the longitudinal curvature of the plate increases from zero to its maximum K_{Lmax}. In the unloading area, the curvature is decreased from point B to point C, and the bending moment decreases. At point C, the external loading has been completely removed and remaining plastic deformation can be expressed by residual curvature K^*_L (36)(39).

$$K_L^* = K_{Lmax} - \frac{M_{max}}{E'I}$$

Equation 26 – Calculation of residual curvature

Where M_{max} is the bending moment per unit width of sheet metal at the point B, K_{Lmax} is the curvature of deformed sheet metal at point B, I is the second moment of area of sheet metal per unit width, $E' = E/1\text{-}\mu^2$ and E is the Young's modulus and μ is the Poisson's ratio of the material.

M_{max} is the bending moment per unit width of sheet metal at the point B:

$$M_{max} = F * d$$

Equation 27 – Calculation of bending moment per unit width

Where *F* is the force, and *d* is the distance/length.

I is the second moment of area of sheet metal per unit width:

$$I = \frac{bh^3}{12}$$

Equation 28 – Second moment of area

E' is:

$$E' = \frac{E}{1 - \mu^2}$$

E is the Young's modulus and

μ is the Poisson's ratio of the material.

The final curvature of the elastic perfectly plastic sheet in the longitudinal direction is given by:

$$K_L^* = \frac{2\sigma_s'}{E'h}\left(\frac{1}{\sqrt{3 - 2\xi}} - \xi\right)$$

Equation 29 – Final curvature equation

Where:

$$\sigma_s' = \frac{\sigma_s}{\sqrt{1 - \mu + \mu^2}}$$

And:

$$\xi = \frac{M_{max}}{M_e}$$

Where M_e is the maximum elastic moment per unit width of sheet metal

2.8 Fitness for Service

During the life cycle of a component or structure, it is inevitable that defects may appear during the duration of its operation (40). By inspection and maintenance, the risk of catastrophic failure can be mitigated, and thus repairing or replacing parts at the correct

time can save overall operation and management costs. The assessment of defects can be known as engineering critical assessments, or fitness for service assessments, which provide standardised routes of assessment (41). Such assessments are usually carried out via the failure assessment diagram technique, which correlates various factors such as fracture toughness and defect size to determine whether a structure or component may be deemed “safe”.

The concept of the Failure Assessment Diagram (FAD) is a common method of determining the stability of a material in the presence of a flaw. Static failure of offshore structures containing a defect can occur either by fracture or plastic collapse. The benefit of this methodology is that it allows engineers to apply linear elastic fracture mechanics (LEFM) concepts to the failure assessment of a structure, as failure will occur when the stress intensity, K_I, reaches a critical value (K_{mat}). The FAD approach was originally derived from a two-criterion approach, which states that structures or components can fail by either plastic collapse or brittle fracture. If the service assessment point falls within the boundaries given by the failure assessment line, the structure is considered safe. There are currently three options of failure assessment diagram available, which are selected based on their complexity and the range of data available.

By rearranging the Paris equation, the remaining useful life in which the component/structure may be deemed “safe” can be calculated. There are many codes and standards which outline the best practice for fitness for service assessment; three of which are most common are R6, BS7910 and API 579 (42) (43) (44). All standards pose their individual merits, with a degree of interchangeability between them depending on company policies and attitudes (45). It is therefore of utmost importance to have accurate fracture and fatigue crack growth data to hand in order to ensure correct fitness for service assessment of structures. Since material pre-straining has been shown to affect the properties of a material, it is therefore of prime importance to ensure that the data being used to carry out fitness for service assessments will reflect the behaviour due to pre-straining accurately.

2.9 References

1. Callister WD. Materials Science and Engineering: An Introduction. Seventh. New York, NY: John Wiley & Sons; 2007.

2. Systems D. Defining plasticity in Abaqus [Internet]. [cited 2021 Mar 1]. Available from: https://abaqus-docs.mit.edu/2017/English/SIMACAEGSARefMap/simagsa-c-matdefining.htm

3. Perez N. Fracture Mechanics: Second edition. Fracture Mechanics: Second Edition. 2017. 1–418.

4. Griffith AA. The Phenomena of Rupture and Flow in Solids. Philosophical Transactions. 1920;221(Series A):163–98.

5. Alfred Wöhler. Über die Festigkeits-Versuche mit Eisen und Stahl. Berlin: Ernst und Korn; 1870.

6. Dowling NE. Mechanical Behaviour of Materials - Engineering Methods for Deformation, Fracture and Fatigue. Fourth Edi. Pearson Education; 2012.

7. Dharan CKH, Kang BS, Finnie I. The Nature of Fracture. In: Finnie's Notes on Fracture Mechanics: Fundamental and Practical Lessons [Internet]. New York, NY: Springer New York; 2016. p. 1–19. Available from: https://doi.org/10.1007/978-1-4939-2477-6_1

8. Rice JR. A path independent integral and the approximate analysis of strain concentration by notches and cracks. Journal of Applied Mechanics, Transactions ASME. 1964;35(2):379–88.

9. ESIS. ESIS P2-92: Procedure for Determining the Fracture Behaviour of Materials. European Structural Integrity Society. 1992. p. 1–92.

10. Wang QY. Fatigue crack initiation and growth behavior of a thin steel sheet at ultrasonic frequency Title. In: Proceedings of the 7th International Fatigue Congress (Fatigue'99). 1999.

11. Stephens RI, Fatemi A, Stephens RR, Fuchs HO. Metal fatigue in Engineering. John Wiley & Sons; 2000.

12. Paris P, Erdogan F. A critical analysis of crack propagation laws. Journal of Fluids Engineering, Transactions of the ASME. 1963;85(4):528–33.

13. Mehmanparast A. The Influence of Inelastic Damage on Creep, Fatigue and Fracture Toughness. Department of Mechanical Engineering. 2012; PhD (September).

14. Mehmanparast A, Davies CM, Dean DW, Nikbin K. Effects of plastic pre-straining level on the creep deformation, crack initiation and growth behaviour of 316H stainless steel. International Journal of Pressure Vessels and Piping [Internet]. 2016 May;141:1–10. Available from: https://doi.org/10.1016%2Fj.ijpvp.2016.03.013

15. Mehmanparast A, Davies CM. The influence of inelastic pre-straining on fracture toughness behaviour of Type 316H stainless steel. Engineering Fracture

Mechanics [Internet]. 2018 Feb;188:112–25. Available from: https://doi.org/10.1016%2Fj.engfracmech.2017.08.001

16. Liaw PK, Landes JD. Influence of prestrain history on fracture toughness properties of steels. Metallurgical Transactions A [Internet]. 1986 Mar;17(3):473–89. Available from: https://doi.org/10.1007%2Fbf02643954

17. Amouzouvi KF, Bassim MN. Effect of the type of prior straining on the fracture toughness of AISI 4340 steel. Materials Science and Engineering. 1983;60(1):1–5.

18. Al-Rubaie KS, del Grande MA, Travessa DN, Cardoso KR. Effect of pre-strain on the fatigue life of 7050-T7451 aluminium alloy. Materials Science and Engineering A. 2007;464(1–2):141–50.

19. Sivaprasad S, Tarafder S, Ranganath VR, Ray KK. Effect of prestrain on fracture toughness of {HSLA} steels. Materials Science and Engineering: A [Internet]. 2000 May;284(1–2):195–201. Available from: https://doi.org/10.1016%2Fs0921-5093%2800%2900739-5

20. Igwemezie V, Mehmanparast A, Kolios A. Materials selection for XL wind turbine support structures: A corrosion-fatigue perspective. Marine Structures [Internet]. 2018;61(May 2018):381–97. Available from: https://doi.org/10.1016/j.marstruc.2018.06.008

21. Jacob A, Mehmanparast A, Urzo R, Kelleher J. Experimental and numerical investigation of residual stress effects on fatigue crack growth behaviour of S355 steel weldments. International Journal of Fatigue [Internet]. 2019 Nov;128:105196. Available from: https://doi.org/10.1016%2Fj.ijfatigue.2019.105196

22. MEADinfo. Material Properties of S355 - An Overview [Internet]. 2015 [cited 2021 Feb 25]. Available from: https://www.meadinfo.org/2015/08/s355-steel-properties.html

23. Tata Steel. Structural Steel [Internet]. [cited 2021 Feb 25]. Available from: https://www.tatasteeleurope.com/ts/engineering/products/hot-rolled/structural-steel

24. Asia R steel. EN 10225 Chemical & Mechanical. 2014;(20):1055110.

25. Det Norske Veritas. Determination of Structural Capacity by Non-linear FE analysis Methods. Dnv-Rp-C208. 2013;DNV-RP-C20(June).

26. Forni D, Chiaia B, Cadoni E. High strain rate response of S355 at high temperatures. Materials & Design [Internet]. 2016 Mar;94:467–78. Available from: https://doi.org/10.1016%2Fj.matdes.2015.12.160

27. de Jesus AMP, Matos R, Fontoura BFC, Rebelo C, da Silva LS, Veljkovic M. A comparison of the fatigue behavior between S355 and S690 steel grades. Journal

of Constructional Steel Research [Internet]. 2012 Dec;79:140–50. Available from: https://doi.org/10.1016%2Fj.jcsr.2012.07.021

28. Pawliczek R, Prażmowski M. Study on material property changes of mild steel S355 caused by block loads with varying mean stress. International Journal of Fatigue [Internet]. 2015 Nov;80:171–7. Available from: https://doi.org/10.1016%2Fj.ijfatigue.2015.05.019

29. Mrozinski S, Piotrowski M. Effect of strain level on cyclic properties of S355 steel. AIP Conference Proceedings. 2016;1780(October).

30. Ulewicz R, Szataniak P, Novy F. Fatigue properties of wear resistant martensitic steel. METAL 2014 - 23rd International Conference on Metallurgy and Materials, Conference Proceedings. 2014;23(January 2014):784–9.

31. Klusák J, Seitl S. Very high cycle fatigue tests of high strength steels S355 J0 and S355 J2. Procedia Structural Integrity [Internet]. 2019;17:576–81. Available from: https://doi.org/10.1016/j.prostr.2019.08.077

32. HSE. Offshore technology report 2001/083 - Comparison of Fatigue Provisions in Codes and Standards. 2002; Available from: http://www.hse.gov.uk/research/otopdf/2001/oto01083.pdf

33. Mehmanparast A, Taylor J, Brennan F, Tavares I. Experimental investigation of mechanical and fracture properties of offshore wind monopile weldments: {SLIC} interlaboratory test results. Fatigue & Fracture of Engineering Materials & Structures [Internet]. 2018 May;41(12):2485–501. Available from: https://doi.org/10.1111%2Fffe.12850

34. Mehmanparast A, Brennan F, Tavares I. Fatigue crack growth rates for offshore wind monopile weldments in air and seawater: {SLIC} inter-laboratory test results. Materials & Design [Internet]. 2017 Jan;114:494–504. Available from: https://doi.org/10.1016%2Fj.matdes.2016.10.070

35. Altan T, Oh SI, Gegel HL. Metal Forming: Fundamentals and Applications. 1st Edition. American Society for Metals;

36. Cai Z-Y, Li M-Z, Lan Y-W. Three-dimensional sheet metal continuous forming process based on flexible roll bending: Principle and experiments. Journal of Materials Processing Technology [Internet]. 2012 Jan;212(1):120–7. Available from: https://doi.org/10.1016%2Fj.jmatprotec.2011.08.014

37. Amstead, B.H, Otswald PF, Begeman ML. Manufacturing Processes. 7th Edition. Austin: John Wiley & Sons; 1977.

38. Shin JG, Lee JH, Kim Y il, Yim H. Mechanics-based determination of the center roller displacement in three-roll bending for smoothly curved rectangular plates. {KSME} International Journal [Internet]. 2001 Dec;15(12):1655–63. Available from: https://doi.org/10.1007%2Fbf03185120

39. Yang M, Shima S. Simulation of pyramid type three-roll bending process. International Journal of Mechanical Sciences [Internet]. 1988 Jan;30(12):877–86. Available from: https://doi.org/10.1016%2F0020-7403%2888%2990071-9

40. Lie ST, Yang ZM, Gho WM. Validation of BS7910:2005 failure assessment diagrams for cracked square hollow section T-, Y- and K-joints. International Journal of Pressure Vessels and Piping [Internet]. 2009;86(5):335–44. Available from: http://dx.doi.org/10.1016/j.ijpvp.2008.11.015

41. Larrosa NO, Ainsworth RA, Akid R, Budden PJ, Davies CM, Hadley I, et al. 'Mind the gap' in fitness-for-service assessment procedures-review and summary of a recent workshop. International Journal of Pressure Vessels and Piping [Internet]. 2017;158:1–19. Available from: https://doi.org/10.1016/j.ijpvp.2017.09.004

42. EDF Energy. R6-Revision 4, Assessment of the integrity of the structures containing defects, Amendment 11. Transactions [Internet]. 2015; Available from: https://repository.lib.ncsu.edu/bitstream/handle/1840.20/33851/SMiRT-23_Paper_081.pdf?sequence=1&isAllowed=y

43. BS 7910. BSI Standards Publication Guide to methods for assessing the acceptability of flaws in metallic structures. BSI Standards Publication. 2015;(UK):490.

44. Anderson TL, Osage DA. API 579: A comprehensive fitness-for-service guide. International Journal of Pressure Vessels and Piping. 2000;77(14–15):953–63.

45. Wintle JB. Which Procedures for Fitness-for-Service Assessment: API 579 or BS 7910? In: International Conference on Pressure Vessel Technology. Vienna; 2003.

46. Furuya Y. Size effects in gigacycle fatigue of high-strength steel under ultrasonic fatigue testing. Procedia Engineering [Internet]. 2010;2(1):485–90. Available from: http://dx.doi.org/10.1016/j.proeng.2010.03.052

47. Shahani AR, Rastegar M, Botshekanan Dehkordi M, Moayeri Kashani H. Experimental and numerical investigation of thickness effect on ductile fracture toughness of steel alloy sheets. Engineering Fracture Mechanics [Internet]. 2010;77(4):646–59. Available from: http://dx.doi.org/10.1016/j.engfracmech.2009.12.017

48. Baek J hyun, Kim Y pyo, Kim C man, Kim W sik, Seok C sung. Effects of pre-strain on the mechanical properties of API 5L X65 pipe. Materials Science and Engineering A. 2010;527(6):1473–9.

49. Dzioba I, Lipiec S. Fracture mechanisms of S355 steel-experimental research, FEM simulation and SEM observation. Materials. 2019;12(23).

50. Wang Y, Zhao L, Cui X, Zhu X. Research on numerical simulation and process parameters of three-roll bending based on thickness characteristics of extra-thick plate. Advances in Mechanical Engineering. 2019;11(4):1–10.

51. Mehmanparast A. Prediction of creep crack growth behaviour in 316H stainless steel for a range of specimen geometries. International Journal of Pressure Vessels and Piping. 2014; 120: 55-65

3. A numerical analysis of the effects of manufacturing processes on material pre-strain in offshore wind monopiles

Satya Anandavijayan*, Ali Mehmanparast, Feargal Brennan

[a]*Offshore energy engineering centre, Cranfield University, MK43 0AL, UK*
[b]*Naval architecture and marine engineering, University of Strathclyde, G4 0LZ, UK*

Abstract

The majority of offshore wind turbines in Europe are supported by monopile type foundation structures. Monopiles are made of large thickness steel plates which are formed and then longitudinally welded to fabricate "cans" and these cans are subsequently welded around the circumference to manufacture a monopile. Monopile structures can have diameters of 4-10m, with wall thicknesses of 40-150mm. To achieve the cylindrical shape in individual cans, large thickness steel plates are typically cold formed via the three-roll bending process. During forming of these plates, the material is subjected to plastic pre-strain, which subsequently influences the fracture and fatigue properties of monopile structures. In this study, a finite element model has been developed to predict the pre-straining levels in monopiles of different dimensions. To determine the influence of numerous manufacturing practices, a sensitivity analysis of different factors has been conducted. These include fabrication dependent variables such as the influence of friction coefficient and bending force, and geometry dependent factors such as plate thickness, length, and distance between rollers. From the numerical results, a range of expected material pre-strain levels have been identified and presented in this paper.

Peer-review under responsibility of the ECF22 organizers.

Keywords: material pre-strain; monopile; fatigue; fracture; S355; finite element analysis; three roll bending

3.1 Introduction

Renewable energy is predicted to be one of the fastest growing maritime sectors. Currently, wind energy already meets 11% of the EU's power demand and is predicted that by the year 2030, its installed capacity will reach up to 23% of Europe's total electricity demand (European Wind Energy Association, 2017). For this to be technically feasible, it is crucial for new offshore concepts and designs to be developed in order to

utilize the deeper, larger expanses and wind potential of areas such as the Mediterranean, Atlantic and North Sea waters (European Wind Energy Association, 2013).

Monopiles are the most common support structures of offshore wind turbines (Leite, 2015). A monopile is essentially a steel tube which is fixed into the seabed. Its main advantage is its simplistic design and production, and thus its low unit cost. As a result, it is the most widely used offshore wind structure (Schaumann & Boker, 2005). Monopile manufacturing is conducted in two phases. The first phase is rolling, the second phase is welding. Plates of steel are hot rolled and then these can then be cut to size (Kumar, et al., 2016). A roller is then applied to the steel plates to induce bending of the steel via cold rolling processes (Figure 7). The plates are then welded together to form the cylindrical cans. These sections are then circumferentially welded together, until the desired length of the monopile is achieved. These steps are achieved onshore, to save time and money during the offshore installation process (Leite, 2015). Roll bending, also known as three-roll forming (called the pyramid type) or plate bending, is the process of giving a curvature to a sheet/bar/shaped section by bending it between two or three adjustable cylindrical rolls. Common applications of this procedure are in making cylinders for pressure tanks, boilers, corrugate pipe, structural sections for submarines, aircraft, and nuclear reactors (Altan, et al., 1983).

This process is known as a continuous manufacturing process, meaning that local deformation is moving over the entire plate, and at any instant only a small region is being formed. It is suitable for small batch or single products due to its low set-up cost. However, it is time consuming. To overcome this, three rollers are introduced into the process to manufacture a doubly curved plate. This ensures that the deformation is within a local contact region below the centre roll, and the plate is rolled within one pass. (Cai, et al., 2012). In step one, the blank plate is fed into the machine via two side rollers until the plate is positioned properly. In step two, the centre roller is lowered onto the plate, thus bending it. The third step involves the two side rollers rotating so that the plate is being bent continuously. During this step, it is ensured the whole plate is bent equally through the rollers to ensure all points undergo the same stress and strain history (Shin, et al., 2001). The rolls are employed as a forming tool to generate curvature in the longitudinal and transverse directions simultaneously. The metal plate is bent by the configuration of the rollers. In the longitudinal direction, the upper and lower rolls bend

the plate downwards (Cai, et al., 2012). The longitudinal deformation is dependent upon the vertical positioning of the upper roller in relation to the lower rollers and thus the basic forming principle is the three-point bending of a plate. As the plate moves from right to left, it forms contact points with the three rollers. Thus, the plate can be split into three regions by their contact points: the formed region, the deformation region, and undeformed region. In Figure 7, the deformation region AC is a plate and includes a loading region AB and unloading section BC. In the loading area, the bending moment increases from zero (at point A) to its maximum at point B. During this, the longitudinal curvature of the plate increases from zero to its maximum K_{Lmax}. In the unloading area, the curvature is decreased from point B to point C, and the bending moment decreases (Yang & Shima, 1988).

In this work, numerical investigations regarding the effects of the three-roll bending manufacturing process on the plastic strain levels in offshore wind monopiles have been conducted. By estimating the range of plastic pre-strain present, the subsequent effects on the structural integrity of offshore wind monopiles can be estimated. In future work, the results of this work will be accounted for in engineering critical assessments.

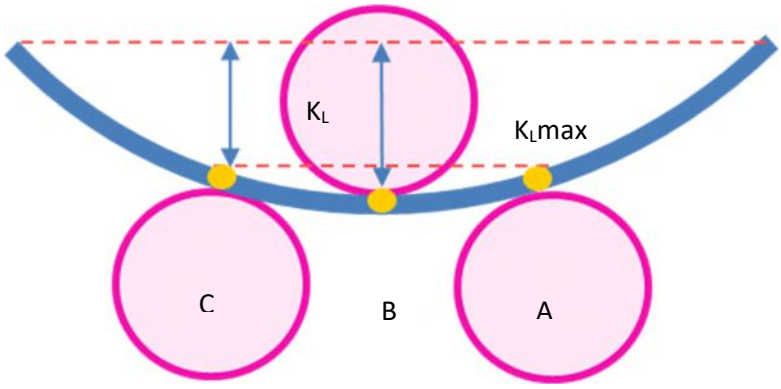

Figure 7 – Schematic of three roll bending process

Nomenclature

$\sigma\|_0$	yield stress
ε_p	plastic strain
γ	material coefficient

c	length of plate
C	material coefficient
d	deflection
E	Young's Modulus
K_{Lmax}	maximum curvature
R	radius

3.2 Finite Element Model

3.2.1 Dimensions and Material Properties

Static bending simulations were run on a symmetrical quarter symmetry model of the three-roll bending set up. The top and bottom rollers were modelled with 1m diameter and 3m roller length. The distance between the rollers was 2m.However, in the roller diameter simulation, the diameter of the rollers were changed by +/- 0.2m to determine the sensitivity of S355 to this change. The plate was modelled with a thickness of 60mm, as this thickness is commonly used for offshore wind monopile structures and is therefore a realistic assumption. In plate thickness simulations, the plate thickness varied between 55m and 65mm to determine the sensitivity of the plastic strain within the plate to this change.

The material used in this work is S355 structural steel which is widely used in the fabrication of monopiles. The material properties were gathered from experimental data from previous work, and calculating the required parameters (Mrozinski & Piotrowski, 2006). The Young's modulus was calculated from literature values (de Jesus, et al., 2012). As recommended in the Abaqus documentation, the combined isotropic/kinematic hardening model was used (Abaqus documentation). The kinematic hardening behaviour was characterised using the parameters $\sigma|_0$, *C*, and γ where $\sigma|_{0\ is}$ the yield stress of the material, while C and γ are material coefficients. The yield stress of the material was taken as 400 MPa in this study.

The hardening law can be expressed as:

$$\propto_k = C_k \frac{1}{\sigma^0}(\sigma - \alpha)\dot{\varepsilon}^{-pl} - \gamma_k \alpha_k \dot{\varepsilon}^{-pl}$$

Equation 30 – Kinematic hardening model

Where the overall backstress is calculated as:

$$\propto = \sum_{k=1}^{N} \propto_k$$

Equation 31 – Calculation of backstresses

Where: σ^0 is the yield surface size, N is the number of backstresses, C_k and γ_k are material parameters. The initial kinematic hardening modulus is defined as C_k, while γ_k determines the rate at which the modulus decrease/increases with increasing plastic strain.

The isotropic hardening component can be defined as:

$$\sigma^0 = \sigma|_0 + Q_\infty(1 - e^{-b\varepsilon^{-pl}})$$

Equation 32 – Isotropic hardening model

Where: $\sigma|_0$ is the yield stress at zero plastic strain, Q_∞ and b are material parameters.

For the purpose of the simulation, the following material parameters were taken from a previous work involving S355 (Albani, 2017).

Table 2 – Material parameters used in Abaqus

$\sigma\|0$ [MPa]	C/γ [MPa]	C [MPa]	γ	Q_∞ [MPa]	b
400	215	387	1.8	340	45

Boundary conditions were applied on the rollers, as the plate was assumed to not be fixed. The bottom set of rollers were assigned ENCASTRE (U1 = U2 = U3 = UR1 = UR2 = UR3 = 0) boundary conditions. The upper roller was assigned displacement/rotation boundary conditions. In the initial step, the upper roller was assigned a displacement rotation boundary condition.

3.2.2 Element Type, Mesh Sensitivity Analysis, and Validation

The plate was meshed using C3D8R elements. The rollers were meshed using discrete rigid elements. It is best practice to identify the correct balance of mesh density before any finite element analyses are undertaken. This is useful as the accuracy of results may be dependent on the density of the mesh. Too coarse a mesh can give inaccurate results,

whereas a mesh which is too fine may unnecessarily increase the computational time required to run a simulation. Therefore, a mesh sensitivity analysis was carried out.

The mesh of the entire geometry was refined in both the longitudinal (lengthwise) and transverse (through thickness) directions to increase the number of elements and nodes and thus the mesh density as seen in figure 8. A partition was created 1m either side of the node of the contact point of the roller (2m in length in total). This partition was then meshed using double bias picking, so that the elements would be most concentrated towards the centre.

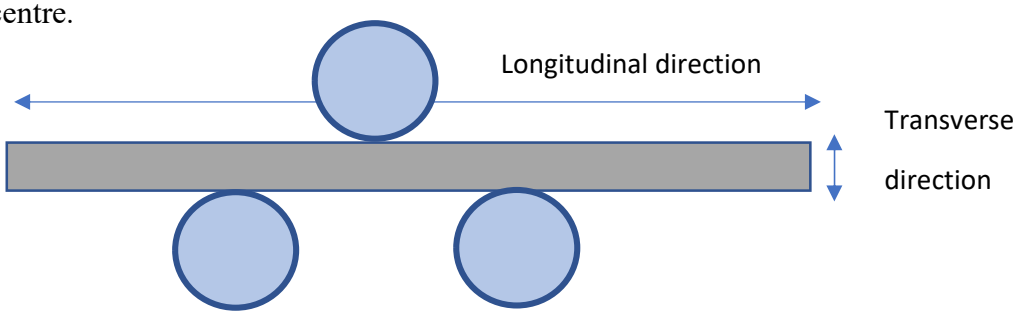

Figure 8 – Longitudinal and transverse directions of FE geometry

The mesh was refined by increasing the number of elements and the simulation was run and rerun at varying mesh intensities. A path was created in both the longitudinal direction (at y = 0), and in the transverse direction to plot the values from the mesh sensitivity analysis at the same points. Once the results had converged on the graphs, it was assumed that the optimum mesh density for each model had been identified correctly. From the mesh sensitivity analysis, it was concluded that the optimum mesh density was 68073 elements for the whole model. This was obtained when the element size in the regions of interest was reduced to 0.001m. At the areas of contact, a denser mesh was generated using single bias picking.

The FE model was validated via the use of hand calculations. A simple three point bending calculation was conducted and the stress results from the finite element simulation were compared to those from the hand calculation. Good agreement ensured that the model was valid and working correctly.

3.3 Results and Discussion

The sensitivity cases investigated were the effects of loading, friction coefficient, distance between the bottom rollers, roller diameter, plate thickness and plate length.

Loading cases were run by applying load in the range of 500-900 kN on the plate via the top roller. A friction coefficient of 0.2 was maintained and all dimensions were kept constant. As seen in Figure 9, at the lowest load level of 500kN examined in this study the plastic strain present is minimal as expected, whereas between 800 kN – 900 kN, the plastic strain levels increase by 200% and reach maximum values of 1.41% in tension and -1.41% in compression. The effects of altering the friction coefficient were analysed by subjecting the model to the highest load level of 900 kN (Figure 11). For metal forming processes, the friction coefficient is usually around 0.2-0.3 (Z Marciniac, et al., 2002) (Chudasama & Raval, 2015). The simulations results show similar trends when different values of friction coefficient were employed in the analysis. However, increasing the friction coefficient from 0.2 to 1.0 decreased the plastic tensile strain from 1.42% to 1.18%, giving a reduction in plastic strain which is approximately 17%.

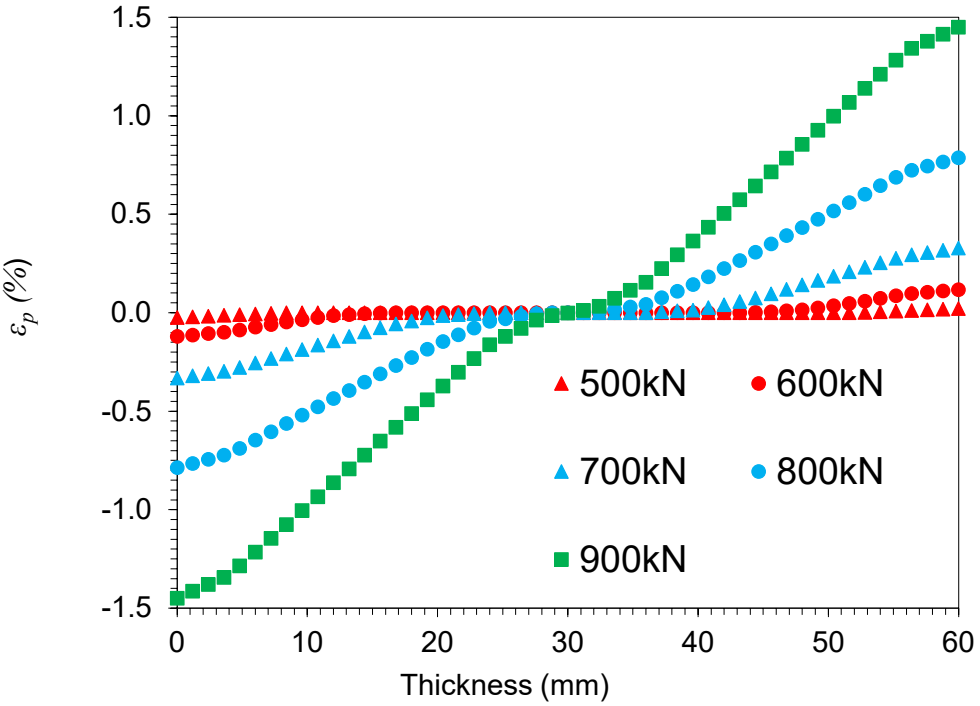

Figure 9 – Effect of loading on plastic strain level along plate thickness

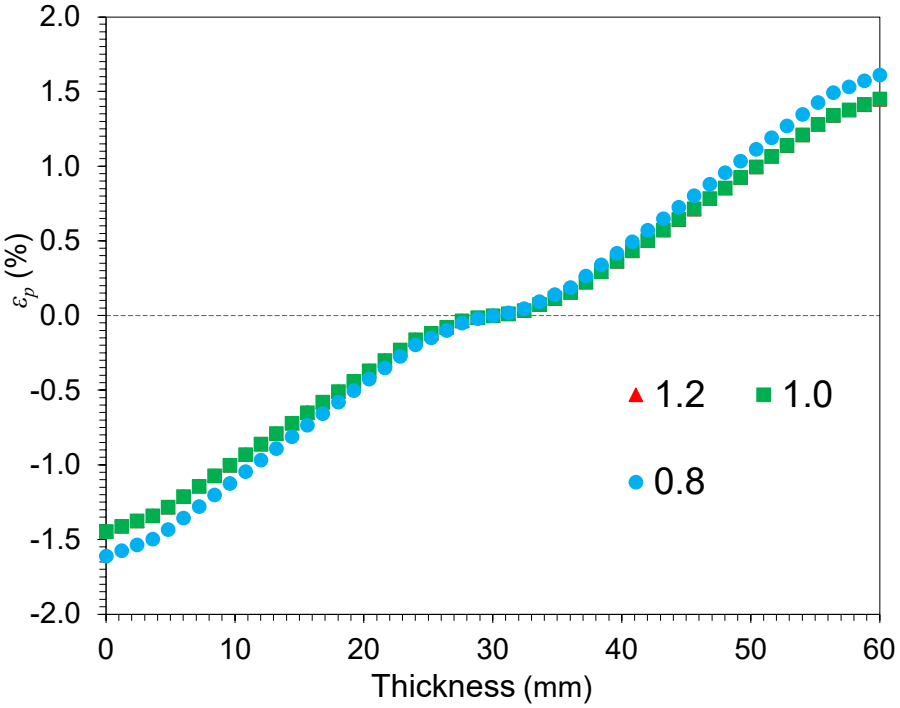

Figure 10 – Effect of roller diameter on plastic strain across the plate thickness

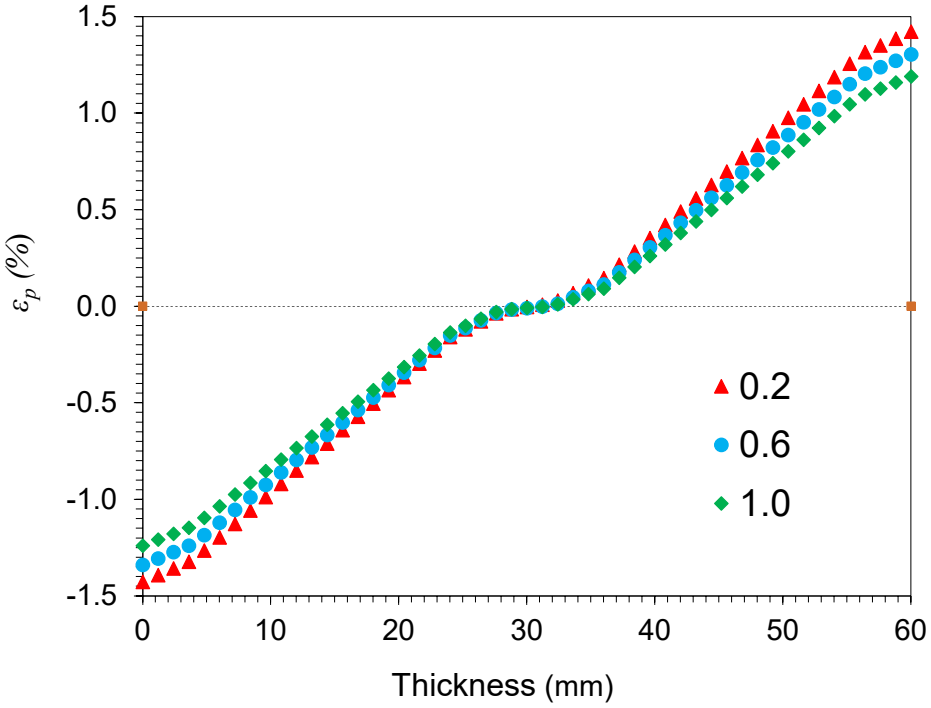

Figure 11 – Effect of friction coefficient on plastic strain level along the plate thickness

The roller diameter was increased from 1m to 1.2m for one of the cases, and decreased from 1m to 0.8m for another. The load level for the simulation was set at 900 kN at a friction coefficient of 0.2, and the thickness of the plate remained as 60mm. The distance between the two bottom rollers remained at 1m. Decreasing the roller diameter by 0.2m resulted in the plastic strain increasing from 1.44% to 1.6%, which is a 10% increase in plastic strain. Increasing the roller diameter by 0.2m resulted in a very minimal decrease in plastic strain. This suggests that changing the roller diameter will not play a significant part in altering the pre-strain level of S355 plates. The length of plate hanging past the bottom rollers was increased to determine if this had any effect on the plastic pre-strain levels (Figure 12). This case was run to determine if the plate length would affect the plastic strain level during the fabrication process. It was noticed that increasing the length of plate extending from the roller can result in a decrease in plastic strain levels. As the plate length increased the overall mass of the plate increased making it more difficult to bend in compression. Thus, a decrease in plastic strain was observed. Increasing the

overhang of sheet from 1m to 3m can reduce the plastic strain by approximately 22%, from a tensile plastic strain of 1.45% to 1.18%.

The bottom rollers were moved from a distance of 2m between the rollers, to 2.5m and 3m. The diameter of the rollers and the plate were unchanged, and the friction coefficient was kept at 0.2. The load level used for the simulation was 900 kN. From the finite element results, it can be concluded that re-positioning the bottom rollers to create more distance will not significantly affect the level of plastic strain present in the material (Figure 13).

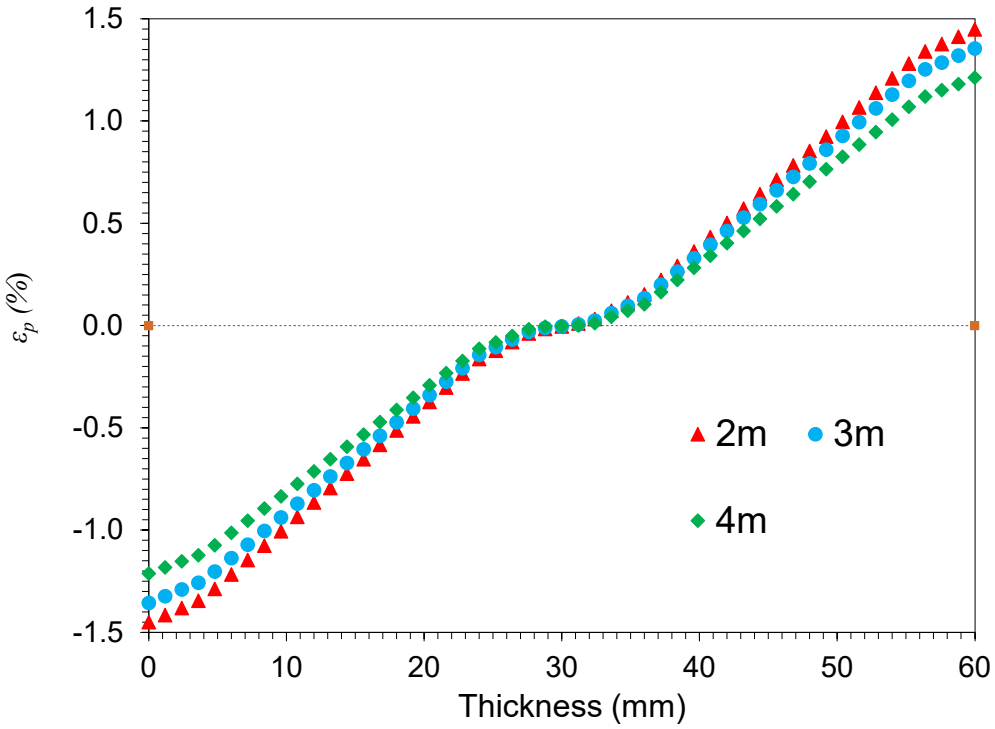

Figure 12 – Effect of plate length on the plastic strain through the thickness of the plate

The maximum plastic strain in tension was 1.45%, and -1.45% in compression.

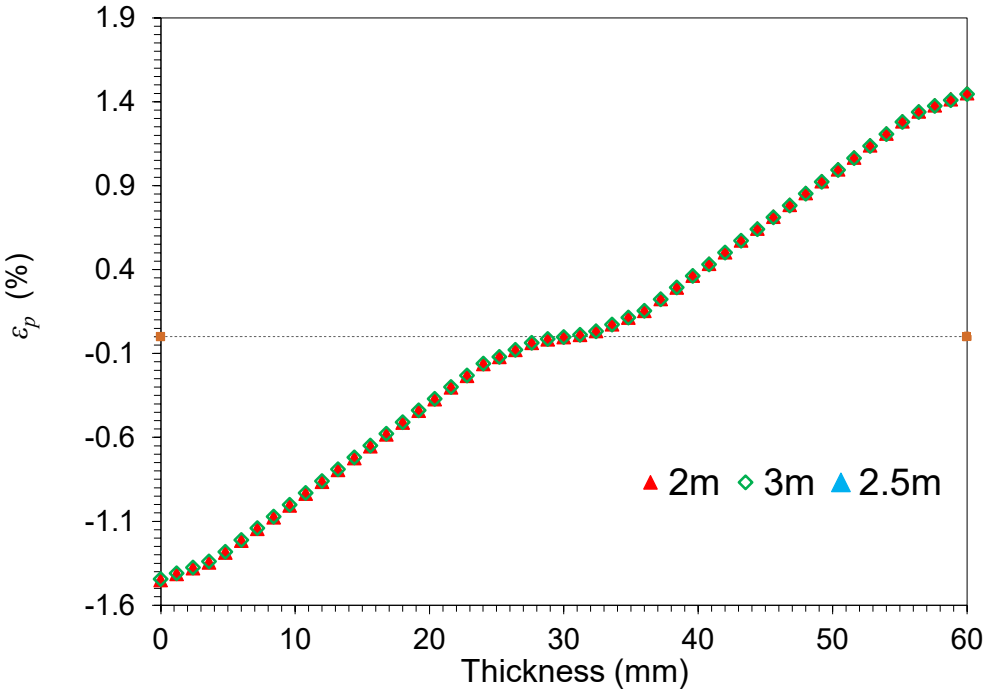

Figure 13 – Effect of the distance between the bottom rollers on the plastic strain level across the thickness

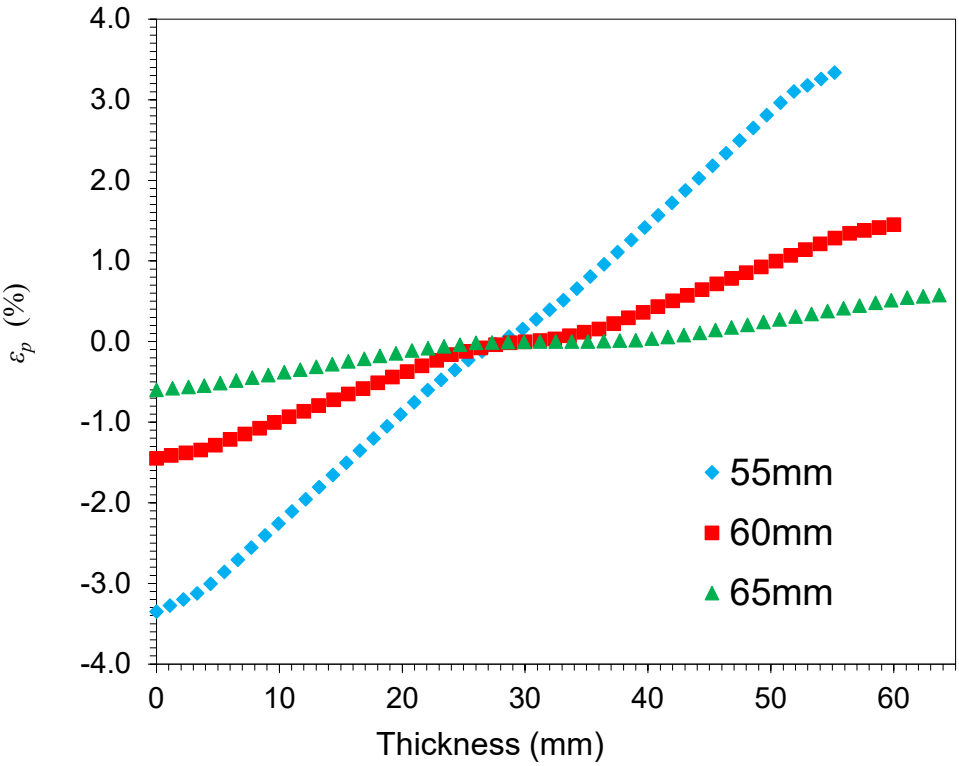

Figure 14 - Effect of the thickness of plates on the plastic strain level

The plate thickness was altered from 60mm to 55mm and 65mm, and were subjected to a load of 900kN. The friction coefficient was maintained at 0.2 and all dimensions were kept constant. From the simulations, a 60mm plate thickness when subjected to a load of 900kN gives a maximum tensile plastic strain of 1.45%. Reducing the wall thickness by 5mm results in an increase in plastic strain by 190%. Increasing the wall thickness by 5mm resulted in a reduction in plastic strain by 245%. From these results it can be seen how significant a 5mm difference in plate thickness can make a significant difference in plastic strain level (Figure 14). The displacement outputs from the simulations were used to calculate the radius of curvature and the corresponding maximum possible diameter from these results (Table 3). Displacement values were taken from cases run at a load level of 900kN, with a friction coefficient of 0.2. The distance between the rollers remained at 2m. The equation used to calculate the radius was:

$$R = \frac{c^2 + 4d^2}{8d}$$

Equation 33 – Equation to calculate the radius of curvature from displacement

Where c is the distance between the rollers, d is the displacement, and R is the radius.

Table 3 - Radius of curvature for corresponding wall thickness

Wall Thickness (mm)	**Radius (m)**
55	2.15m
60	4.30m
65	8.12m

From the results in Table 3, it can be noted that with each 5mm increase in wall thickness, the radius of curvature will halve. Further studies will be conducted in future work to examine the load level effects on radius of curvature. From the overall results, the maximum plastic strain range obtained from of finite element cases from load levels, friction coefficients, and distance between rollers considered was from -1.6% to 1.6% for S355 steel. However, in the case for wall thicknesses, the maximum plastic strain range was from -3.3% to 3.3%

3.4 Conclusions

The results from this study have demonstrated how the fabrication and manufacturing processes can affect the resulting plastic strain values in material S355. Load levels of 500kN result in minimal plastic strain present in the material, however, increasing the load level up to 900kN increases the plastic strain present to 1.41%. Increasing the friction coefficient from 0.2 to 1.0 resulted in a decrease in plastic strain values by 13%. Decreasing the roller diameter by 0.2m resulted in a 10% increase in plastic strain, however, increasing the roller diameter had minimal effects on the plastic strain levels. Increasing the plate length resulted in an overall increase in plastic strain levels. The most significant change in plastic strain level was obtained by changing the wall thickness. Reducing the wall thickness by 5mm resulted in an increase in plastic strain by 190%, while increasing the wall thickness resulted in a plastic strain decrease of 245%. Altering the wall thickness also affected radius of curvature at a load level of 900kN, with a 5mm increase in wall thickness halving the overall radius, and a 5mm decrease doubling in overall radius.

3.5 References

Abaqus Analysis User's Manual (6.10), Classical Metal Plasticity

Albani, P., 2017. Experimental and Numerical Investigation of Corrosion Fatigue in Offshore Weldments. Cranfield University

Altan, T., Oh, S.-l. & Gegel, H. L., 1983. Metal Forming: Fundamentals and Applications. 1 ed. Metals Park: American Society for Metals.

Cai, Z. Y., Li, M. Z. & Lan, Y. W., 2012. Three-dimensional sheet metal continuous forming process based on flexible roll bending: Principle and experiments. Journal of Materials Processing Technology, Volume 212, pp. 120-127.

Chudasama, M.K, Raval H.K. Comparative Study of Static and Dynamic Bending Forces during 3-Roller Cone Frustum Bending Process. World Academy of Science, Engineering and Technology, Volume 9, pp 1097-1100.

de Jesus, A. M. et al., 2012. A comparison of the fatigue behavior between S355 and S690 steel grades. 79(140-150).

European Wind Energy Association, 2017. Driving Cost Reductions in Offshore Wind, Cork: Leanwind.

Kumar, L., Majumdar, S. & Sahu, R. K., 2016. Measurement of the Residual Stress in Hot Rolled Strip using Strain Gauge Method, Raipur: NIT Raipur.

Leite, O. B., 2015. Review of Design Procedures for Monopile Offshore Wind Structures, Porto: Universidade Do Porto.

Mrozinski, S., Piotrowski, M., Skibicki, D., 2016. Effect of strain level on cyclic properties of S355 steel. AIP Conference Proceedings 1780, 02005.

Schaumann, P. & Boker, C., 2005. Can Jackets and Tripods Compete With Monopiles? Contribution to Copenhagen Offshore Wind, pp. 1-10.

Shin, J. G., Lee, J. H., Kim, Y. I. & Yim, H., 2001. Mechanics-Based Determination of the Center Roller Displacement in Three-Roll Bending for Smoothly Curved Rectangular Plates. KSME International Journal, 15(12), pp. 1655-1663.

Yang, M. & Shima, S., 1988. Simulation of Pyramid Type Three-Roll Bending Process. International Journal of Mechanical Science, 30(12), pp. 877-886.

Z Marciniac, JL Duncan, SJ Hu, 2002. "Mechanics of sheet metal forming", 2nd Edition, Butterworth-Heinemann

4. Material pre-straining effects on fracture toughness variation in offshore wind turbine foundations

Satya Anandavijayan[1], Ali Mehmanparast[1]*, Feargal Brennan[2] and Amir Chahardehi[3]

[1] Offshore Renewable Energy Engineering Centre, Cranfield University, MK43 0AL, UK

[2] Naval Architecture, Ocean & Marine Engineering Department, University of Strathclyde, G4 0LZ, UK

[3]Atkins Energy, Westminster, London, SW1E 5BY, UK

*Corresponding author: a.mehmanparast@cranfield.ac.uk

Abstract

S355 structural steel is a commonly used material in the fabrication of foundation structures of offshore wind turbines, which are dominantly supported using monopiles. During the manufacturing process of monopile foundations, S355 steel plates are pre-strained via a three-point bending and rolling process, which subsequently changes the mechanical, fatigue and fracture properties of the material. The aim of this study it to investigate the variation in fracture toughness of S355 material by considering a range of pre-strain levels induced during the manufacturing process. Fracture toughness tests have been performed on compact tension specimens made of the as-received, 5% and 10% pre-strained S355 material. The test results have shown that the fracture toughness of the material decreases as the percentage of pre-straining increases. An empirical correlation has been derived between the yield strength of the material, the plastic pre-strain level and the fracture toughness values. The drawn relationship can potentially be utilised in the life assessment of offshore wind turbine monopile foundations to give a relatively accurate estimate the remaining life by considering realistic values of fracture toughness post-fabrication, which results in better informed design and assessment.

Keywords: fracture toughness, S355, offshore wind, material pre-straining, manufacturing effect

Nomenclature

a	Crack length
a_0	Initial crack length before pre-cracking
a_i	Crack length after pre-cracking
a_f	Final crack length after fracture toughness testing
Δa	Increment of crack growth
Δa_{max}	Maximum allowable crack extension in fracture toughness tests
B	Specimen thickness
B_e	Effective thickness

B_n	Specimen net thickness between side grooves
b_0	Uncracked ligament, (W-a_0)
C_0	Unloading compliance
E	Young's Modulus
E_M	Effective Young's modulus in fracture toughness data analysis
J_{IC}	Critical value of J for fracture under Mode I loading conditions
W	Specimen width
η	Factor relating J to load and displacement measurements
$\sigma_{0.2}$	0.2 % proof stress
σ_{UTS}	Ultimate tensile stress
σ_y	Yield stress
ε_p	Plastic strain

4.1 Introduction

Offshore wind is a rapidly maturing industry and is currently one of the leading sources of renewable energy for electricity production, with the EU aiming to reach 100GW of offshore wind capacity by 2030 [1,2]. The UK has made an ambitious plan to generate 40GW of electricity from offshore wind energy by 2030 [3]. This push for an increase in installed offshore wind capacity has been driven by the evidence of [4] climate change, thus not only the UK government but also many other governments have decided to look into renewable sources for reducing CO_2 emissions [2]. As a result of this, the offshore wind industry is continuously developing wind farms of higher capacities and looking to install them in deeper waters [5,6].

Foundation support structures and their design requirements are an important aspect to be considered in the future development of offshore wind projects [7,8]. There are many different types of support structures to be considered for offshore wind structures, the most common types being gravity based structures (GBS), monopiles, tripods, jackets and floating structures [9]. Monopile structures are a single cylindrical tube structure that are fixed into the seabed, and thus are the simplest technical solution for shallow waters of up to 25 m. Tripods are three-legged support structures connected to a frame of a central pipe that sits on top of a tripod frame structure. Tripods can use either piles or

suction bucket anchors. Due to its wide base, this structure has a large resistance against overturning. Jacket structures are very similar to tripod structures and consist of three or four legs connected to each other via slender braces, and then are piled into the seabed. This system has been adapted from oil and gas concepts, which have been previously used for decades. Floating structures are still in early stages of development and are set to be utilised in deeper waters. There are numerous floating structure concepts which are being developed and adapted from the oil and gas industry, which are starting to yield good results [10–13].

Most offshore wind developers have selected monopiles in the last decade due to its simple design and production, and thus low unit cost [10,14]. Monopile support structures are installed into the seabed and during their service life they are subjected to corrosion-fatigue damage due to the constant exertion of wave, wind and current forces in the corrosive environments [4,15–20]. An important issue to be considered in the structural integrity assessment of offshore wind monopile structures is the influence of material pre-straining, introduced into the structures during fabrication processes, on the mechanical response and fracture behaviour of the material. The manufacture of monopiles is conducted in three phases: rolling, bending, and welding. S355 plates are firstly hot rolled, before being cut to size [21]. These plates are then cold rolled into cylindrical cans via the three point bending process, which involves a roller being applied to induce bending of the steel, and then longitudinally welded [22]. These individual cans are then circumferentially welded together until the desired monopile length is achieved [22]. This process is a continuous manufacturing process, and has a low set-up cost [22]. As a result of the monopile fabrication process, a range of plastic strain levels can be found across the wall thickness, ranging from compressive to tensile [22].

From previous research studies it has been understood that varying levels of plastic pre-strain can affect the mechanical and fracture properties of steel. For many metallic materials it has been observed that material pre-straining results in a reduction in the fracture toughness properties of the material [23]. The effects of material pre-straining is a topic of research within the pipelines industry, as pipelines can be permanently plastically deformed via force (for example in dents), or due to subsidence, frost heave or earthquake/seismic loading during service [24,25]. In a study conducted by Sivaprasad *et.al.* [26], HSLA-80 and HSLA-100 steels were pre-tensioned and fracture toughness

testing was conducted. From the results it was concluded that HSLA steels did not show any significant changes in fracture toughness up to a plastic strain of 2%, however pre-straining over 2% presented a deterioration in fracture toughness for HSLA steels [27]. The effects of plastic pre-compression on the fracture toughness of 316H steels was investigated by Mehmanparast *et.al* [28–30]. In their study 316H stainless steel was pre-compressed to 8% plastic strain and fracture toughness tests were performed. From the results it was concluded that there was a decrease in fracture toughness values in the pre-compressed material compared to the as-received material state. Liaw and Landes reported similar results for both 316 and 4340 steels where both materials were monotonically pre-tensioned to 2% and 5% and fracture toughness tests were performed [31].

Previous works from other researchers suggest that pre-straining the metals results in a change in the mobile dislocation density and this can control the fracture toughness in metallic materials [32-38]. As metals are pre-strained, the dislocation structure and distribution is altered [36]. Dislocation density generally increases with pre-straining, and this can result in a higher yield strength and lower ductility [37]. In some instances, dislocation density can decrease at low pre-straining levels, due to the destruction of localised dislocation. With increasing pre-straining, new dislocations start forming which therefore increases the dislocation density [38], however the formation of small voids may induce fracture and therefore pre-strained material exhibits a lower fracture resistance [29].

The same effect will be present at varying levels of plastic-pre-strains across the thickness of monopile structures, however there is very little information on the fracture behaviour of S355 steel with relation to material pre-strain. In order to gain an insight into the implications of material pre-straining on monopile structures, an experimental programme has been devised. As the worst case scenario is being investigated, pre-strain levels that have been investigated are only from the tensile regions for this particular project, assuming that tensile pre-strain results in similar or more detrimental effects on the fracture toughness compared to compressive pre-strains. In addition, in the context of offshore wind monopile structures, the face subjected to wind and wave loads will have been pre-strained in tension. Therefore, in this work the effect of material tensile pre-straining levels of up to 10% on fracture properties of S355 structural steel has been

investigated. Although previous finite element work suggests pre-straining levels of up to 3% are observed during the fabrication of monopile cans, pre-strains of up to 10% have been accounted for more extreme scenarios based on individual fabricators methods which were not investigated during the finite element study.

4.2 Material Pre-Conditioning and Specimen Preparation

The material used in this work is S355G10+M structural steel, which is widely used in the manufacture of offshore wind monopile structures. The chemical composition of the material used in this study is shown in Table 4. All specimens examined in this study were extracted from the mid-thickness of a 90 mm wide, 16mm thick S355G10+M plate.

Table 4 - Composition wt% of S355G10+M

C	**Mn**	**Si**	**Cu**	**N**	**P**	**S**	**Cr**	**Ni**	**Mo**	**V**
0.061	1.58	0.280	0.254	0.0041	0.0013	0.0007	0.034	0.342	0.06	0.001
Nb	**As**	**Sn**	**Ti**	**Pb**	**B**	**Sb**	**Ca**	**Bi**	**Al-T**	
0.022	0.003	0.001	0.003	0.000	0.0003	0.0010	0.0028	0.0001	0.032	

To investigate the effects of material pre-straining on mechanical properties and fracture behaviour of the material, three material states were considered: (1) As-received (also known as the base metal with 0% plastic strain), (2) uniformly pre-tensioned material to 5% plastic strain, and (3) uniformly pre-tensioned material to 10% plastic strain. These pre-strain levels were chosen to investigate the effects of material pre-strain on fracture toughness of S355 over the examined stress range applied during the monopile fabrication process detailed in [22]. In addition, considering a wide range of pre-straining will result in a more conservative defect assessment in structural integrity procedures, thus allowing a larger margin for error. In order to conduct experiments to determine the influence of material pre-strain, the material had to be uniformly plastically pre-strained first at room temperature, as shown in Figure 15. The level of material pre-strain was estimated from the tensile curves obtained, by deducting the elastic strain from the total strain and pre-tensioning the material to the corresponding stress levels for 5% and 10% pre-strain to be attained.

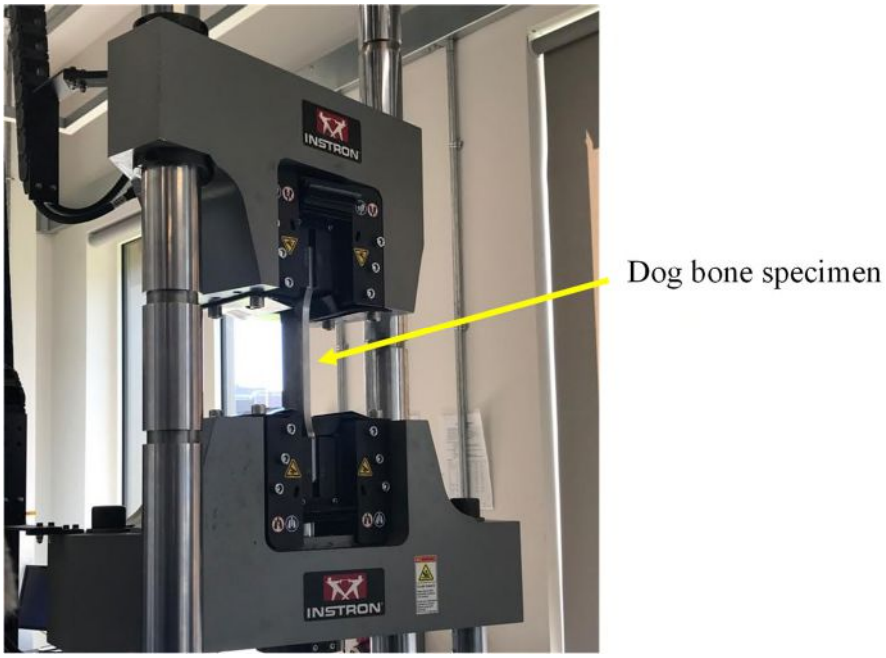

Figure 15 - Dog bone specimen undergoing pre-tensioning

In order to quantify the tensile properties of the material, for each pre-strain level (i.e., 0%, 50% and 10%) two tensile tests were conducted on dog bone shape specimens extracted from the uniformly pre-strained material. The dog bone specimens for tensile tests had the thickness of 11 mm, width of 36 mm and gauge length of 48 mm. The "engineering stress *vs.* engineering strain" obtained from these tensile tests are graphically presented in Figure 16 and the average values of mechanical properties obtained from two tests at each pre-strain level have been summarised in Table 5. From the table it can be seen that while the elastic Young's modulus, E, has slightly increased by increasing the pre-strain level, there is an increase in the ultimate tensile strength, σ_{UTS}, and the yield stress of the pre-tensioned materials, σ_Y, as expected. In this study, the yield stress is defined as the lowest value of yield in the non-linear (which is also discontinuous in the case of 0% pre-strain material) region of the tensile curves. Moreover, a 2% decrease in the axial strain at failure, ε_f, is also noticed between each pre-strain level. In general, it can be seen in Table 5 and Figure 16 that increasing the material pre-strain level increases the yield stress and decreases the failure strain of the material.

Table 5 - Average mechanical properties of as-received and pre-strained materials

Tensile pre-strain level	E (GPa)	σ_Y (MPa)	σ_{UTS} (MPa)	ε_f (%)
0%	222	417	517	51
5%	255	468	532	49
10%	264	516	545	47

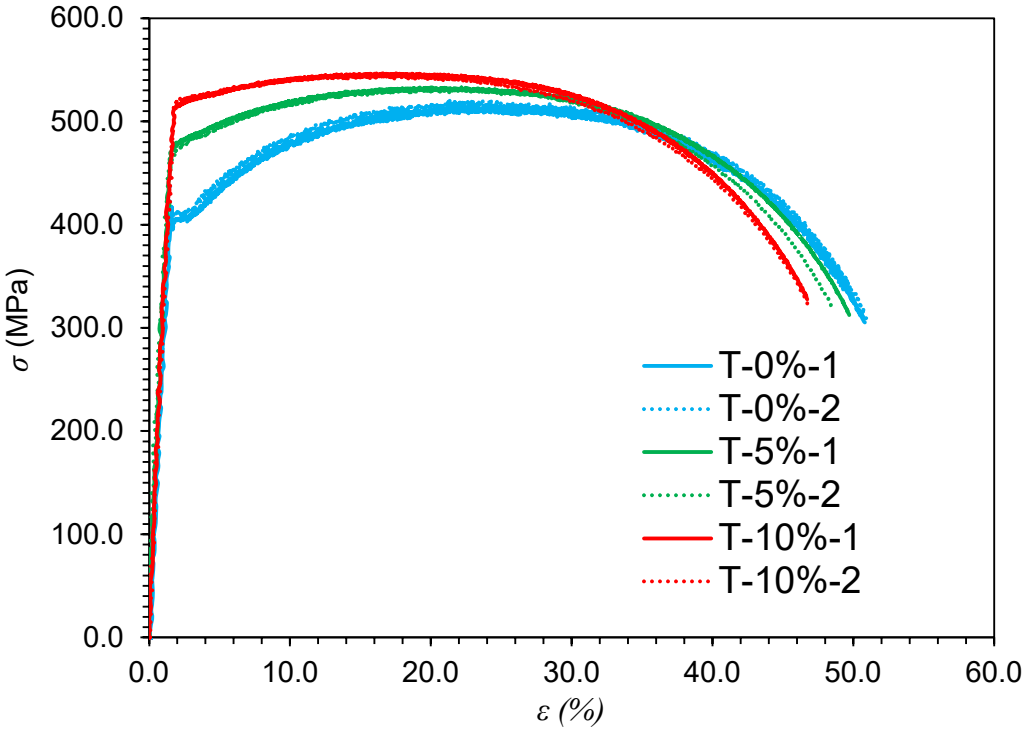

Figure 16 - Stress-Strain curves for 0%, 5% &10% pre-strained materials

The tensile tests performed in this study were conducted in conjunction with digital image correlation (DIC) measurements to monitor the strain variations during the tests. DIC is an optical method of measuring displacements and strains on engineering materials subjected to different loading conditions. The technique involves spraying the specimens with a speckle pattern which are used as reference points by the DIC software. The DIC software then tracks the movements of the speckle patterns and the output from DIC will map the displacements of these speckles which can then be converted into strains. For this work, the software used was Istra 4D to view the strain maps and process the output data. DIC measurements on initial tests showed that pre-straining is consistent across the gauge region during the tensile tests before any necking occurs in the test specimen. Moreover, it was ensured that the specimens were lit adequately while DIC strain

measurements were conducted. The contour plots of the axial strain distribution along the loading direction for 0%, 5% and 10% pre-strained specimens at the stress level of 500 MPa are shown in Figure 17, Figure 18 and Figure 19, respectively. From the images it can be seen that the strain in the gauge region of the 0% material is much higher compared to the strain contours for 5% and 10% material. This is due to the fact that the lower pre-strain material has a lower yield stress, which has resulted in larger plasticity hence greater strain values at 500 MPa in the as-received material compared to 5% and 10% pre-strained specimens. Also comparing the strain distribution maps in Figure 18 and Figure 19 it can be seen that at 500 MPa, the material with 10% pre-straining has exhibited lower strain levels compared to the 5% pre-strained material. This is due to the material hardening effect which has occurred by increasing the pre-strain level from 5% to 10%.

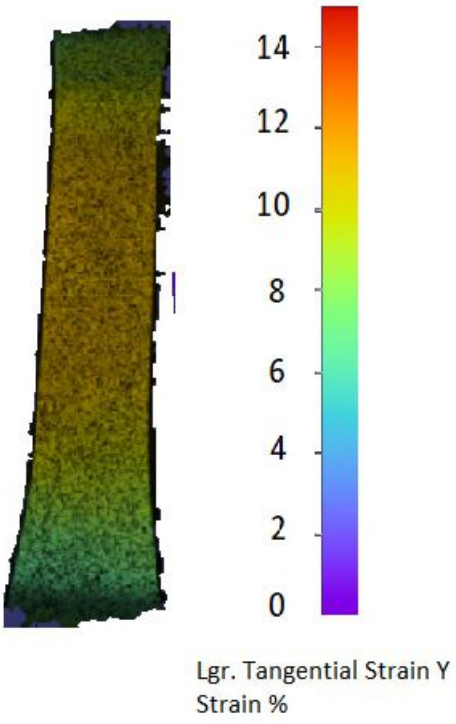

Figure 17 – Axial strain map of 0% pre-strained specimen at 500MPa

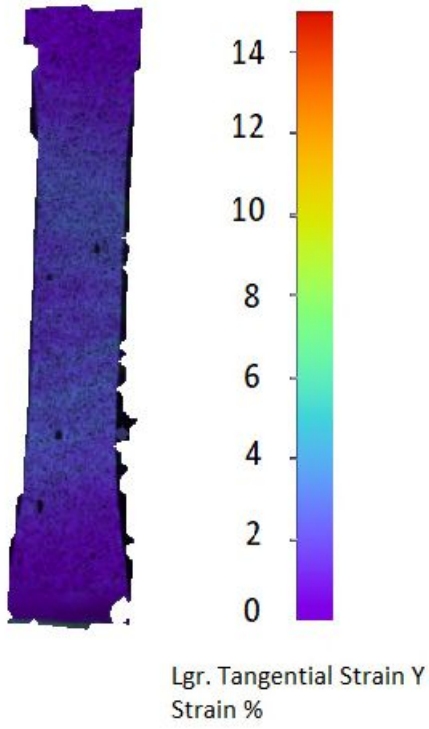

Figure 18 – Axial strain map of 5% pre-strained specimen at 500MPa

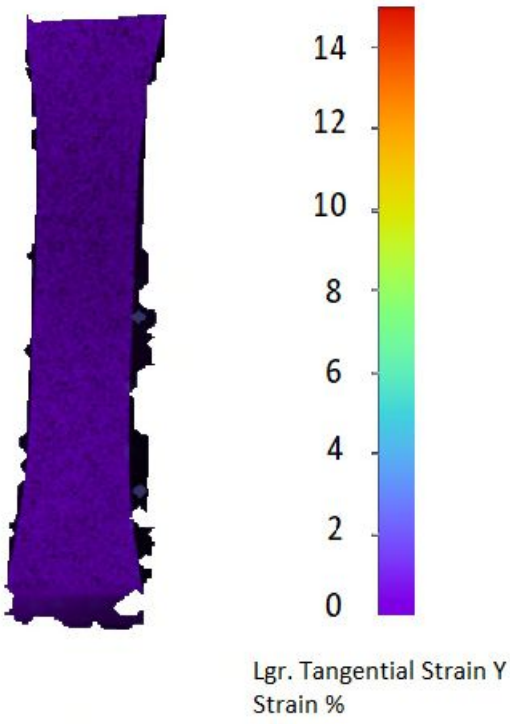

Figure 19 – Axial strain map of 10% pre-strained specimen at 500MPa

Upon characterisation of the mechanical properties of material, for each of the pre-straining levels examined in this study, two large-scale dog bone specimens were prepared and pre-tensioned (see Figure 15) to extract a sufficient number of fracture toughness test specimens. The large-scale dog bone samples for material pre-straining tests had the thickness of 16 mm, width of 90 mm and gauge length of 150 mm. The pre-straining of the large-scale dog bone samples was monitored using the DIC technique to interrupt the tests at 5% and 10% pre-strain levels. On completion of material pre-straining on large-scale dog bone samples, compact tension, C(T), specimens were then fabricated from the as received and pre-strained dog bones as shown in Figure 20. For each pre-strain level, four C(T) specimens were extracted from two pre-strained large-scale dog bone samples (i.e., 2 C(T)s from each large-scale dog bone sample), with the exception of 0% pre-strained material for which three samples were extracted and tested. The C(T) specimens were extracted with the loading axis parallel to the pre-straining direction. The specimen dimensions were chosen based on the guidelines proposed in the ESIS P2-92 standard, however the thickness, B, was reduced to 15 mm to cater for the reduced load capacities during the large-scale dog bone pre-straining as shown in Table 6. From the table it can be seen that all the specimens had a width of W = 50 mm, total thickness of B = 15 mm, and net thickness between the side grooves of approximately B_n = 10.5 mm.

Moreover, the machined notch length introduced into the C(T) specimens, before fatigue pre-cracking, using electrical discharge machining (EDM) technique was approximately a_0 = 23 mm. It is worth noting that all C(T) specimens were initially side-grooved by 30% of the total thickness and then were pre-fatigue cracked to promote a straight fronted crack growth during testing. The initial crack lengths after fatigue pre-cracking, a_i, are summarised in Table 6. As shown in Table 6, 11 samples were tested in total to examine the plastic pre-straining effects on the fracture toughness behaviour of the material. Each specimen has been denoted a unique sample ID which includes the specimen type, followed by the percentage of plastic-pre-strain and ending with the specimen number for each material state. For example, CT-0-1 indicates that the fracture toughness test was performed on the first C(T) specimen with 0% plastic pre-strain (as-received material state).

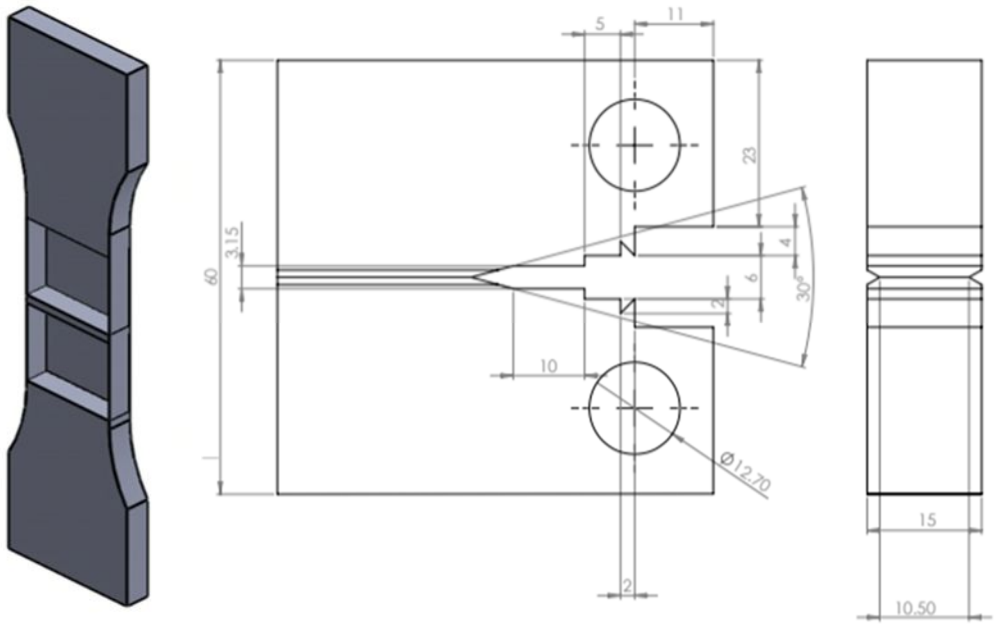

(a) *(b)*

Figure 20 - (a) Schematic illustration of the large-scale dog bone pre-straining samples, (b) engineering drawing of the C(T) specimen notch design for fracture toughness testing (all dimensions are in mm)

Table 6 - Fracture toughness test specimen dimensions

Test ID	W (mm)	B (mm)	B_n (mm)	a_i (mm)
CT-0-1	49.8	15.0	10.3	34.86
CT-0-2	50.0	15.0	10.6	34.51
CT-0-3	50.0	15.0	10.3	34.89
CT-5-1	50.2	15.1	10.3	34.80
CT-5-2	50.0	15.1	10.6	34.86
CT-5-3	50.1	14.9	10.3	34.85
CT-5-4	50.0	15.0	10.5	34.80
CT-10-1	50.1	15.0	10.4	34.88
CT-10-2	50.0	15.0	10.4	34.74
CT-10-3	50.9	15.1	10.4	34.62
CT-10-4	50.0	15.0	10.6	34.84

4.3 Fracture Toughness Testing and Analysis

Fracture toughness tests can be conducted on C(T) specimens using the multiple specimens and single specimen approaches. The multiple specimens approach requires a number of nominally identical specimens to be loaded and unloaded after a specified amount of crack extension had occurred [32]. The single specimen approach involves multiple loading and unloading cycles on only one test specimen, where the crack

extension would be estimated between each loading/unloading cycle using the unloading compliance data. There are a few standard test methods available for fracture toughness testing, however, the standards that are most commonly used to execute and analyse fracture toughness tests on metals are ASTM E1820 and ESIS P2-92 [33,34]. For this work the test method that has been followed is the procedure outlined in ESIS P2-92 [34] which enables direct comparison with the results available in the literature.

4.3.1 Testing Methodology

Fracture toughness tests were performed on three as received (CT-0-1, CT-0-2, CT-0-3), four 5% pre strained (CT-5-1, CT-5-2, CT-5-3, CT-5-4) and four 10% pre-strained (CT-10-1, CT-10-2, CT-10-3, CT-10-4) specimens. Although it is recommended by standard test methods to side groove the specimens after pre-cracking, for this work the specimens were side grooved prior to pre-cracking to ensure that the starter crack introduced into the specimen through fatigue pre-cracking is perfectly straight. Although the standards recommend side grooving specimens by up to 25%, it was noted in preliminary tests for 0% pre-strained S355 material that 25% side grooving on specimens with the maximum allowable crack size for fracture toughness testing (normalised crack length of $a/W \leq 0.7$) was not sufficient to successfully complete the tests (see Appendix C). Therefore, the specimens were side grooved by 30% of the total thickness for this work to facilitate fracture testing. It was ensured that the initial crack lengths at the beginning of fracture toughness tests and after fatigue pre-cracking, a_i, were less than 0.7 of the specimens' width, therefore, all fracture toughness tests had a valid initial crack length at the beginning of the tests as recommended by standards. All specimens were pre-fatigue cracked in air at a frequency of 2 Hz and load ratio of $R = 0.1$ to around 10 mm or more from the machined notch with the crack size being calculated by the unloading compliance technique using a clip gauge attached to the samples during the fatigue pre-cracking process. Pre-cracking allows a sharp crack tip to be introduced into the specimens without allowing a significant plastic zone size to be developed ahead of the starter crack tip. The applied load levels during the fatigue pre-cracking process were continuously decreased as recommended by standards with the cyclic force maintained below the maximum allowable load limit given by [33,34]:

$$P_m = \frac{0.4Bb_0^2\sigma_y}{2W + a_0}$$

Equation 34 – Maximum allowable load limit for fatigue pre-cracking

where b_0 is the uncracked ligament defined as the difference between the specimen width and the initial crack length (W-a_0).

A hydraulic Instron machine with a load cell capacity of 100 kN was used for both the fatigue pre-cracking and fracture toughness testing. The initial crack lengths after fatigue pre-cracking, a_i, together with the final crack length at the end of each fracture toughness test, a_f, are presented in Section 2 and Section 4, respectively. Fracture toughness tests were performed by loading and partial unloading (by 30% of each peak load) at specified intervals, on single specimens. The load line displacement (LLD) was measured using a clip gauge attached to the knife edges which were machined at the crack mouth of the C(T) specimens along the centre of the pin holes. The tests were performed in displacement (i.e., position) control mode with a hold time of 30 seconds at each peak load with the loading and unloading speed of 1 mm/min. From these tests a *P vs LLD* plot was obtained which were then used to generate resistance curves.

4.3.2 Fracture Toughness Data Analysis

For ductile materials, the resistance curves (also known as the R-curves) are built up by plotting the elastic-plastic fracture mechanics parameter J, against the crack extension Δa. According to the ESIS P2-92 standard test method, the J parameter for fracture toughness testing can be calculated by:

$$J_{plastic} = \frac{U}{B_n(W - a_0)}\eta$$

Equation 35 – Calculation of J plastic

where U is the area under the *P vs. LLD* curve and η is a geometry dependent constant which can be defined as η = 2+ 0.522 (1-a_0/W) for C(T) specimen geometry. The instantaneous crack length in fracture toughness tests can be estimated from the unloading compliance, C, using:

$$\frac{a}{W} = 1.000196 - 4.06319\mu + 11.242\mu^2 - 106.043\mu^3 + 464.335\mu^4 - 650.677\mu^5$$

Equation 13 – Calculation of a via unloading compliance

Where:

$$\mu = \frac{1}{[B_{eff} E_M C]^{1/2} + 1}$$

Equation 14 – Calculation of μ

$$B_{eff} = B - (B - B_n)^2 / B$$

Equation 15 – Calculation of Beff

In Equation 14, E_M is described as the effective Young's Modulus which can be determined from:

$$E_M = \frac{1}{C_0 B_{eff}} \left(\frac{W + a_0}{W - a_0}\right)^2 [2.163 + 12.219 + \left(\frac{a_0}{W}\right) - 20.065 \left(\frac{a_0}{W}\right)^2 - 0.9925 \left(\frac{a_0}{W}\right)^3 + 20.609 \left(\frac{a_0}{W}\right)^4 - 9.9314 \left(\frac{a_0}{W}\right)^5$$

Equation 16 – Calculation of Effective Young's Modulus

where C_0 is the average compliance determined from the unloadings performed in the elastic regime.

To identify the data points which would be valid for fracture toughness analysis, crack growth limits must be applied. This is achieved by specifying the blunting line slope and constructing parallel exclusion lines at the appropriate offsets as outlined by the standards. ESIS P2-92 provides guidance on characterising the construction lines, in both their slopes and their placements. The equation given by the ESIS P2-92 standard is:

$$J = 3.75 \sigma_{uts} \Delta a$$

Equation 36 – Construction line equation from ESIS P2-92

The construction of an exclusion line helps to define the limit between which the R curve data points are valid, and which should be removed. ESIS P2-92 suggests plotting the exclusion lines intersecting the abscissa at 0.1 mm and Δa_{max} which can be calculated using:

$$\Delta a_{max} = 0.1(W - a_0)$$

Equation 37 – Calculation of Δa_{max}

A line of best fit is plotted through the valid data points falling between the exclusion lines; the intersection with the parallel line at the offset of 0.2 mm indicates the initiation toughness of the material, which is often referred to as J_{IC}.

4.4 Fracture Toughness Test Results and Discussion

4.4.1 P vs. LLD Curves

Fracture toughness tests were performed on as received (i.e. 0%) and 5% and 10% pre-strained material states at room temperature and the load, *P*, *vs.* load line displacement, *LLD*, curves are shown in Figure 21, Figure 22 and Figure 23, respectively. The presented curves include the loading and partial unloading data (i.e., by approximately 30% of the individual peak loads) which are used to calculate the unloading compliance and subsequently the instantaneous crack length. The dip in the "*P vs. LLD*" curves midway through testing was due to clip gauge limitation, as the travel range was limited and the test had to be interrupted once the LLD reached 4 mm, and the clip gauge reset to continue the curves. For the as-received material state in Figure 21, each specimen shows a similar trend and trajectory with regards to peak loads, however, CT-0-1 showed a lower peak load compared to CT-0-2 and CT-0-3. For all three as-received specimens, the peak load starts to drop at the end of the tests. This indicates that despite the relatively large crack mouth opening displacement in the as-received C(T) specimens, which is around 7 mm, the maximum peak load in *P vs. LLD* response doesn't appear only until the end of the test where the *LLD* is around 6 mm. This is thought to be due to the high ductility of the as-received S355 material, which makes the maximum load level, P_{max}, to appear at relatively large *LLD* values.

For 5% specimens' results shown in Figure 22, all specimens apart from CT-5-3 have exhibited an almost identical trend, except CT-5-3 which shows a lower trend compared to the rest. From around 4 mm, all 5% pre-strained specimens show a decrease in peak load towards the end of the tests which indicates that sufficient loadings and unloading were performed beyond P_{max}. In the 10% test batch results shown in Figure 23 there was more variation in peak load, with specimens CT-10-1 and CT-10-3 showing higher trends. This may be due to the fact that the pre-straining to 10% pre-strain may not have been so uniform in the large-scale dog bone specimens from which the C(T) specimens were extracted. For 10% pre-strain specimens, all specimens show a decrease in peak load from

an *LLD* of around 3.5 mm. Overall, the test results show good repeatability and replication.

In order to directly compare the loading behaviour of the materials with different pre-strain levels, the *P vs. LLD* data from one specimen per material state (the upper bound trend) are plotted in Figure 24. This figure shows that the linear slope in the elastic region for all specimens within different pre-strain levels remains the same, which indicates that the elastic properties are almost identical in the as received and pre-strained materials. It can be seen in this figure that for higher pre-strain levels, a lower load line displacement is required to reach a specific load level. Also seen in Figure 24 is that as the pre-strain level increases, a higher P_{max} value is observed in the *P vs. LLD* response of the material. For example, for the 10% pre-strained material the observed P_{max} value is around 10% higher than the indicative P_{max} value of the as-received material which is observed towards the end of the test on 0% material state. This is due to the material hardening effects with pre-strain which results in higher yield stress, hence greater P_{max}. Finally, seen in Figure 24, is that the experimentally observed *LLD* to reach the P_{max} value in 0%, 5% and 10% pre-strain levels are approximately 6 mm, 4 mm, and 3.5 mm, respectively. This means that by increasing the pre-strain level the extent of ductility reduces in the material and subsequently the P_{max} appears at a lower *LLD* value.

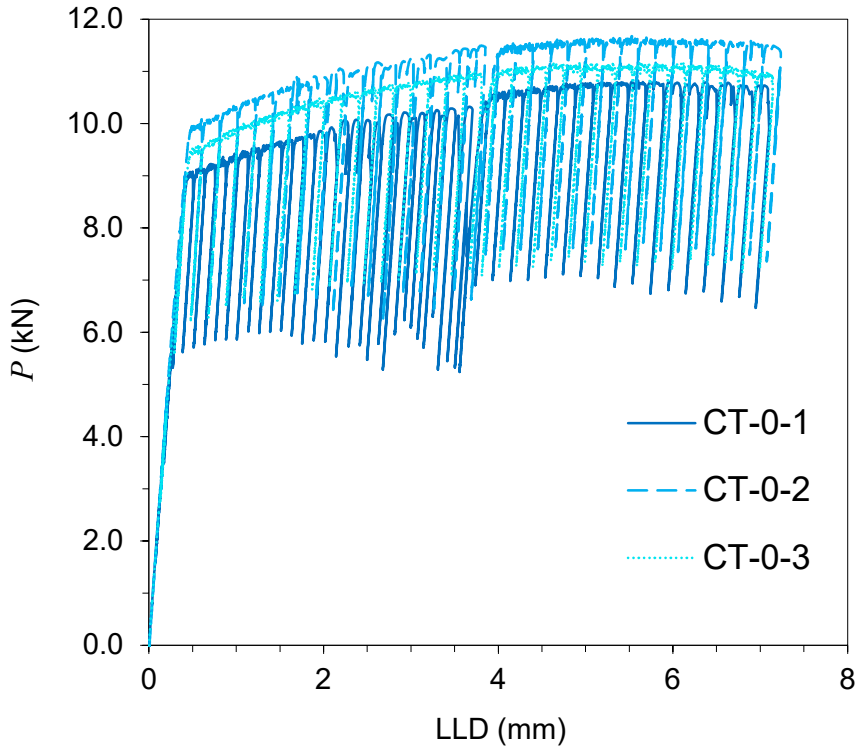

Figure 21 - Comparison of P vs. LLD curves for the as-received specimens

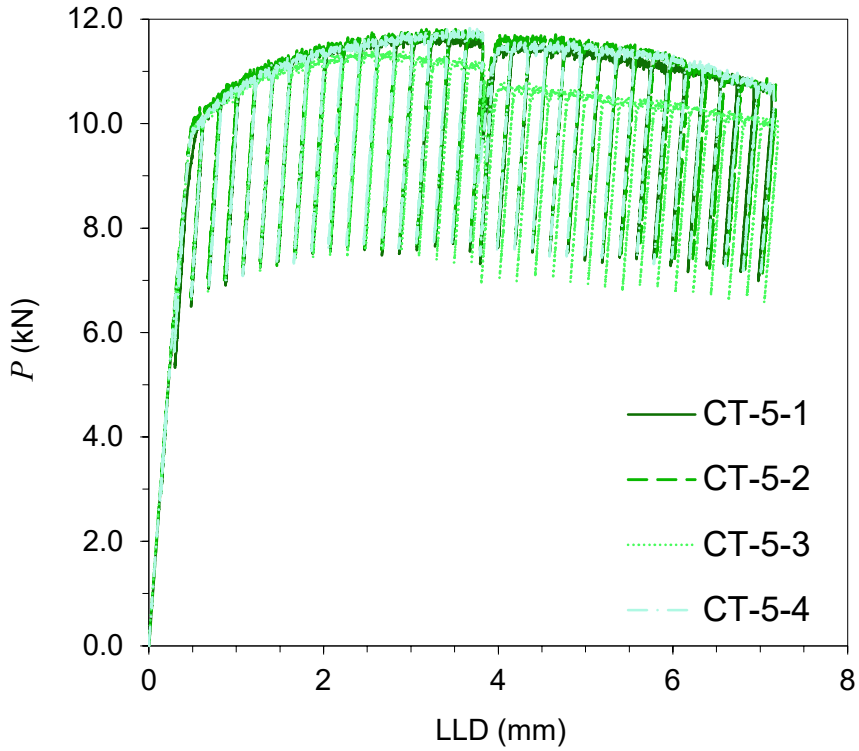

Figure 22 - Comparison of P vs. LLD curves for 5% pre-strained specimens

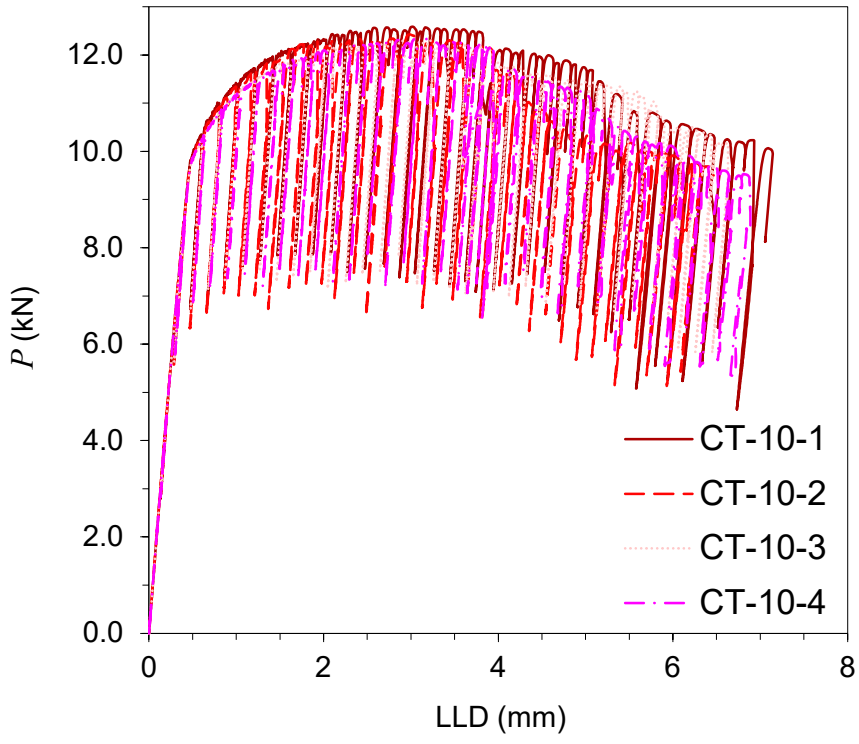

Figure 23 - Comparison of P vs. LLD curves for 10% pre-strained specimens

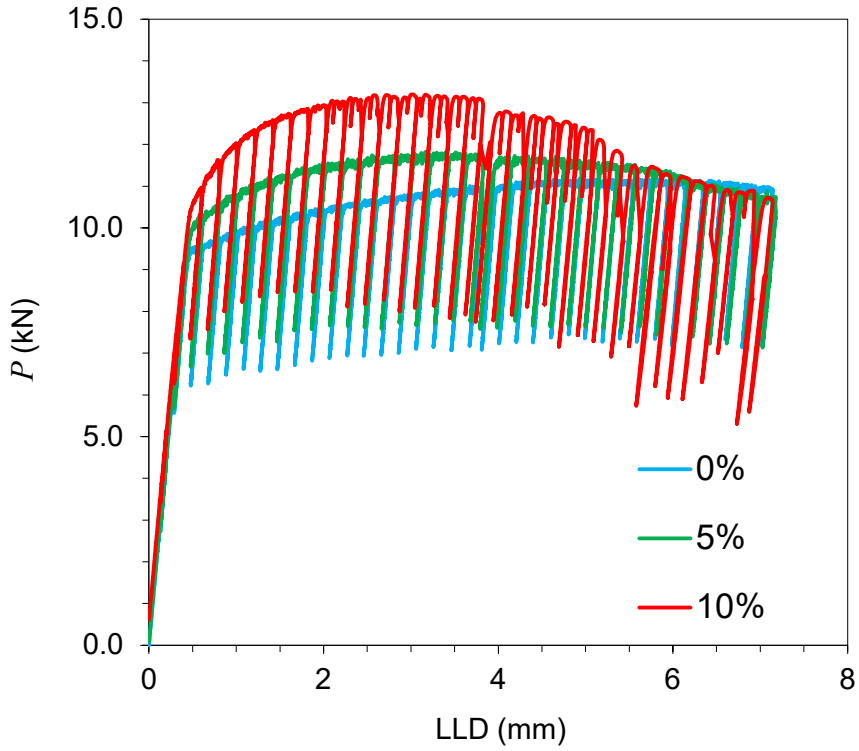

Figure 24 - Comparison of the upper bound P vs. LLD curves for different pre-strain levels

4.4.2 Resistance Curves

The *P vs. LLD* data were analysed, using the guidelines detailed in section 6.3, to generate the R-curves for 0%, 5% and 10% pre-strained specimens in Figure 25, Figure 26 and Figure 27, respectively. For 0% material state in Figure 25, the R-curves show a very similar trend with all specimens following a similar slope with some slight variation in values. Also seen in Figure 25 is that CT-0-1 has exhibited the lowest trend among the as-received material R-curves which is consistent with the *P vs. LLD* trends shown in Figure 21. The R-curves for the 5% pre-strained specimens observed in Figure 26 show good agreement and replicability, with CT-5-1 and CT-5-2 data sets falling upon each other. The lowest R-curve among 5% pre-strained specimens is observed in the test on CT-5-3 which is consistent with the low *P vs. LLD* curve observed for this specimen in Figure 22. The results for 10% pre-strained specimens in Figure 27 show relatively more experimental scatter, however all results exhibited very similar trends with a clear correlation between J and Δa parameters.

For direct comparison between the R-curves obtained from material with different pre-strain levels, one data set per material state is plotted and compared with other material states in Figure 28. The lowest curve for each set has been plotted. It can be clearly

observed in this figure that an increase in the pre-strain level results in a higher R-curve and therefore the fracture toughness behaviour of S355 material is strongly dependent on the material pre-straining. As seen in Figure 28, for a given value of Δa the corresponding J value is found to be the highest in 0% as-received material and the lowest in 10% pre-strained material, with the 5% pre-trained material falling in between the two. The results in Figure 28 show that while for the low values of Δa the resistance curve data points for different material states fall close to each other, it is evident that the difference between J values for pre-strained materials compared to the as-received material state increases by increasing the crack extension. This implies that while plastic pre-straining increases the P_{max} and P *vs.* LLD trend (see Figure 24), it has a considerable detrimental effect on the fracture behaviour of the material as shown in Figure 28. In summary, these observations show that material pre-straining results in a reduction in fracture toughness for S355.

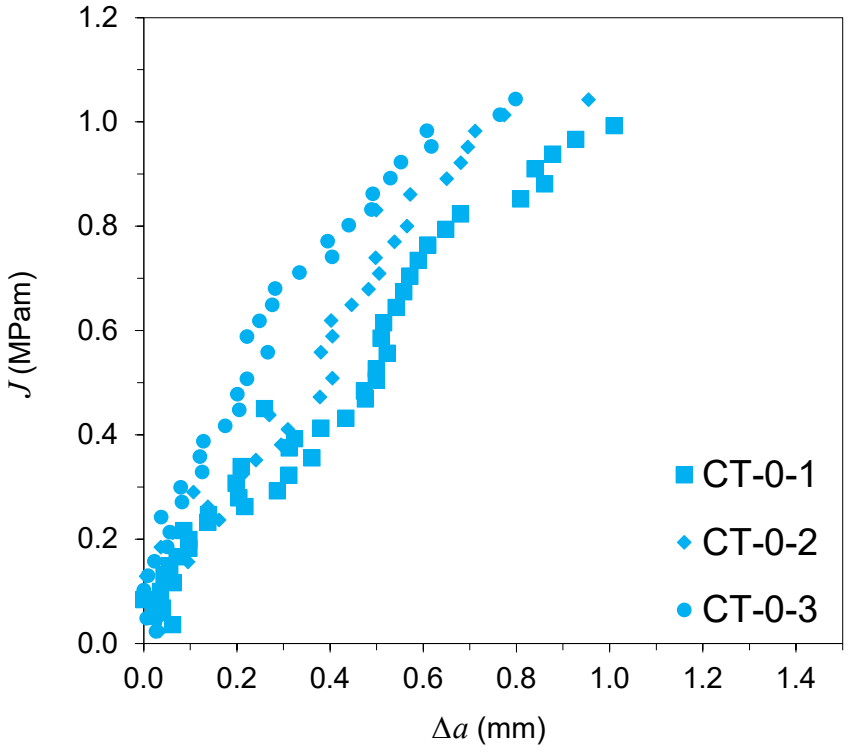

Figure 25 - R-curves for the as received specimens

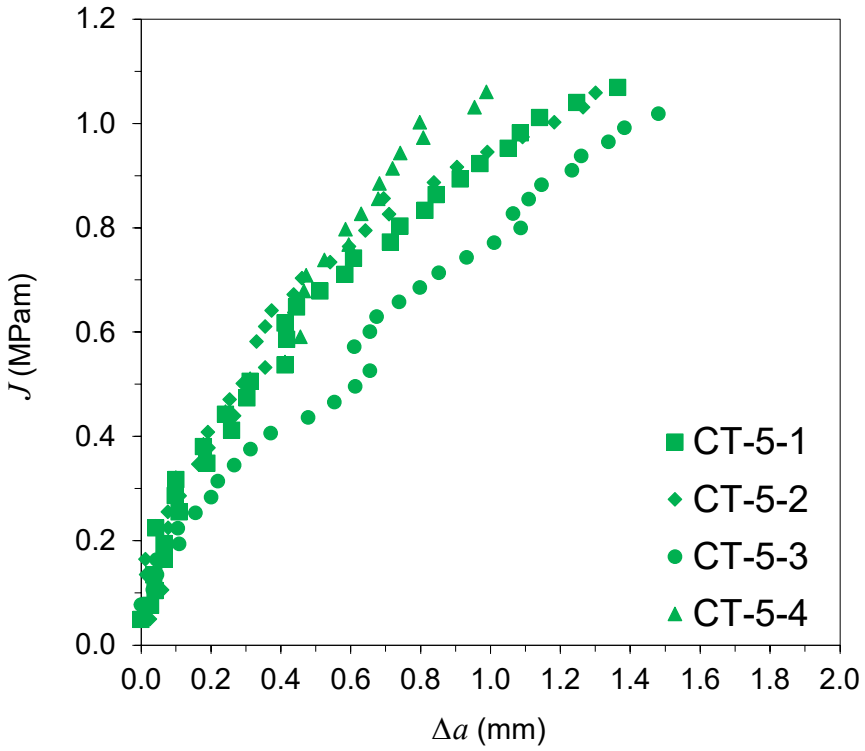

Figure 26 - R-curves for 5% pre-strained specimens

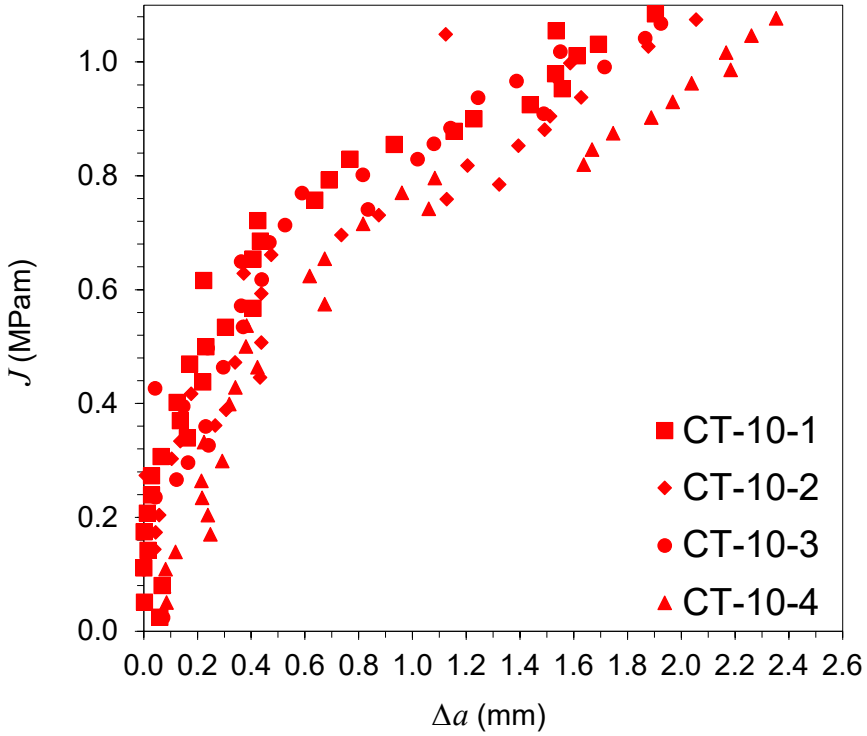

Figure 27 - R-curves for 10% pre-strained specimens

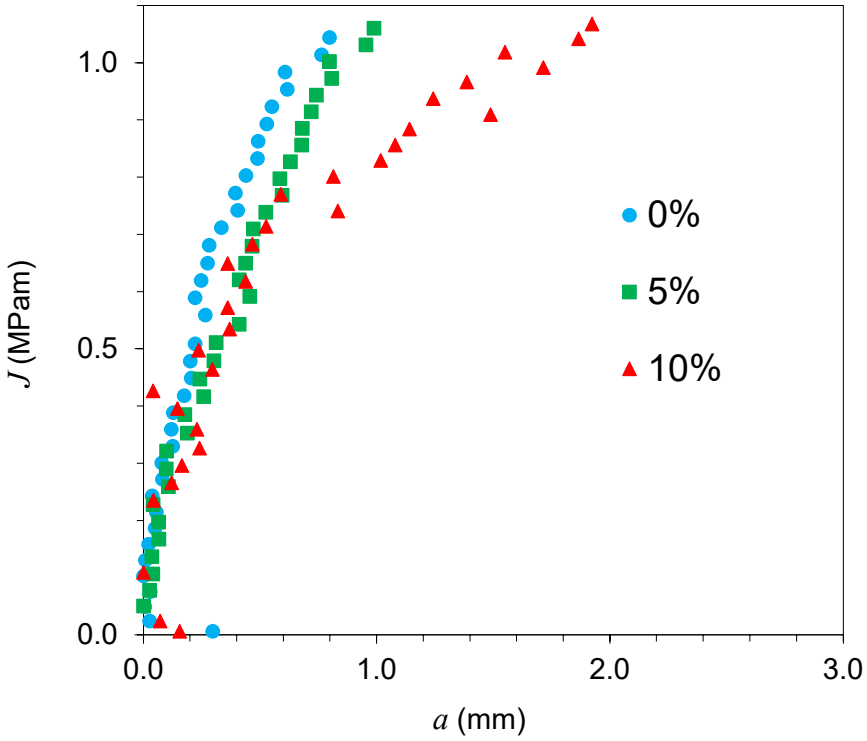

Figure 28 - Comparison of R-curves for different pre-strain levels

4.5 Fracture Toughness Results

The R-curves presented in Figure 25-Figure 27 were further analysed, following the procedure described in section 6.3, to quantify the fracture initiation toughness values for all the specimens tested in this study. An example of the data analysis process on the R-curves, which includes the construction of a blunting line and exclusions lines, is presented for CT-10-4 specimen in Figure 29. The equations of the line of best fits to the valid data points for each of the specimens examined in this study are collectively presented in Table 7. Also included in this table are the Δa_{max} and J_{IC} values for specimens with different pre-strain level. As seen in Table 7, the fracture initiation toughness values for 0%, 5% and 10% pre-strained materials are found to range within 0.76−1.02, 0.44−0.86 and 0.65−0.78, respectively. The test results show that the average J_{IC} values for the as received, 5 and 10% pre-strained material states are 0.86 MPam, 0.79 MPam and 0.71 MPam, respectively. This indicates that an increase in the plastic pre-strain level in S355 material leads to a reduction in the fracture initiation toughness value. It can be noted that the energy required to initiate the crack is higher in 0% pre-strain specimens compared to 5% and 10% pre-strained specimens. This is because the as-received material has a higher ductility and lower yield stress, therefore a higher level of energy is requited for fracture crack initiation. The results show that on average, tensile pre-straining to 10% reduces that J_{IC} fracture toughness value by around 15% to that of observed in the as-received material, therefore this effect should be quantified and accounted for in life assessment of offshore wind monopiles.

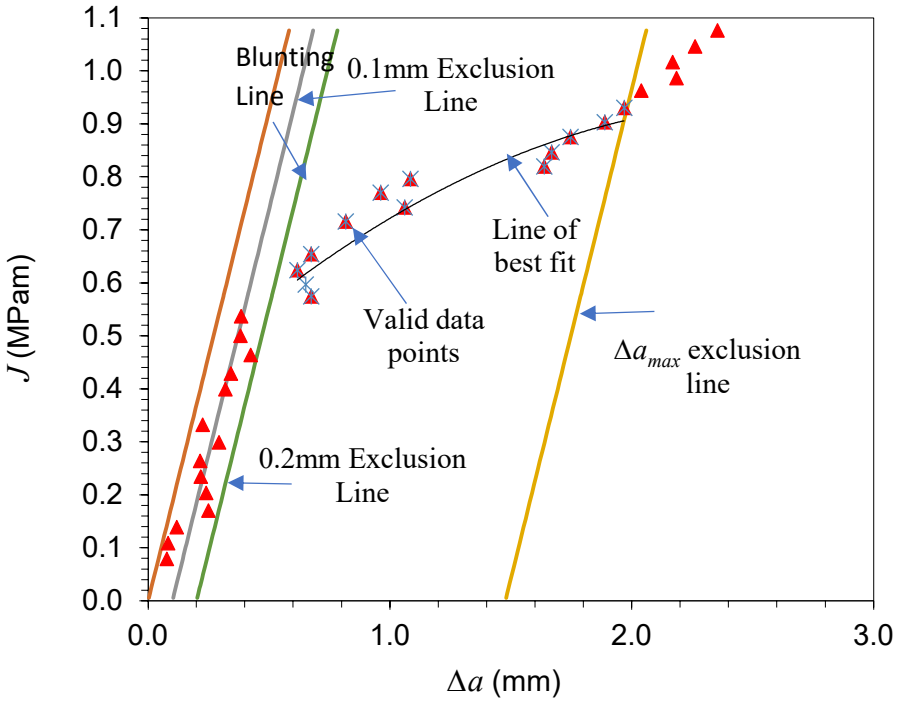

Figure 29 - An example of the fracture toughness analysis using the R-curve generated for CT-10-4 specimen

Table 7 - J_{IC} test results for all specimens with different pre-strain levels

Test ID	Δa_{max} (mm)	J_{IC} (MPam)	Line of best fit equation
CT-0-1	2.70	0.76	$y = -1.5401\Delta a^2 + 3.0792\Delta a - 0.5776$
CT-0-2	1.57	0.80	$y = -1.2886\Delta a^2 + 2.4908\Delta a - 0.1567$
CT-0-3	1.51	1.02	$y = -0.7322\Delta a^2 + 1.4187\Delta a + 0.3695$
CT-5-1	1.50	0.72	$y = -0.1959\Delta a^2 + 0.8514\Delta a + 0.2808$
CT-5-2	1.57	0.80	$y = -0.0718\Delta a^2 + 0.5016\Delta a + 0.517$
CT-5-3	1.51	0.44	$y = -0.0466\Delta a^2 + 0.6807\Delta a + 0.1335$
CT-5-4	1.54	0.86	$y = -1.925\Delta a^2 + 3.7828\Delta a - 0.8102$
CT-10-1	1.47	0.78	$y = 0.0583\Delta a^2 + 0.1005\Delta a + 0.6939$
CT-10-2	1.55	0.69	$y = -0.0299\Delta a^2 + 0.3554\Delta a + 0.4608$
CT-10-3	1.46	0.74	$y = -0.0163\Delta a^2 + 0.2955\Delta a + 0.5651$
CT-10-4	1.48	0.65	$y = -0.0836\Delta a^2 + 0.4386\Delta a + 0.3665$

Furthermore, the fracture toughness results were re-evaluated by calculating the J_{IC} values using an offset line of 0.5mm to account for scatter in fracture toughness values. A table summarising the averages of the findings are seen in Table 8. From the table, it can be seen that even after accounting for scatter, the correlation of a reduction in fracture toughness with increasing pre-straining still holds true.

Table 8 – Average fracture toughness values using 0.5mm offset line

Pre-strain (%)	J_{IC} (MPam)
0	1.01
5	0.95
10	0.81

4.6 Fractography

Upon completion of the fracture toughness tests, the specimens were soaked in liquid nitrogen for 5 minutes and then broken open under monotonic loading conditions. Fractography analysis was conducted by taking high resolution macroscopic pictures of the fracture surfaces of all specimens after testing to measure the actual crack lengths prior and after fracture toughness testing. Crack lengths were measured using ImageJ software, and the crack extensions reported are an average of values across the fracture surface. An example of the fracture surfaces for 0% can be seen in Figure 30. From the fracture surface, three zones can be identified: the zone of fatigue pre-cracking, fracture toughness crack growth and fast fracture during specimen break open (see Figure 30). From the fracture surface, there is uniformity in the pre-cracking region, and this suggests good alignment in the test set up. Table 9 shows the crack length estimations taken from the unloading compliance for the final crack length, at the end of the fracture toughness tests, compared to the measured final crack lengths on the fracture surface. The percentage error between each has also been calculated. The results shown that there is a good agreement between the measurements taken from the unloading compliance compared to the actual measurements taken in the fractography analysis. This is determined by the percentage error between the two, which is in general less than 7%. Due to the fact that the percentages of error for a_f values are very small, it can be concluded that there is relatively good agreement overall between the unloading compliance and the actual measurements. Therefore, it can be concluded with confidence that the R-curves and quantified J_{IC} values are reliable.

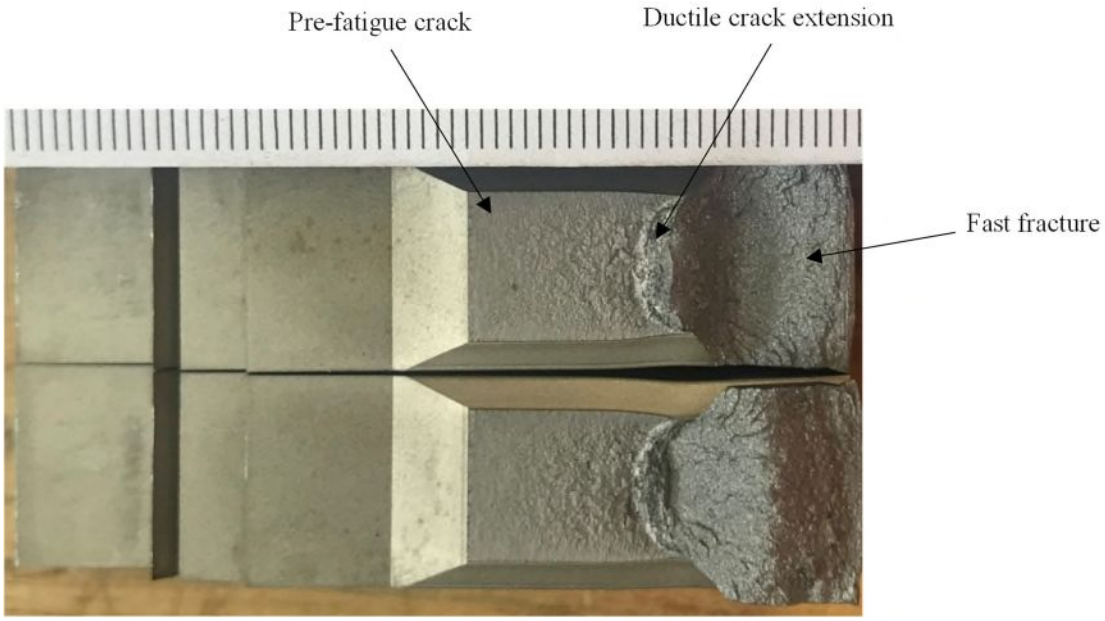

Figure 30 - Fracture surface of an as-received specimen (the division lines in the scale bar are spaced with 1 mm distance)

Table 9 - Comparison of crack length estimates and measurements

Specimen ID	a_i – from the unloading compliance (mm)	a_i – from the fracture surface (mm)	% error in estimation of a_i	a_f – from the unloading compliance (mm)	a_f – from the fracture surface (mm)	% error in estimation of a_f
CT-0-1	12.17	12.39	1.74	36.22	37.11	2.40
CT-0-2	12.54	11.87	5.61	35.29	36.81	4.13
CT-0-3	12.15	12.16	0.07	35.81	37.10	3.48
CT-5-1	12.31	12.53	1.81	36.59	38.29	4.44
CT-5-2	12.42	11.77	5.48	35.65	37.42	4.73
CT-5-3	12.18	12.24	0.52	36.54	37.91	3.61
CT-5-4	12.21	11.84	2.14	35.62	36.31	1.90
CT-10-1	12.18	12.59	3.27	37.33	38.64	3.39
CT-10-2	12.43	11.96	3.87	36.90	39.32	6.15
CT-10-3	12.16	12.59	3.46	37.36	38.49	2.94
CT-10-4	12.11	12.36	2.02	36.60	38.39	4.66

4.7 Pre-straining Effects on Structural Integrity Assessments

In the offshore wind industry, the location of cracks may occur at the weld toes between plates, or around cable holes for electrical cabling of monopiles. It is to be understood that during the induced material pre-straining during the manufacturing process, the strain distribution through the thickness of the plates are not uniform, and instead a progression from tensile strains on the outer surface to compressive strains on the inner surface would exist [22]. Comparison of the obtained results from the present study with those available on the literature show that material pre-straining affects the fracture and mechanical properties regardless of whether the pre-strains are tensile or compressive, as both pre-straining directions have been found to increase the yield stress and reduce the fracture toughness of the material [29].

The results obtained from the present study highlight the importance of pre-straining effects in structural integrity assessment of offshore wind monopiles. In order to find a correlation between the fracture toughness and the tensile pre-strain level, the data obtained from the tests performed in the current study are further analysed in Figure 31. This figure graphically presents the correlation between J_{IC} values and yield strength with the plastic pre-strain level, ε_p. It can be seen in this figure that as the pre-strain level increases, the yield strength increases due to strain hardening mechanisms. Therefore, the material decreases in ductility and thus a decrease in J_{IC} values appears in the material's behaviour. So, it can be seen that within the range of tensile pre-strains considered in this study there is a direct correlation between the average fracture toughness value and the level of pre-tensioning specifically for steel grade S355G10+M which can be empirically described as:

$$J_{IC} = -0.0145\varepsilon_p + 0.8618$$

Equation 38 – Empirical equation correlating J_{IC} with plastic strain for S355G10+M

The proposed empirical relationship could enable monopile fabricators and designers in the offshore wind industry using this specific steel grade (S355G10+M) to gain a more accurate design life and realistic structural integrity analysis by considering the plastic strain levels introduced into the monopiles during the fabrication process. These obtained fracture toughness values and proposed empirical relationship can be used in future work to perform further analysis using failure assessment diagrams to estimate the critical crack

length beyond which failure would occur in monopiles, and thus enable appropriate inspection and maintenance schedules to avoid catastrophic failures in the offshore wind turbine foundations. However, this relationship needs to be tested across a larger database of experimental results than what is presented in this paper. These results will be used in the future to develop and validate a finite element model to predict the pre-straining effects on fracture behaviour of structural steels to achieve a more accurate remaining life estimation of offshore structures. It must also be pointed out that C(T) specimens, especially those with side grooves, experience a high degree of crack tip constraint (the dependence of fracture toughness value on the geometry of a test specimen) and were selected for these experiments as higher thicknesses of monopile structures typically possess higher levels of constraint. Therefore, the fracture toughness results presented in this paper are a conservative assessment of the structural integrity of a monopile structure. Further work needs to be undertaken to investigate the transferability of the constraint parameter from C(T) testing specimens to monopile structures. The trend in reduction of J_{IC} as a result of plastic pre-straining can be used in structural integrity assessment of cable holes present in offshore wind turbine monopile structures, as the results from this study can be used in failure assessment diagrams for defect assessment. As fracture toughness values are inputted into failure assessment diagram criteria, a change in fracture toughness would make a significant impact on the defect assessment of an offshore wind monopile structure.

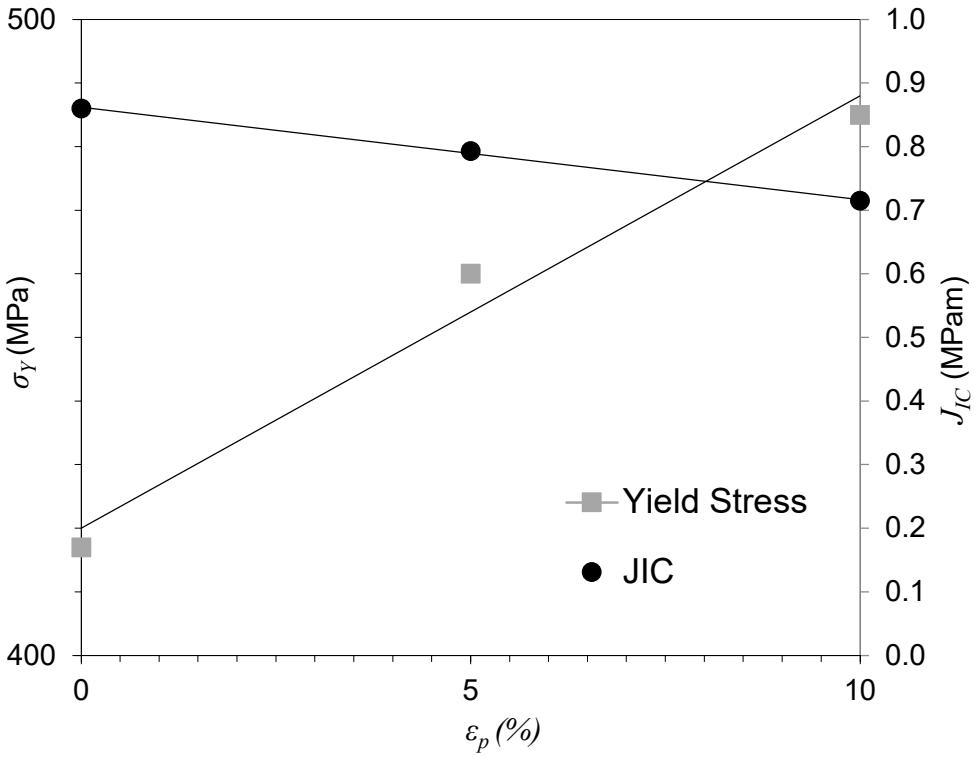

Figure 31 - Effects of pre-strain level on yield stress and J_{IC} values

4.8 Conclusions

Material pre-strain was introduced into S355 structural steel samples by performing interrupted tensile tests to stress levels corresponding to 5% and 10% plastic strain at room temperature. C(T) specimens were fabricated from the pre-strained material and fracture toughness tests were conducted at room temperature. From fracture surface analysis it was concluded that there was good alignment in the test set up, and that there was good agreement between the estimated crack length from unloading compliance and the actual crack length measurements. *P vs. LLD* plots of each pre-strained material were analysed and from the results it could be seen that the peak load increased with the pre-strain level, with a decrease in load line displacement value. This is due to the decrease in ductility and increase in the yield stress of the material as a result of pre-straining. From the R-curve results it was observed that pre-straining decreases the J_{IC} fracture toughness by up to 15% compared to the as-received material. This is due to the material hardening and thus a reduced ability to absorb energy due to the increase in dislocation density. An empirical formula was determined to correlate the yield stress and fracture toughness values with the pre-strain level for S355G10+M structural steel, which could improve the structural integrity assessment on offshore wind turbine monopile foundations which are

subjected to plastic pre-strains during the fabrication process. However, further investigation needs to be conducted in future work to improve the life assessment of monopiles made of a wider range of S355 structural steel subgrades as this study only investigated one specific subgrade.

4.9 Acknowledgements

This work was supported by grant EP/L016303/1 for Cranfield, Oxford and Strathclyde Universities, Centre for Doctoral Training in Renewable Energy Marine Structures - REMS (http://www.rems-cdt.ac.uk/) from the UK Engineering and Physical Sciences Research Council (EPSRC).

4.10 References

[1] Soares-Ramos EPP, de Oliveira-Assis L, Sarrias-Mena R, Fernández-Ram\'\irez LM. Current status and future trends of offshore wind power in Europe. Energy [Internet]. 2020 Jul;202:117787. Available from: https://doi.org/10.1016%2Fj.energy.2020.117787

[2] Spring MJJ. Global Expansion of Offshore Wind Power Depends on Overcoming Significant Challenges Facing Floating Wind Turbines. In: Offshore Technology Conference [Internet]. Offshore Technology Conference; 2020. Available from: https://doi.org/10.4043%2F30524-ms

[3] Queen T. THE QUEEN ' S SPEECH 2019 Prime Minister ' s Office 10 Downing Street London HER MAJESTY ' S MOST GRACIOUS SPEECH TO BOTH HOUSES OF PARLIAMENT. 2019;(December).

[4] Mehmanparast A, Brennan F, Tavares I. Fatigue crack growth rates for offshore wind monopile weldments in air and seawater: SLIC inter-laboratory test results. Mater Des [Internet]. 2017 Jan;114:494–504. Available from: https://doi.org/10.1016%2Fj.matdes.2016.10.070

[5] Moghaddam BT, Hamedany AM, Taylor J, Mehmanparast A, Brennan F, Davies CM, et al. Structural integrity assessment of floating offshore wind turbine support structures. Ocean Eng [Internet]. 2020 Jul;208:107487. Available from: https://doi.org/10.1016%2Fj.oceaneng.2020.107487

[6] Velarde J, Kramhøft C, Sørensen JD, Zorzi G. Fatigue reliability of large monopiles for offshore wind turbines. Int J Fatigue [Internet]. 2020 May;134:105487. Available from: https://doi.org/10.1016%2Fj.ijfatigue.2020.105487

[7] Esteban MD, Couñago B, López-Gutiérrez JS, Negro V, Vellisco F. Gravity based support structures for offshore wind turbine generators: Review of the installation

process. Ocean Eng [Internet]. 2015 Dec;110:281–91. Available from: https://doi.org/10.1016%2Fj.oceaneng.2015.10.033

[8] Negro V, López-Gutiérrez J-S, Esteban MD, Matutano C. Uncertainties in the design of support structures and foundations for offshore wind turbines. Renew Energy [Internet]. 2014 Mar;63:125–32. Available from: https://doi.org/10.1016%2Fj.renene.2013.08.041

[9] Sergio, Sanchez Lopez-Gutierrez Jose-Santos, Negro Vicente EMD. Foundations in Offshore Wind Farms: Evolution Characteristics and Range of Use. Analysis of Main Dimensional Parameters in Monopile Foundations. Mar Sci Eng. 2019;

[10] Pérez-Collazo C, Greaves D, Iglesias G. A review of combined wave and offshore wind energy. Renew Sustain Energy Rev [Internet]. 2015 Feb;42:141–53. Available from: https://doi.org/10.1016%2Fj.rser.2014.09.032

[11] Lozano-Minguez E, Kolios AJ, Brennan FP. Multi-criteria assessment of offshore wind turbine support structures. Renew Energy [Internet]. 2011 Nov;36(11):2831–7. Available from: https://doi.org/10.1016%2Fj.renene.2011.04.020

[12] Henno S. Hydrodynamic loading on the shaft of a gravity based offshore wind turbine. Delft. 2014.

[13] Kolios A, Collu M, Chahardehi A, Brennan FP, Patel MH. A multi-criteria decision making method to compare support structures for offshore wind turbines. 2010 Dec 1;4778–87.

[14] Orlando L. Review of Design Procedures for Monopile Offshore Wind Structures. 2015.

[15] Igwemezie V, Mehmanparast A. Waveform and frequency effects on corrosion-fatigue crack growth behaviour in modern marine steels. Int J Fatigue [Internet]. 2020 May;134:105484. Available from: https://doi.org/10.1016%2Fj.ijfatigue.2020.105484

[16] Igwemezie V, Mehmanparast A, Kolios A. Materials selection for XL wind turbine support structures: A corrosion-fatigue perspective. Mar Struct [Internet]. 2018 Sep;61:381–97. Available from: https://doi.org/10.1016%2Fj.marstruc.2018.06.008

[17] Igwemezie V, Mehmanparast A, Kolios A. Current trend in offshore wind energy sector and material requirements for fatigue resistance improvement in large wind turbine support structures - A review. Renew Sustain Energy Rev [Internet]. 2019 Mar;101:181–96. Available from: https://doi.org/10.1016%2Fj.rser.2018.11.002

[18] Jacob A, Mehmanparast A, D'Urzo R, Kelleher J. Experimental and numerical investigation of residual stress effects on fatigue crack growth behaviour of S355 steel weldments. Int J Fatigue [Internet]. 2019 Nov;128:105196. Available from: https://doi.org/10.1016%2Fj.ijfatigue.2019.105196

[19] Jacob A, Oliveira J, Mehmanparast A, Hosseinzadeh F, Kelleher J, Berto F. Residual stress measurements in offshore wind monopile weldments using neutron diffraction technique and contour method. Theor Appl Fract Mech [Internet]. 2018 Aug;96:418–27. Available from: https://doi.org/10.1016%2Fj.tafmec.2018.06.001

[20] Mehmanparast A, Taylor J, Brennan F, Tavares I. Experimental investigation of mechanical and fracture properties of offshore wind monopile weldments: {SLIC} interlaboratory test results. Fatigue Fract Eng Mater Struct [Internet]. 2018 May;41(12):2485–501. Available from: https://doi.org/10.1111%2Fffe.12850

[21] Kumar L, Majumdar S, Sahu RK. Measurement of the residual stress in hot rolled strip using strain gauge method. In Author(s); 2017. Available from: https://doi.org/10.1063%2F1.4990193

[22] Anandavijayan S, Mehmanparast A, Brennan F. A numerical analysis of the effects of manufacturing processes on material pre-strain in offshore wind monopiles. Procedia Struct Integr [Internet]. 2018;13:953–8. Available from: https://doi.org/10.1016%2Fj.prostr.2018.12.178

[23] Hagiwara N, Masuda T, Oguchi N. Effects of Prestrain on Fracture Toughness and Fatigue-Crack Growth of Line Pipe Steels. J Press Vessel Technol [Internet]. 2001 Apr;123(3):355–61. Available from: https://doi.org/10.1115%2F1.1379531

[24] Cosham A, Hagiwara N, Fukuda N, Masuda T. A Model to Predict the Effect of Pre-Strain on the Fracture Toughness of Line Pipe Steel. In: 4th International Pipeline Conference, Parts A and B [Internet]. ASMEDC; 2002. Available from: https://doi.org/10.1115%2Fipc2002-27324

[25] Minami F, Arimochi K. Evaluation of Prestraining and Dynamic Loading Effects on the Fracture Toughness of Structural Steels by the Local Approach. J Press Vessel Technol [Internet]. 2001 Apr;123(3):362–72. Available from: https://doi.org/10.1115%2F1.1379532

[26] Sivaprasad S, Tarafder S, Ranganath VR, Ray KK. Effect of prestrain on fracture toughness of {HSLA} steels. Mater Sci Eng A [Internet]. 2000 May;284(1–2):195–201. Available from: https://doi.org/10.1016%2Fs0921-5093%2800%2900739-5

[27] Madi Y, Shinohara Y, Besson J. Effect of prestrain on ductility and toughness in a high-strength line pipe steel. Int J Fract. 2020 Mar 18;224(1):15–29.

[28] Mehmanparast A, Davies CM. The influence of inelastic pre-straining on fracture toughness behaviour of Type 316H stainless steel. Eng Fract Mech [Internet]. 2018 Feb;188:112–25. Available from: https://doi.org/10.1016%2Fj.engfracmech.2017.08.001

[29] Mehmanparast A, Davies CM, Dean DW, Nikbin KM. Plastic pre-compression and creep damage effects on the fracture toughness behaviour of Type 316H stainless steel. Eng Fract Mech [Internet]. 2014 Nov;131:26–37. Available from:

https://doi.org/10.1016%2Fj.engfracmech.2014.10.005

[30] Mehmanparast A, Davies CM, Dean DW, Nikbin K. Effects of plastic pre-straining level on the creep deformation, crack initiation and growth behaviour of 316H stainless steel. Int J Press Vessel Pip [Internet]. 2016 May;141:1–10. Available from: https://doi.org/10.1016%2Fj.ijpvp.2016.03.013

[31] Liaw PK, Landes JD. Influence of prestrain history on fracture toughness properties of steels. Metall Trans A [Internet]. 1986 Mar;17(3):473–89. Available from: https://doi.org/10.1007%2Fbf02643954

[32] Landes JD. Evaluation of the ASTM and ESIS multiple specimen J initiation procedures using the EURO fracture toughness dataset. 2001.

[33] ASTM E1820-06. Standard Test Method for Measurement of Fracture Toughness. Annu B ASTM Stand. 2006;(August):1–65.

[34] ESIS. ESIS P2-92: Procedure for Determining the Fracture Behaviour of Materials. European Structural Integrity Society. 1992. p. 1–92.

[35] Zhu X-K, Joyce JA. Review of fracture toughness (G, K, J, {CTOD}, {CTOA}) testing and standardization. Eng Fract Mech [Internet]. 2012 May;85:1–46. Available from: https://doi.org/10.1016%2Fj.engfracmech.2012.02.001

[36] Amouzouvi KF. A comparative fracture study of a slightly prestrained low alloy steel and a slightly prestrained austenitic stainless steel. Mater Sci Eng [Internet]. 1986 Feb;78(1):65–70. Available from: https://doi.org/10.1016%2F0025-5416%2886%2990080-7

[37] Lee W-S, Lin C-F. Effects of prestrain and strain rate on dynamic deformation characteristics of 304L stainless steel: Part 2{\textemdash}Microstructural study. Mater Sci Technol [Internet]. 2002 Aug;18(8):877–84. Available from: https://doi.org/10.1179%2F026708302225004720

[38] Seth PP, Das A, Bar HN, Sivaprasad S, Basu A, Dutta K. Evolution of Dislocation Density During Tensile Deformation of {BH}220 Steel at Different Pre-strain Conditions. J Mater Eng Perform [Internet]. 2015 May;24(7):2779–83. Available from: https://doi.org/10.1007%2Fs11665-015-1554-6

5. Material Pre-Straining Effects on Fatigue Behaviour of S355 Structural Steel

Satya Anandavijayan[1], Ali Mehmanparast[1], Jarryd Braithwaite[1], Feargal Brennan[2] and Amir Chahardehi[3]

[1] Offshore Renewable Energy Engineering Centre, Cranfield University, Bedfordshire MK43 0AL, UK

[2] Naval Architecture and Marine Engineering, University of Strathclyde, G4 0LZ, UK

[3]Atkins Energy, Nova North, 11 Bressenden Pl, Westminster, London SW1E 5BY

Abstract

A commonly used material in offshore structures is S355 structural steel. For example, during the monopile fabrication process, the material is pre-strained to different levels at different depths through the thickness. Therefore, the influence of pre-straining on fatigue life and crack growth behaviour of the material needs to be examined and considered for design and life assessment procedures. In the present study, uniaxial fatigue and fatigue crack growth tests have been conducted on materials with different pre-strain levels and the results are compared with the un-strained material state. From the test data, it has been seen that the S-N fatigue life will reduce with increasing pre-straining level, while the fatigue crack propagation rate remains largely unchanged in pre-strained material. The results from this study are compared with the recommended S-N fatigue and fatigue crack growth trends available in standards and are discussed in terms of the applicability and level of conservatism in the recommended curves to account for the material pre-straining effects on the fatigue life assessment of offshore structures.

Keywords: fatigue, S355, offshore wind, material pre-straining, S-N curve, monopile

Nomenclature

a	Crack length
a_0	Initial crack length
a_f	Final crack length
B	C(T) specimen thickness
B_n	Net thickness between the side grooves
d	C(T) specimen hole diameter
D	Fatigue damage
E	Elastic Young's modulus
f	Frequency
H	C(T) specimen height
K_{max}	Stress intensity factor at maximum load

K_{min}	Stress intensity factor at minimum load
ΔK	Stress intensity factor range
N	Number of fatigue cycles
N_f	Number of cycles to failure in uniaxial fatigue tests
P_{max}	Maximum Load
P_{min}	Minimum Load
R	Load ratio in fatigue tests (P_{max}/P_{min})
W	C(T) specimen width
Y	Shape function
$\Delta\sigma$	Stress range
σ_{UTS}	Ultimate tensile stress
σ_{max}	Maximum stress
σ_{min}	Minimum stress
σ_y	Yield stress
ε_f	Tensile strain at failure
ε_p	Plastic strain

5.1 Introduction

There is a push for offshore wind which has resulted in the offshore wind industry to develop newer technologies and install more wind farms with turbines of higher capacities in deeper waters [1]. Among different components of offshore wind turbines, foundation structures hold a significant importance in the future development of offshore wind projects due to the significant costs involved in the fabrication and maintenance of these assets [2,3][4][5]. Over the last decade, monopiles foundation structures have been extensively utilised by offshore wind developers due to their simplistic design, production, and unit cost [6,7].

Monopiles are fabricated via the three-roll bending process, a continuous manufacturing process involving cold rolling of previously hot rolled structural steel plates into cylindrical cans, prior to being longitudinally welded. These cans are then welded together circumferentially to achieve the length of monopile required. In order to cold roll structural steel plates into curved shapes, they must be plastically deformed. From

previous works it has been seen that the monopile fabrication process may result in plastic strains ranging from compressive on the inner surface of the steel plates to tensile on the outer surface, and the exact values vary through the thickness [8][9]. Studies have shown that introducing plasticity into metals during fabrication processes can affect the mechanical characteristics of the material [10][11]. Thus, in the case of monopile structures this is an important area that needs to be investigated to ensure accurate lifetimes are predicted using appropriate structural integrity assessment procedures.

Structural steels are widely employed in the fabrication of offshore structures due to their good strength characteristics, as well as good welding properties and ductility. While previous research works have extensively investigated the mechanical and fatigue behaviour of various grades of structural steels [12] [13][14] the material pre-straining effects induced during the fabrication processes have not been examined yet. Work has been previously done to investigate the effect of hardening behaviour on the strength of S355. In the work by de Jesus, et al. [15], monotonic stress-strain curves were obtained on S355 structural steel to evaluate the initial strain hardening behaviour of the parent material. It was observed from these results that S355 had a tensile strength between 470 and 630 MPa, for specimen thicknesses below 16mm, with a yield plateau followed by significant strain hardening [15]. In the work by Forni et al. it was shown that S355 steel retains its strain hardening capacity with increasing strain rate, and at higher strain rates, an instability (such as lower and upper yield strengths) can be present due to the dislocation density, velocity, and loading rate [16].

Another study was conducted on 430 stainless steel to explore the influence of material pre-strain on the fatigue behaviour. The test specimens were initially pre-tensioned to 5%, 8% and 12% strain and subsequently tested under fatigue loading conditions. From this work, it was observed that the tensile pre-straining resulted in a decrease in the number of cycles to failure, at the same stress range [19]. Fatigue behaviour of pre-strained 304L steel was investigated and compared to the as-received materials in [20], and it was noted that pre-strained test specimens had shorter fatigue lives due to their decreased ductility after pre-straining. In a work by Hagiwara et al [18], a comprehensive study was conducted on line pipe steels to compare the fatigue crack growth rates for various grades of steel, in the presence of pre-strains up to 20%. The results from this study showed that

tensile pre-strain had no significant effect on fatigue crack initiation and growth behaviour of the materials tested [18].

While the fatigue design curves such as DNVGL-RP-C203 and life assessment procedures are primarily focussed on engineering materials without any pre-straining history, the results available in the literature suggest that the pre-straining effects on the fatigue life of steels must be carefully investigated and considered in the life assessment of offshore structures. In order to better understand the influence of pre-strains, introduced during fabrication of offshore structures, the present study extensively investigates the fatigue life and crack growth behaviour in the presence of different levels of tensile pre-strains in S355 structural steel, which is widely used in the fabrication of offshore wind turbine foundations, and the results are compared with the as-received material. The results are discussed in terms of the significance of pre-straining effects on design and life assessment of offshore wind turbine monopile foundations and provide new insights to enhance the life prediction of the offshore structures.

5.2 Material Pre-conditioning and Specimen Preparation

The material used in this research is S355GS+10 structural steel due to its wide use in the manufacture of offshore structures. This material is known to have high ductility, allowing it to undergo large deformations [21][22]. In order to investigate the influence of material pre-straining on the fatigue properties of S355, the material was pre-strained to various levels of plastic strain. The three pre-straining conditions which were examined in this study were (1) base metal (BM) which is also known as the as received (AR) material with 0% plastic strain, (2) uniformly pre-tensioned material to 5% plastic strain, and (3) uniformly pre-tensioned material to 10% plastic strain. The mechanical response of the AR material was preliminarily examined by performing an interrupted tensile test on an AR sample and the stress levels corresponding to 5% and 10% plastic strain, ε_p, were identified and applied in uniform pre-tensioning of the AR blocks of S355 in order to introduce the target values of pre-strains in the test specimens.

Subsequent to pre-tensioning of large blocks of S355 steel to 5% and 10% plastic strain, dog-bone shape specimens were extracted for tensile and uniaxial fatigue tests as well as compact tension, C(T), specimens for fatigue crack growth tests. Similarly, dog-bone and C(T) specimens were extracted from an AR block of S355 steel in order to prepare

specimens with 0% plastic strain for testing and comparison with the pre-strained specimens. The dog-bone shape specimens for uniaxial fatigue tests were designed following the guidelines provided in ASTM E466 [23] and had the width of 24 mm, thickness of 11 mm and gauge length of 48 mm. Dogbone specimens were polished prior to testing to reduce the impact of manufacturing effects. The C(T) specimens for fatigue crack growth tests were designed in accordance with ASTM E647[23], and had the total width of W = 50 mm, height of H = 60 mm, thickness of B = 15 mm, pin hole diameter of d = 12.5 mm and initial crack length of a_0 = 22.5 mm. All C(T) specimens were side grooved by 15% of the total thickness on each side and had the net-thickness between the side grooves of B_n = 10.5 mm. The presence of side grooves prior to testing is acceptable, as in the ASTM standards there is no objection against side grooving, thus their presence should not make any significant difference to subsequent test results.

5.3 Testing Methodology

Uniaxial tensile and fatigue tests on dog-bone shape specimens were performed on a servo-hydraulic machine with load carrying capacity of 250kN. To compare the mechanical behaviour of pre-strained materials, two tensile tests per pre-strain levels of 0%, 5% and 10% were performed on dog-bone shape specimens. For the uniaxial fatigue tests, alignment checks were made during the set-up and operation of tests by attaching strain gauges to the opposite sides of the test specimens. All uniaxial fatigue tests were performed under load control mode by implementing the maximum load, $P_{max,}$ and minimum load, P_{min}, in a sinusoidal cyclic waveform. Uniaxial fatigue tests were performed at room temperature in air under a constant frequency of f = 4 Hz with the load ratio of R = 0.1. The uniaxial fatigue samples were continuously cycled, without any interruption throughout the test, until failure. The tests were performed at different values of stress range, $\Delta\sigma$, (described as the difference between maximum applied stress σ_{max} and minimum applied stress σ_{min}) and the number of cycles to failure, N_f, was recorded at the end of each test. In total, six AR, five 5% pre-strained and seven 10% pre-strained dog-bone shape specimens were tested under uniaxial fatigue loading conditions to investigate the influence of material pre-straining on fatigue life of S355 steel. Moreover, additional fatigue tests were performed and interrupted before final failure and were subsequently tested under monotonic loading to investigate the influence of cyclic loading history on the mechanical response of S355 materials with different pre-strain levels.

Fatigue crack growth tests on C(T) specimens were performed on a servo-hydraulic machine with loading capacity of 100kN. The crack growth monitoring in these tests was conducted using the unloading compliance technique by attaching a clip gauge, with the maximum travel range of 4 mm, at the crack mouth of the specimens. For this purpose, knife edges were machined on C(T) specimens to securely accommodate the clip gauge during fatigue crack growth tests. In addition to unloading compliance measurements, high resolution cameras were located behind and in front of the machine to compare the visually observed crack lengths at the free surfaces of C(T) specimens with those estimated from the unloading data. All fatigue crack growth test specimens were at room temperature in air under the frequency of $f = 2$ Hz and load ratio of $R = 0.1$. In total, three AR, four 5% pre-strained and four 10% pre-strained C(T) specimens were tested in this study to investigate the influence of material pre-straining on fatigue crack growth behaviour of S355 steel.

Post testing, specimens were soaked in liquid nitrogen for ten minutes and then broken open under monotonic loading conditions. High resolution macroscopic images of the fracture surfaces were taken and analysed to measure the average fatigue crack growth in each test specimen. The estimated crack lengths from the unloading compliance were compared to the measured values obtained from the fracture surface to check the accuracy of the crack length estimates. As reported in Table 9, the percentage of error in crack length estimations from the unloading compliance data at the end of the fatigue growth tests, a_f, are below 7% confirming that relatively accurate values of crack length were estimated using the clip gauge data.

5.4 Tensile and Fatigue Test Results

5.4.1 Tensile Tests

Tensile tests were conducted on 0%, 5% and 10% pre-strained specimens. Two specimens were tested per pre-straining level; denoted T-0%-1 and T-0%-2, T-5%-1 and T-5%-2, and T-10%-1 and T-10%-2, for 0%, 5% and 10% pre-strain levels, respectively. Digital Imaging Correlation (DIC) technique was employed to accurately determine the strain distributions during tensile tests. An example of the DIC strain maps captured on specimens with 0%, 5% and 10% pre-strains at the given stress level of 480 MPa is shown in Figure 32 . As seen in this figure, before reaching the onset of plasticity the strains

were uniformly distributed across the gauge region of the test specimens. It is worth noting that to plot the tensile curves, the average strain values were taken from an area in the vicinity of the necking and failure region for all the tensile tests performed in this study.

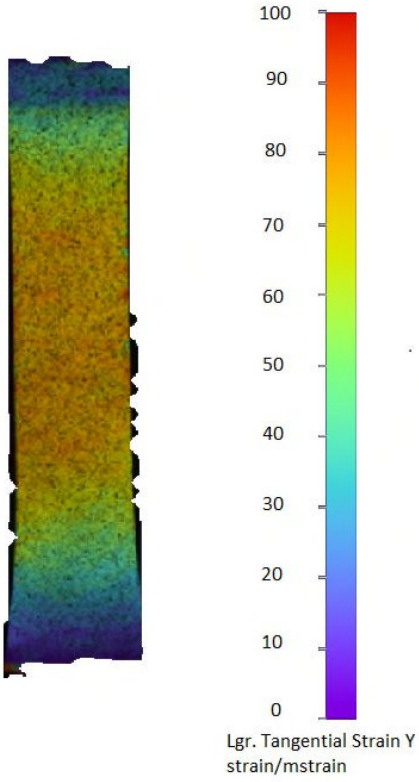

(a)

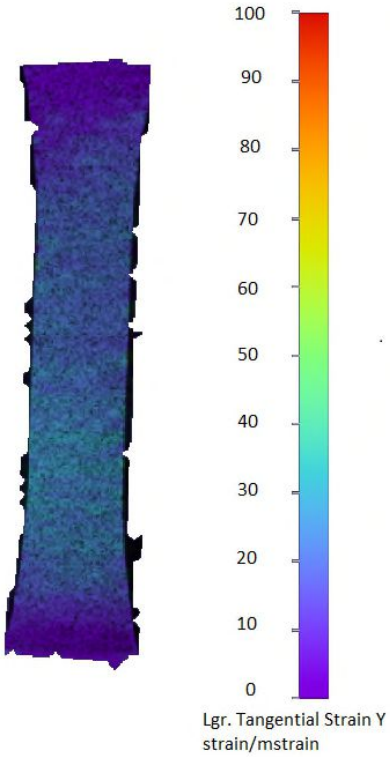

(b)

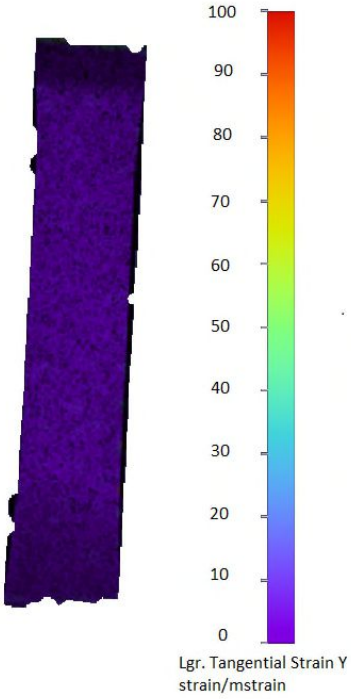

(c)

Figure 32 - DIC strain maps at 480 MPa for (a) 0% , (b) 5%, (c) 10% pre-strained specimens

The average values of elastic Young's modulus, E, yield stress, σ_y, ultimate tensile strength, σ_{UTS}, and strain at failure, ε_f, from the two tests performed on each material pre-strain level are reported in Table 10, and the tensile curves are graphically presented in Figure 33. From the table it can be seen that E, σ_y and σ_{UTS} exhibit an increase by increasing the pre-strain level, while the strain at failure continuously decreases. It is evident from these results that the rate of change in the yield stress of the material, as a result of pre-straining, is greater than that of observed in σ_{UTS}.

Table 10 - Average mechanical properties for 0%, 5% and 10% pre-strained materials

Pre-strain level (%)	***E* (GPa)**	**σ_Y (MPa)**	**σ_{UTS} (MPa)**	***ε_f (%)***
0	222	417	517	50.8
5	255	468	532	49.0
10	264	516	545	46.6

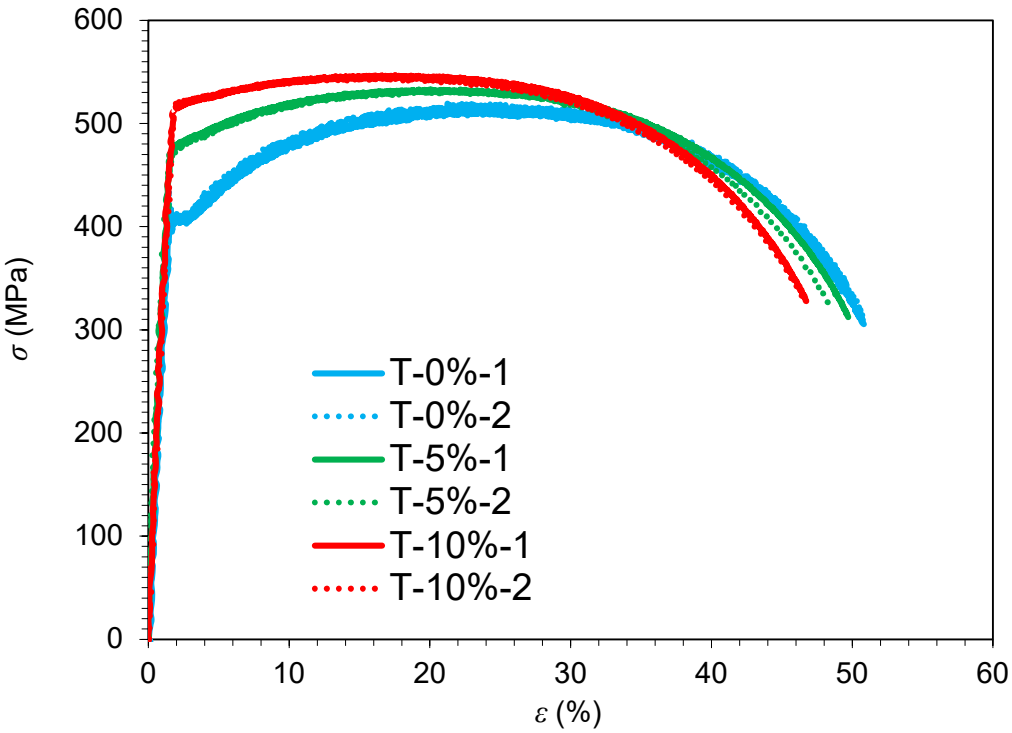

Figure 33 - Comparison of the tensile curves for 0%, 5% and 10% pre-strained materials

5.4.2 Uniaxial Fatigue Tests

Uniaxial fatigue tests were performed on dog-bone specimens with 0%, 5% and 10% pre-strain. Due to the relatively high ductility of S355, initial tests were performed at stress levels of above or close to the yield stress of the AR material and then the stress level was gradually decreased for the following tests via the staircase method. The stress range, $\Delta\sigma$, values applied in uniaxial fatigue tests were 430, 418, 406, 400 and 391 MPa. The number of cycles to failure obtained from uniaxial fatigue tests are correlated with the applied stress range in Log-Log axes and the indicative S-N curves for different pre-strain levels are presented in . It can be seen in this figure that the number of cycles to failure seem to converge at high stress range values. The reducing fatigue life trend, compared to the AR material, can be consistently observed in 5% and 10% pre-strained data points, indicating that an increase in the pre-strain level decreases the fatigue life of the material.

Figure 34 - Uniaxial fatigue specimen undergoing fatigue testing

In order to describe the fatigue life of examined tests specimens, the lines of best fit have been made to each data set to obtain the power-law constants correlating the stress range with the number of cycles to failure, in the form of the Wohler equation which is described as:

$$N_f = A(\Delta\sigma)^B$$ Equation 22 – Wohler's equation

Seen in Table 11 is that while the magnitude of B values for 5% and 10% pre-strain data sets have been found to be lower than the 0% data set, more tests need to be conducted in future work on 5% pre-strained material to quantify a more accurate slope with greater number of data points. Comparing the obtained data on materials with different pre-strain levels presented in and Table 11, an important conclusion derived from this study is that for a given stress range value, severe material pre-straining of up to 10% can reduce the fatigue life by more than an order of magnitude, compared to the AR material with 0% pre-strain level, and this difference in fatigue lives would increase at lower stress levels, however further work needs to be conducted to confirm the fatigue behaviour at lower stresses. These results clearly demonstrate that material pre-straining has a detrimental effect on fatigue life and this effect potentially may be more pronounced at lower stresses and higher pre-strain levels.

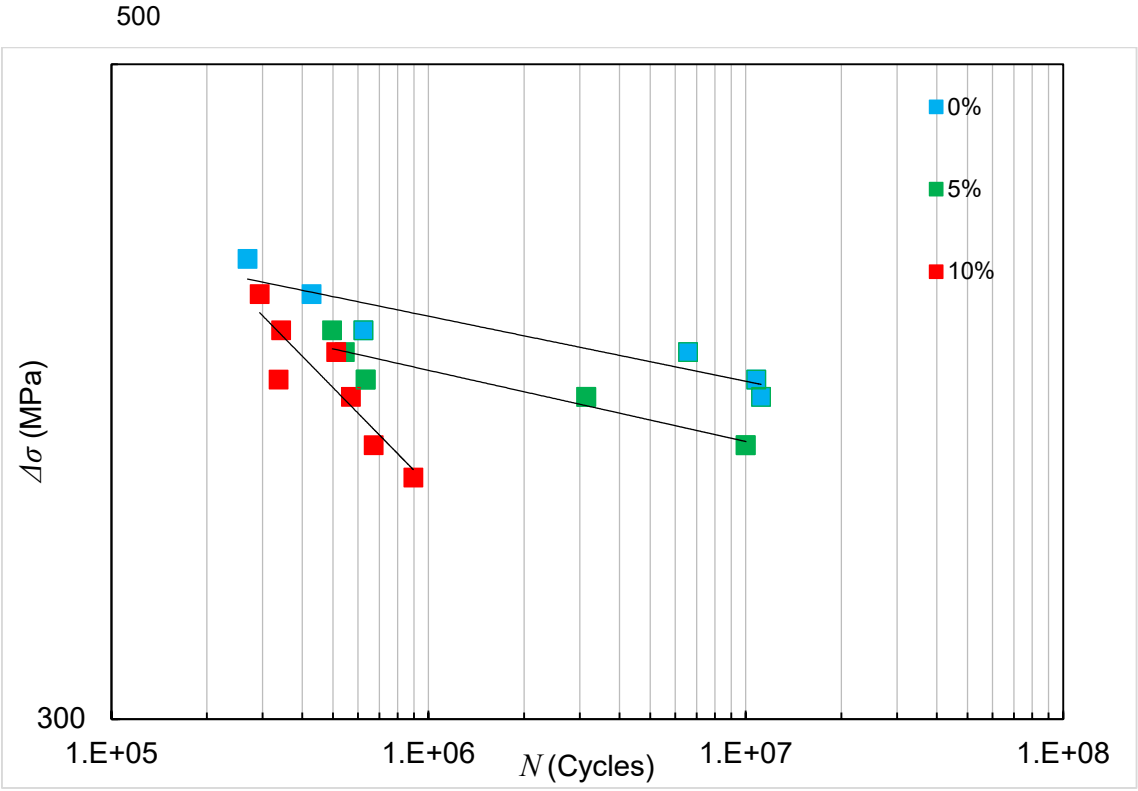

Figure 35 – Line of best fit for uniaxial fatigue data for 0%, 5% and 10% pre-strained materials

Table 11 - Power-law constants from made uniaxial fatigue data

Pre-strain level (%)	N_f	
	logA	***B***
0	110	-39.94
5	100	-36.25
10	24	-7.429

5.4.3 Tensile Tests on Fatigue Damaged Specimens

In order to evaluate the influence of prior fatigue damage on subsequent mechanical behaviour of the material, four interrupted fatigue tests were performed on 0% and 10% pre-strained materials, with two tests performed for each pre-strain level; denoted IF-0%-0.5 and IF-0%-0.8, and IF-10%-0.5 and IF-10%-0.8 for 0% and 10% material pre-strain levels, respectively, where IF stands for interrupted fatigue followed by the percentage of pre-straining whereas the final number identified the level of fatigue damage (i.e. D). Similar to the tests performed in Section 4.2, the interrupted fatigue tests were also performed at the frequency of f = 4 Hz with the load ratio of R = 0.1. For comparison purposes, all four interrupted fatigue tests were performed at a fixed stress range of $\Delta\sigma$ = 406 MPa at which a clear difference in the fatigue life can be observed in 0% and 10% pre-strained material (see). For each of the pre-strain levels, the first test was interrupted at the fatigue damage parameter of D = 0.5 while the second test was stopped at D = 0.8, according to the Miner's rule (see the equation below) and by considering a constant stress amplitude loading condition of $\Delta\sigma$ = 406 MPa (i.e. hence k = 1 in Equation 23). It is worth noting that in order to introduce the pre-defined values of fatigue damage in these tests, the required number of test cycles were calculated based on the total number of cycles for failure, N_f, at $\Delta\sigma$ = 406 MPa for 0% and 10% pre-strain material states (see

).

Tensile tests were performed on interrupted fatigue samples and the results are presented in Figure 36. Also included in this figure are the average tensile curves on 0% (denoted IF-0%-0) and 10% (denoted IF-10%-0) pre-strained materials without any pre-existing fatigue damage (i.e. n = 0 according to Equation 23).

$$D_f = \sum \frac{N_i}{N_{fi}}$$

Equation 23 – Palmgren-Miner rule for damage

The mechanical properties obtained from the tests on 0% and 10% pre-strained materials with different extents of fatigue damage are summarised in Table 12. As seen in Figure 36 and Table 12, for 0% (i.e. AR) material state, a higher yield stress can be observed in interrupted fatigue tests compared to the undamaged material. Knowing that the applied stress level of $\Delta\sigma = 406$ has resulted in the maximum applied stress of $\sigma_{max} = 451$ MPa in these tests, the higher yield stress in the interrupted fatigue tests on AR material state has occurred due to the hardening (behaviour which takes place in the first fatigue cycle under a maximum stress level of greater than yield. On the other hand, knowing that the σ_{max} applied in interrupted fatigue tests on 10% pre-strained material is lower than the yield stress for this material state, there is no noticeable change observed in the yield stress of the fatigue damaged and undamaged pre-strained materials.

Also seen in Figure 36 and Table 12 is that while the increase in σ_{UTS} and decrease in ε_f for the fatigue damaged AR specimens, compared to undamaged AR material, can be associated with material hardening in the first fatigue cycle (because $\sigma_{max} > \sigma_y$), the slight changes in σ_{UTS} and ε_f of 10% pre-strained specimens with different extent of fatigue damage can be considered negligible within the inherent experimental scatter. These results suggest that if uniaxial fatigue damage occurs at an applied maximum stress level of below yield, there will be no noticeable change in the mechanical properties of the material and the accumulation of fatigue damage has insignificant effect on macroscopic plastic properties of the material including strain at failure which has been found to drop by less than 10% after introduction of severe fatigue damage ($D = 0.8$) into the material.

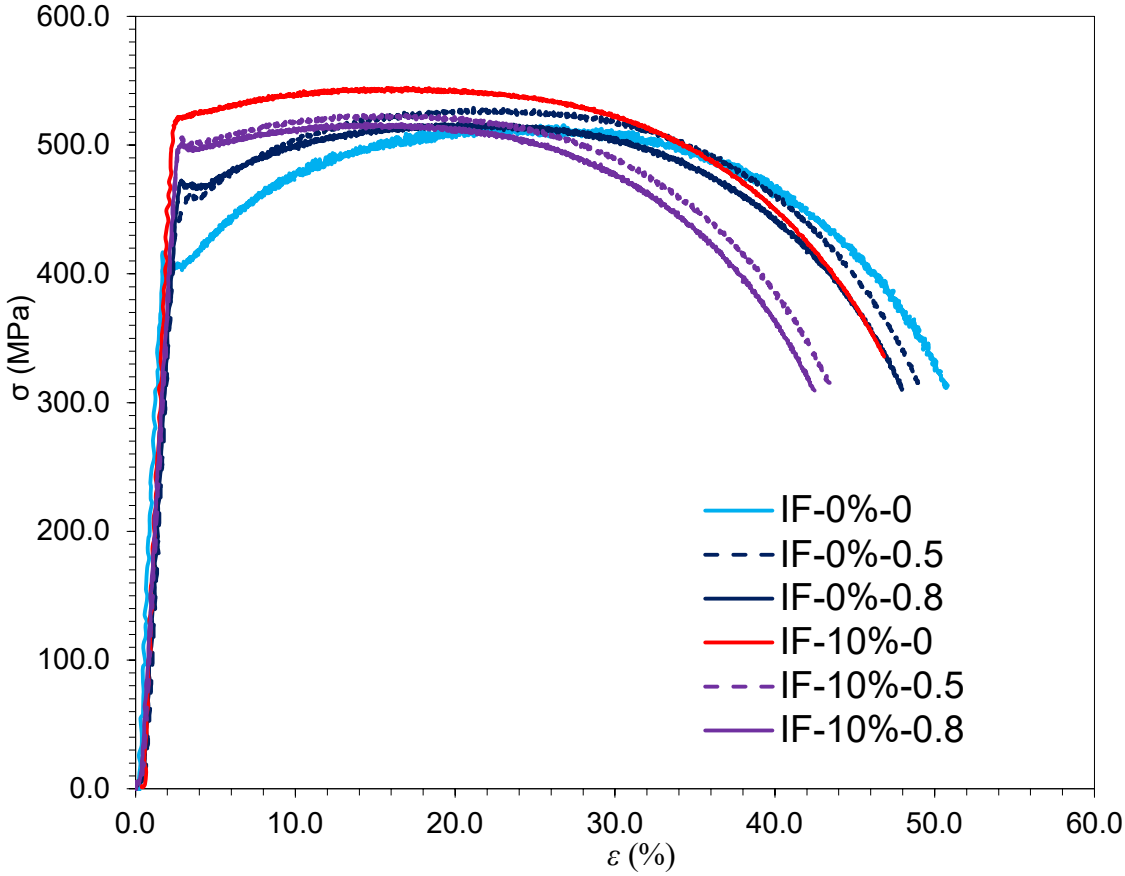

Figure 36 - Comparison of the tensile curves obtained from specimens with different extent of pre-existing fatigue damage, for 0% and 10% pre-strained materials

Table 12 - Summary of mechanical properties obtained from specimens with different extent of pre-existing fatigue damage, for 0% and 10% pre-strained materials

Specimen ID	**Pre-strain level (%)**	***D***	***E* (GPa)**	**σ_Y (MPa)**	**σ_{UTS} (MPa)**	**ε_f (%)**
IF-0%-0	0	0	222	417	518	50.8
IF-0%-0.5	0	0.5	171	466	518	49.3
IF-0%-0.8	0	0.8	176	457	528	48.2
IF-10%-0	10	0	264	516	545	46.6
IF-10%-0.5	10	0.5	197	495	517	43.6
IF-10%-0.8	10	0.8	193	499	524	42.6

5.4.4 Fatigue Crack Growth Tests

Fatigue crack growth tests were performed on three AR specimen (denoted CT-0%-1−3), four 5% pre-strained specimens (denoted CT-5%-1−4) and four 10% pre-strained specimens (denoted CT-10%-1−4). The cycle count and crack length were continuously monitored throughout the tests. Using this data, the fatigue crack growth rate, *da/dN*, was calculated via the incremental polynomial technique and the results were correlated with the linear-elastic fracture mechanic parameter ΔK (i.e., different between K_{max} and K_{min}) which can be calculated using the following equation:

$$K = Y\ \sigma\ \sqrt{\ }\ \pi\ a$$ Equation 5 – Calculation of stress intensity factor

where a is the crack length, $\Delta\sigma$ is the applied stress and Y is a dimensionless shape function, the solutions of which can be found in the literature [23,24]. Moreover, the fatigue crack growth data were analysed to quantify the power-law constants in the secondary fatigue region (also known as the Paris region) calculated following the equation below.

$$\frac{da}{dN} = C(\Delta K)^m$$ Equation 20 – Paris equation

where C and m are known as the Paris law constants which can be identified using a power-law fit to the test data.

The correlation between the fatigue crack growth per cycle, *da/dN*, with ΔK is demonstrated in Figure 37 and the Paris law constants for each data set are summarised in Table 13. As seen in Figure 37 and Table 13, the experimental data sets obtained from materials with different pre-strain levels have been found to fall upon each other indicating that plastic pre-straining doesn't have any noticeable impact on the fatigue crack growth behaviour of the material. This observation on S355 steel is consistent with the data reported on other types of steel in the literature [25][18]. This may be due to the fact that while material pre-straining may increase the yield behaviour of the material, it also decreases the strain at failure (as seen in Figure 33). These behaviours may "cancel" each other out, resulting in similar fatigue crack growth rates between as received and pre-strained material. In addition, curves for the a vs N data for each pre-straining level from the fatigue crack growth testing have been included for reference. Included in Table

13 are the final crack length in fatigue crack growth tests obtained using the unloading compliance data and optical measurements on the fracture surface. As seen in this table, the unloading compliance technique has been found to provide relatively high accuracy for estimation of the instantaneous crack length with the percentage of error found to be below 7%.

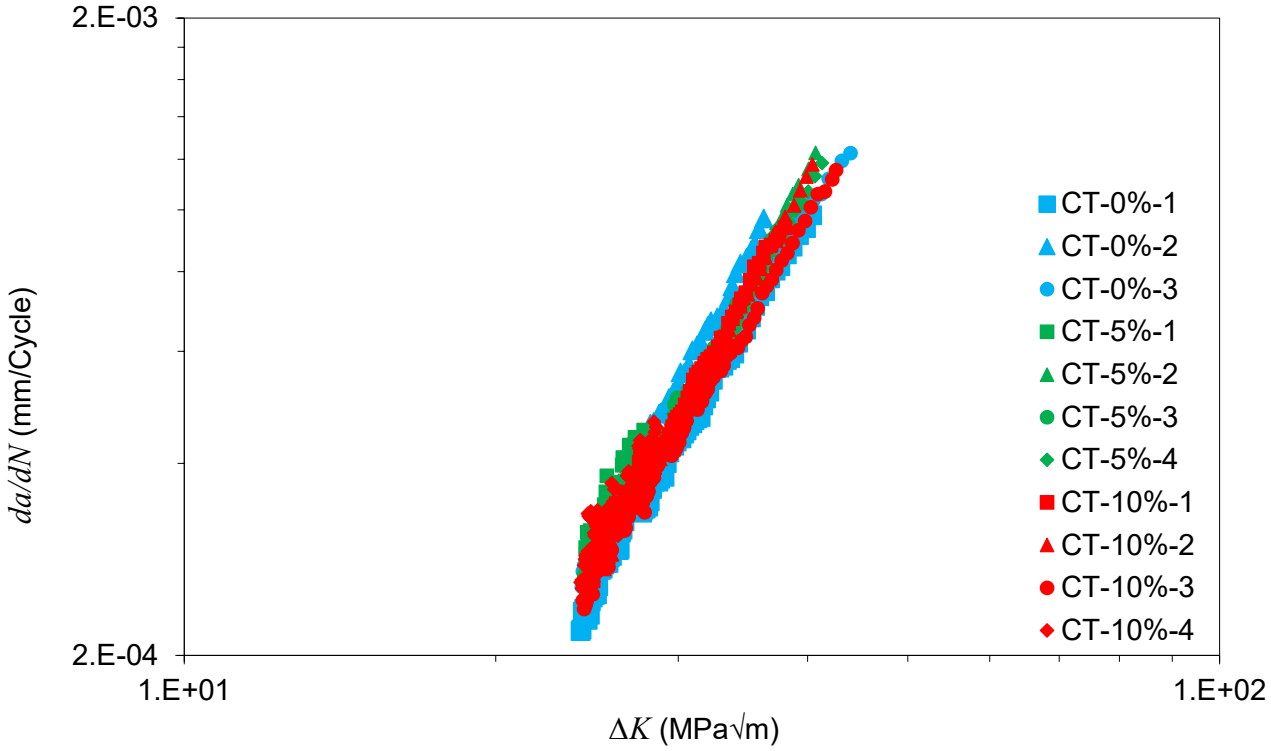

Figure 37 - Fatigue crack growth curves obtained from materials with 0%, 5% and 10% pre-strain levels

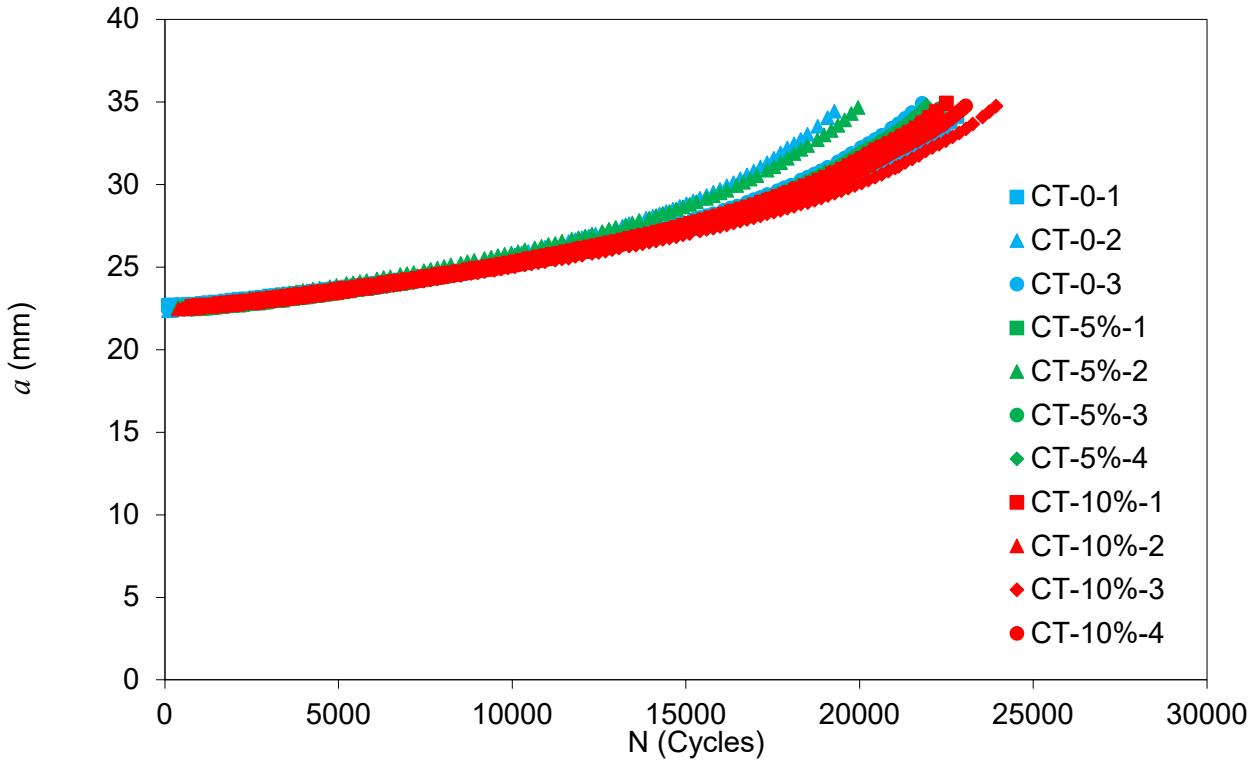

Figure 38 - a vs N data obtained from fatigue crack growth tests for 0%, 5% and 10% pre-strain levels

Table 13 - Paris law constants for each specimen tested on 0%, 5% and 10% pre-strained materials

Specimen ID	**a_f-unloading compliance (mm)**	**a_f-fracture surface (mm)**	**a_f - % error**	***C (*10-^{8})***	***m***
CT-0%-1	35.3	35.2	0.3	2.98	2.82
CT-0%-2	35.1	34.3	2.2	4.45	2.72
CT-0%-3	35.4	35.0	1.0	6.42	2.62
CT-5%-1	35.9	35.2	1.9	4.69	3.41
CT-5%-2	35.9	34.4	4.5	6.71	2.58
CT-5%-3	36.2	35.1	3.2	4.66	2.71
CT-5%-4	35.4	34.6	2.1	8.15	2.54
CT-10%-1	36.6	35.4	3.3	4.74	2.69
CT-10%-2	36.8	34.5	6.6	6.29	2.60
CT-10%-3	36.3	35.4	2.5	6.38	2.59
CT-10%-4	36.8	35.2	4.5	6.22	2.61

In order to evaluate the level of scatter in the fatigue crack growth data, for each material pre-straining level regression analysis has been conducted to work out the upper bound and lower bound trends by calculating and plotting the mean curve ± 2 standard deviations (2SD). The comparison of the mean curve and mean ± 2SD trends for each material data set has been shown in Figure 39(a), (b) and (c) for 0%, 5% and 10% pre-strained material states, respectively, and the Paris law constants are summarised in Table 14. It can be seen in Figure 39 and Table 14 that for each pre-straining level, the there is a small SD in the test data indicating minimal scatter and good repeatability in the fatigue crack growth test data on AR and pre-strained specimens. Comparison of the results shown in Figure 39 and Table 14 also shows that the Paris law constants obtained for the mean curve and the upper bound trend (mean + 2SD) are very similar for different pre-strain levels and the analysed trends fall on top of each other. This confirms that material pre-straining does not have any significant effect on the fatigue crack growth behaviour of the material. Finally included in Table 14 are the coefficients of determination, R^2, for the mean curves fitted to the data points obtained from each material pre-strain levels. As seen in this table, the R^2 values for all three data sets are close to unity confirming that for each pre-strain level the material's behaviour can be accurately described using the Paris law constants presented in Table 14.

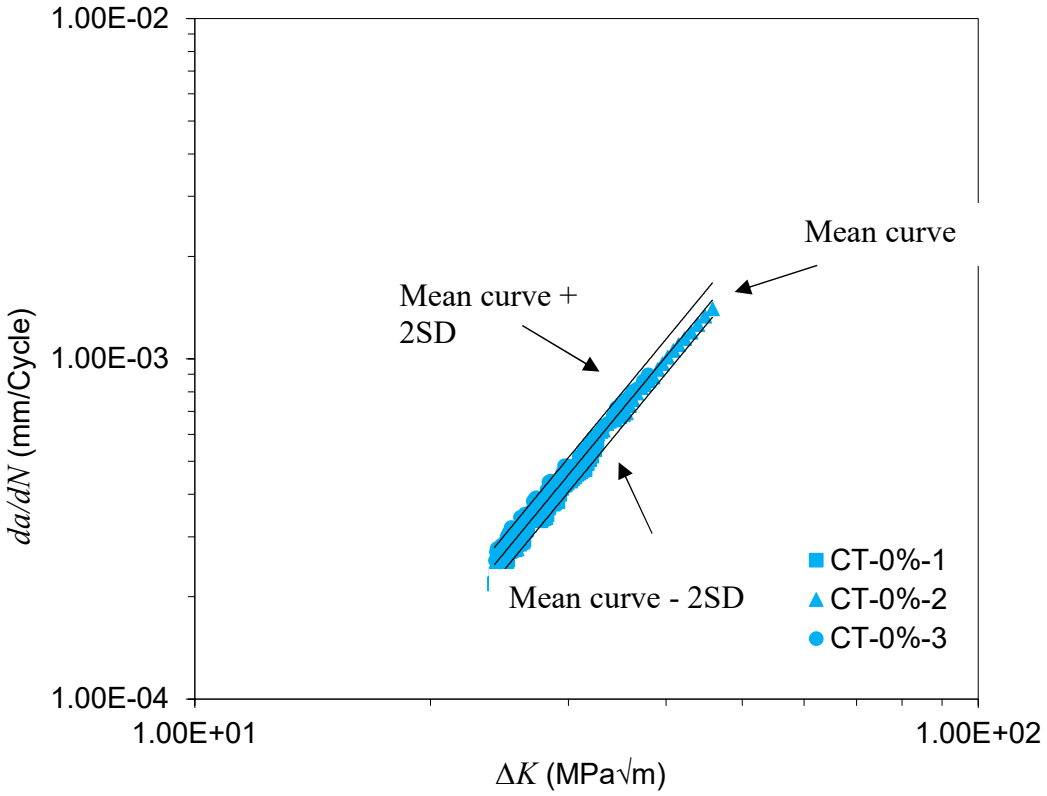
1.00E-02
1.00E-03
1.00E-04
1.00E+01
1.00E+02
da/dN (mm/Cycle)
ΔK (MPa√m)
Mean curve
Mean curve +
2SD
Mean curve - 2SD
CT-0%-1
CT-0%-2
CT-0%-3

(a)

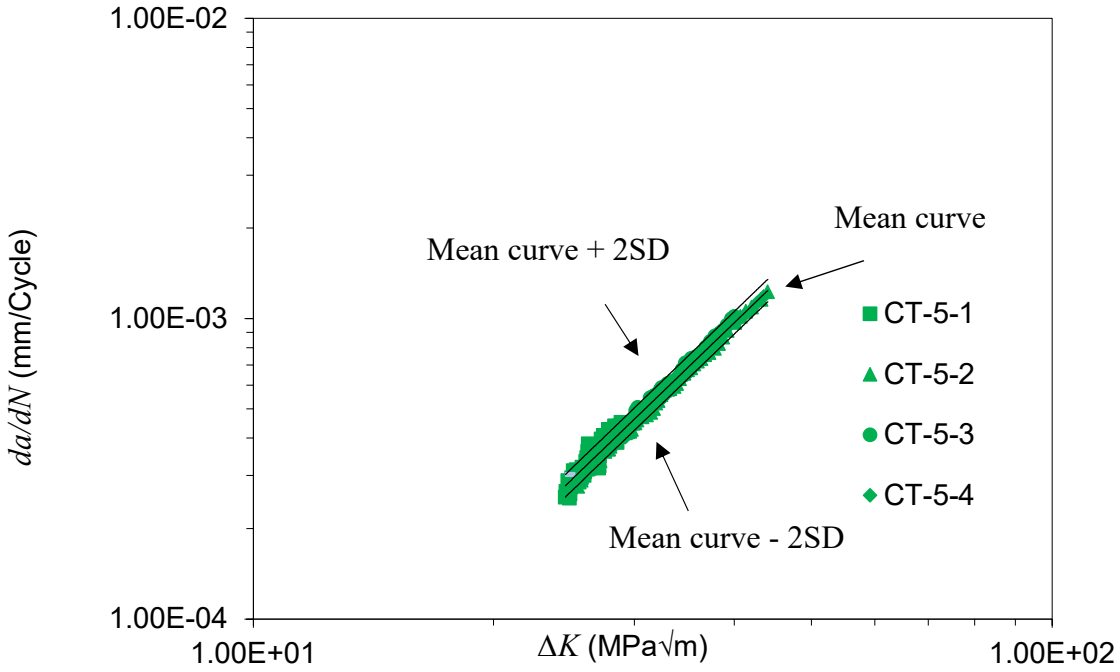

(b)

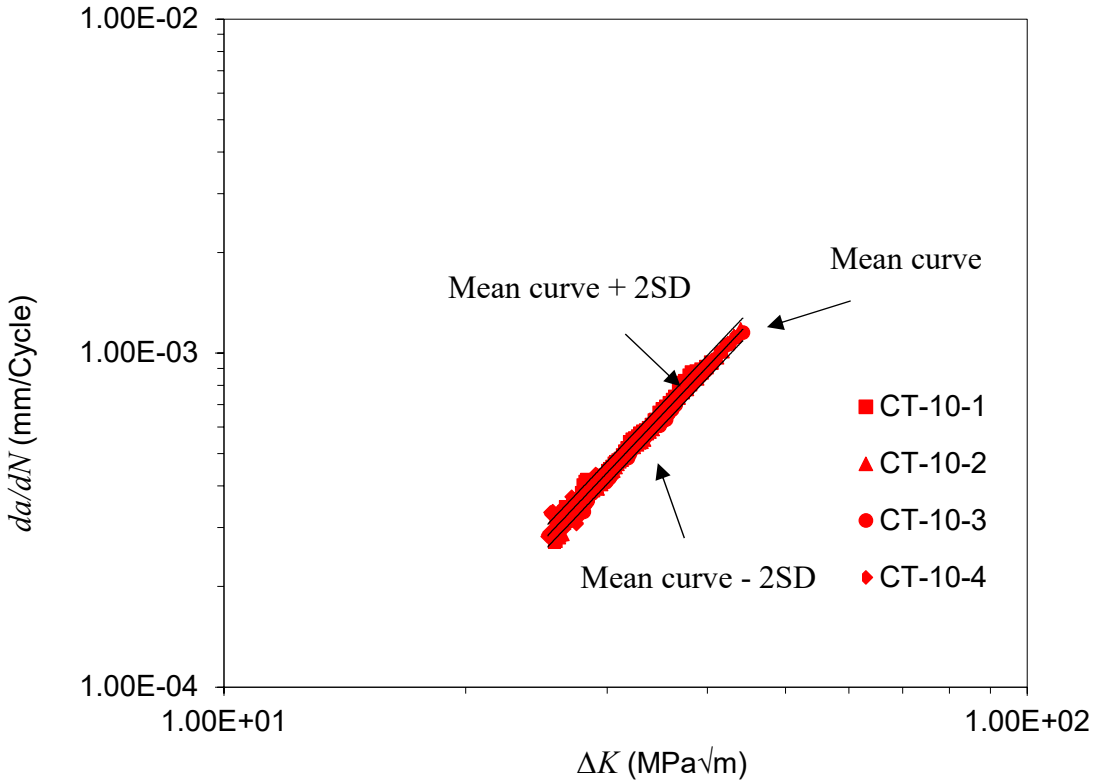

(c)

Figure 39 - Regression analysis of the fatigue crack growth data obtained from the tests on (a) 0%, (b) 5%, and (c) 10%, pre-strained material states

Table 14 - Paris law constants based on mean and mean+2SD curves for 0%, 5% and 10% material data sets

Pre-strain level (%)	Mean curve			Standard Deviation	Mean+2SD	
	C	***m***	R^2		***C***	***m***
0	6.46×10^{-8}	2.59	0.925	0.025	8.77×10^{-8}	2.59
5	2.01×10^{-7}	2.27	0.951	0.019	2.52×10^{-7}	2.27
10	2.04×10^{-7}	2.25	0.978	0.017	2.39×10^{-7}	2.25

5.5 Fractography

Fractography was conducted for all uniaxial fatigue and fatigue crack growth specimens post testing. Figure 40a), b) and c) correspond to the fracture surfaces of uniaxial fatigue specimens which were tested at a stress level corresponding to 86% of the ultimate tensile strength of S355, at pre straining levels of 0%, 5% and 10% respectively. From the fracture surfaces, a smooth portion is visible where the fatigue crack growth would have initiated from the edge of the specimen due to edge effects. This was then followed by ductile tensile fracture of the specimens. This pattern is consistent throughout all fracture specimens, however, with increased pre-straining the fracture surface appears to become smoother in the ductile tensile region; this may be due to the hardening behaviour of the material during pre-straining resulting in a less ductile fracture surface. Uneven fracture surfaces are due to the end of Paris region and the beginning of tertiary fatigue crack growth, hence such features arise which may happen as a result of fast crack growth with some level of plasticity present. Thus, the fatigue crack growth rates from the present study would not be expected to be the same as those provided in BS7910, as they are all in the Paris law regime.

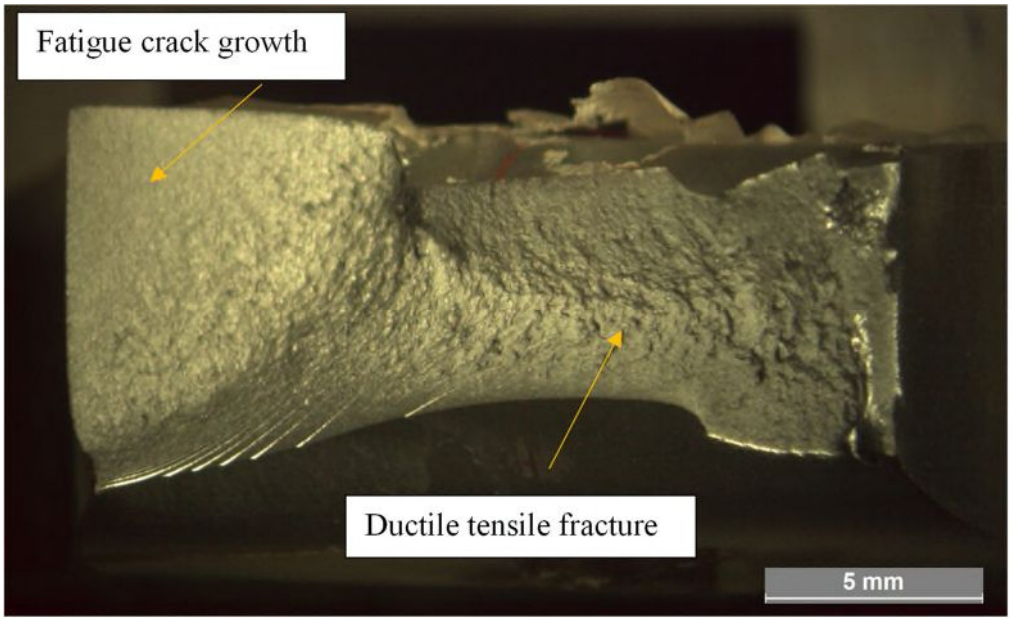

(a)

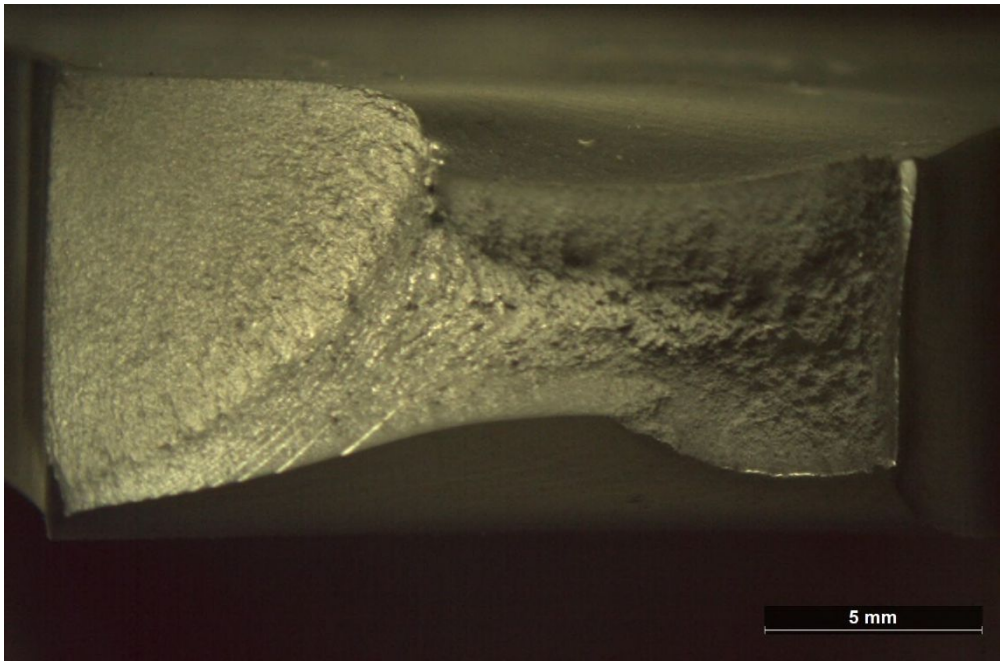

(b)

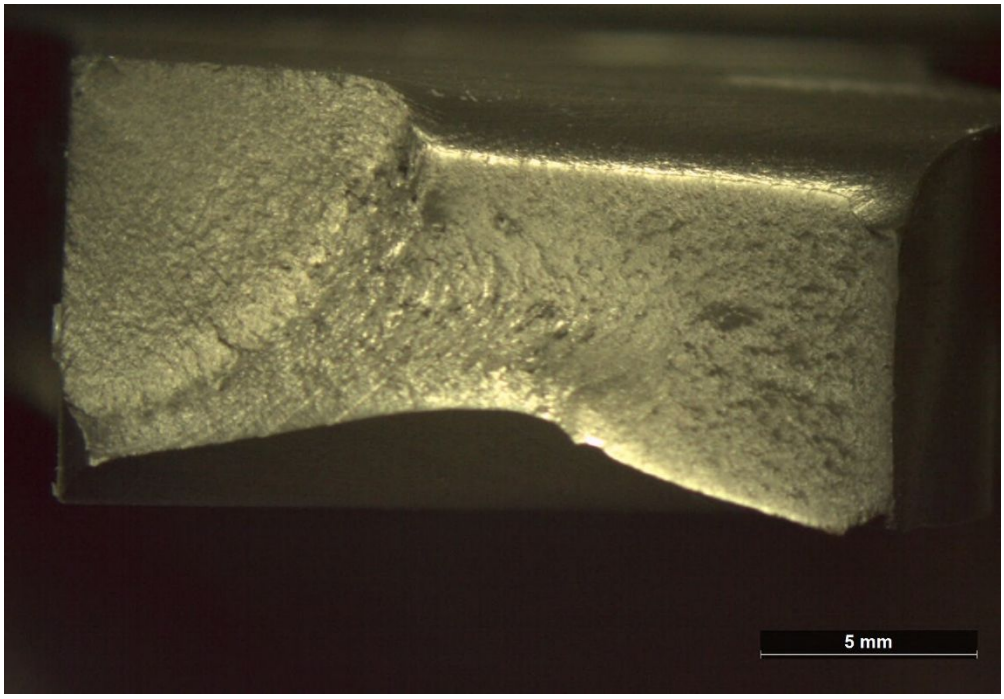

(c)

Figure 40 - Fracture surface of uniaxial fatigue samples with (a) 0%, (b) 5%, (c) 10% pre-strain

Figure 41 shows the fractography images of the C(T) testing post fatigue crack growth testing. Three regions have been identified on the fracture surface during postmortem analysis. The smooth portion of the fracture surface shows the region of pre-fatigue cracking. This was followed by ductile crack extension before the specimen was broken via fast fracture. The uneven fracture surface may be due to the onset of tertiary fatigue crack growth, hence such features may arise as a result of fast crack growth with some level of plasticity present. As there is uniformity in the fatigue crack region, this shows good alignment in the test set up. Measurements from the fractographical assessment were taken and compared to those from the unloading compliance for comparison purposes.

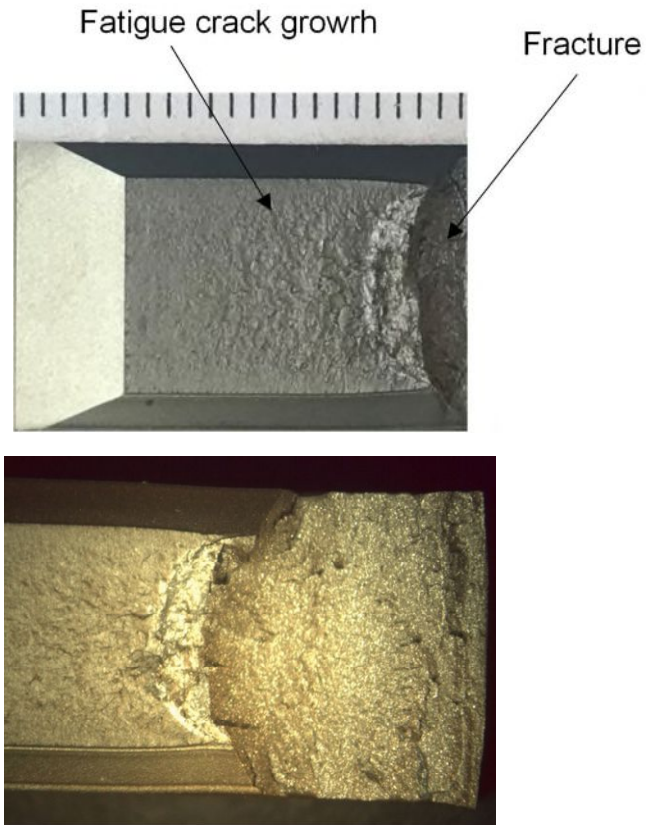

(a)

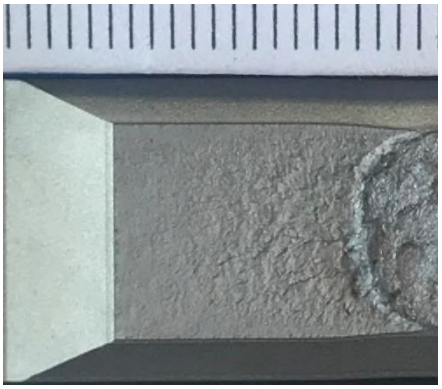

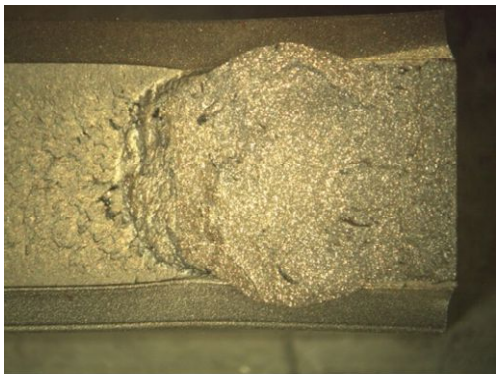

(b)

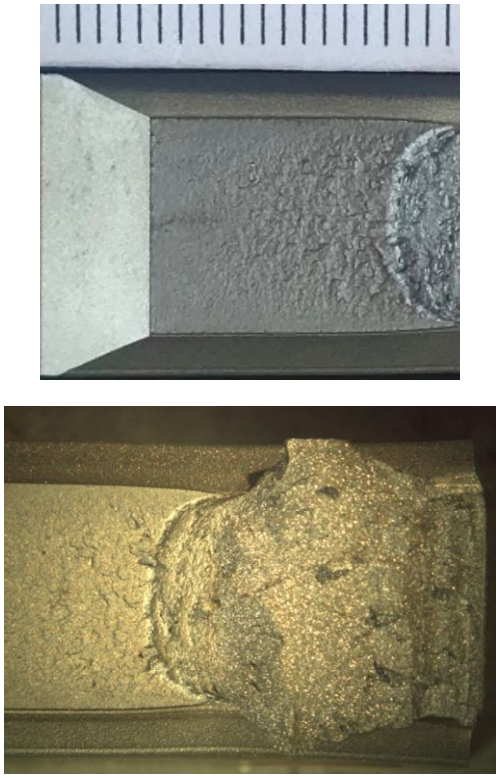

(c)

Figure 41 - Fracture surface of C(T) specimens with (a) 0%, (b) 5%, (c) 10% pre-strain (1 mm distance between division lines on the scale bar)

5.6 Discussion

In order to assess the importance of material pre-straining in fatigue design and life assessment of offshore structures, the obtained uniaxial fatigue data from this study have been compared with the S-N fatigue design curves recommended for the base metal in various design codes and the results are shown in Figure 42 [26,27]][29–34]. It can be seen in this figure that the design curves across various standard bodies differ, with ISO 131819 being the most conservative with fewer cycles to failure, and IIW being the least conservative in the high stress region of the S-N curves. All design curves, for in-air environment, indicate a change in slope once a certain number of cycles have elapsed, with most exhibiting a slope change at 10^7 cycles. An interesting point to note is that the fatigue curve of ISO 13819 is identical to BS 7608, up until the change in the slope at 10^7 cycles. It is believed that these curves may be somewhat under-predictive for the design of offshore structures, and thus, more optimised designs can be made by considering the level of conservatism in these design curves. Comparison of the uniaxial fatigue data on specimens with different level of pre-strain with the S-N fatigue design curves available

in various standards shows that although pre-straining has been found to have a significant effect on the fatigue life of the material, the level of conservatism in all design curves is high enough to suggest significantly lower number of cycles to failure for the pre-strained materials. However, if the design curves are to be revised in the future for reducing the level of excess conservatism, the influence of material pre-straining must be accounted for in the development of the revised curves.

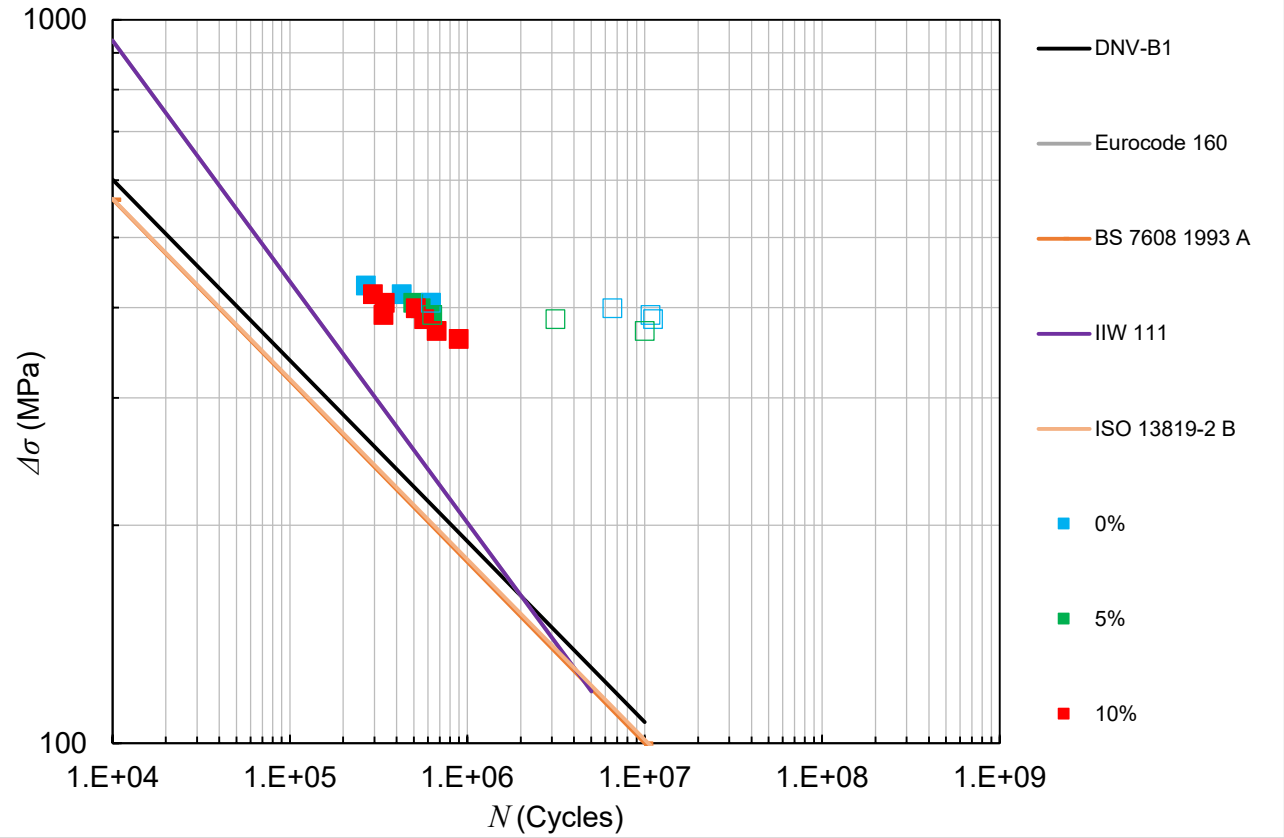

Figure 42 - Comparison of the recommended S-N curves from various standards with the test data obtained from the present study

The results presented in this study exhibited that material pre-straining has insignificant effects on the fatigue crack growth rate of S355 steel, therefore the pre-straining effect does not need to be accounted for in the life assessment of offshore structures. While a similar behaviour has been reported in this literature for pre-tensioning effects in pipe steels, it has been noticed that pre-compression may accelerate the fatigue crack growth rate of the material [18]. A study on pre-compressed SUH660 steel, a steel which is widely used in aircraft engines and gas turbines, also showed that the fatigue crack growth rates were accelerated compared to the AR material state [35]. Knowing that the extent of material pre-straining varies throughout the thickness of offshore wind monopiles, with

tensile plastic strains on the exterior surface of the monopile and compressive strains on the interior [36], the observations in the literature may affect the way monopile defect assessment and inspection are conducted. However, further work may need to be conducted on the compressive pre-straining effects on fatigue crack growth behaviour of S355.

The upper bound fatigue crack growth trends obtained from this study on 0%, 5% and 10% pre-strained material states have been compared with the recommended fatigue crack growth trend in BS 7910 [37] in Figure 43. It can be seen in this figure that while pre-tensioning did not exhibit any noticeable effect on the crack growth behaviour of S355, the upper bound trends obtained from all three material data sets are coincident with the upper bound simplified law curve from BS7910, using the simplified law. The simplified law is typically used for welded joints with an R-ratio of over 0.5. However, it must be noted that the results from base metal tested at R=0.1 align with the higher fatigue crack growth rates which occurs in welded joints, where R>0.5. Therefore, the results obtained from this study suggest that while no consideration needs to be made to account for the influence of material pre-tensioning on the fatigue crack growth behaviour of the material, the fatigue crack growth rates in offshore structures might be under-predicted by using the recommended trends in BS7910, as accelerated fatigue crack growth is illustrated. Further tests need to be conducted in future work to examine the fatigue crack growth rates in pre-compressed S355 material with the crack growth trends recommended in BS7910.

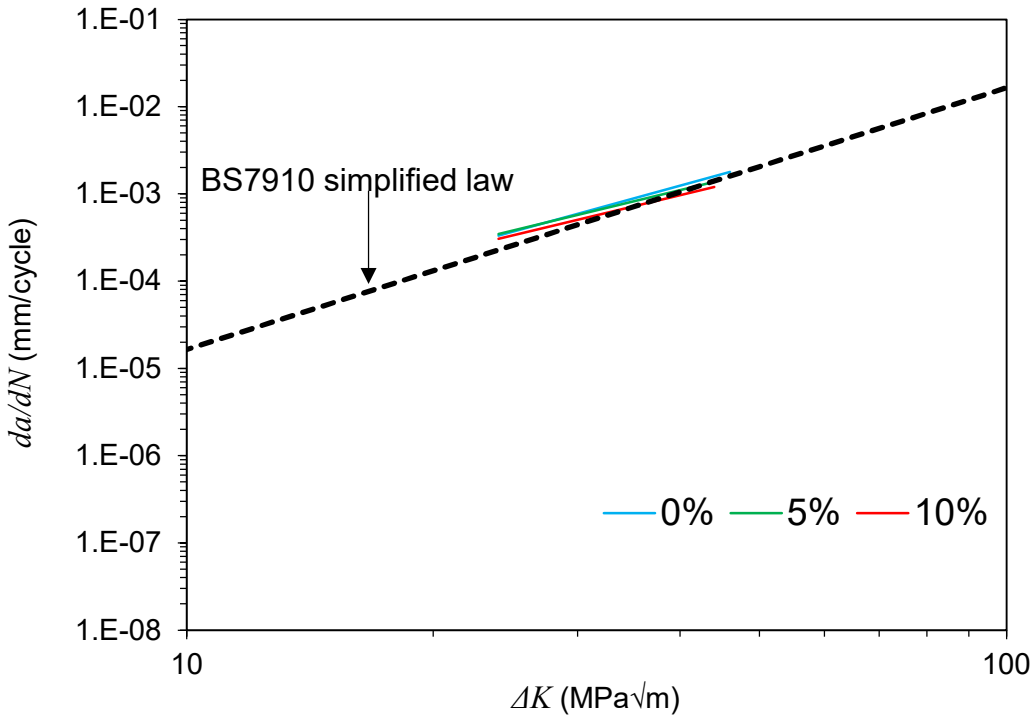

Figure 43 - Comparison of the recommended fatigue crack growth trends in BS7910 with the test data obtained from the present study

5.7 Conclusions

Mechanical, uniaxial fatigue, interrupted fatigue and fatigue crack growth tests were conducted on S355GS+10 structural steel with 0%, 5% and 10% tensile pre-strains states. From the experimental data it was observed that the fatigue life of S355 will significantly decrease with an increase in material pre-straining, particularly at lower stress levels where more than an order of magnitude reduction in fatigue life was found in the 10% pre-strained material. The tensile tests on interrupted fatigue specimens revealed that if the applied stress level during fatigue cycles is less than the yield stress, fatigue damage has insignificant effects on the mechanical behaviour of the material. Finally, it was noted that material pre-tensioning had no significant impact on the fatigue crack propagation behaviour of S355.However further tests must be conducted in future work to examine material pre-compression effects on the fatigue crack growth behaviour. While the S-N fatigue design curves in international standards provide a lower prediction of the fatigue life for the as-received and pre-strained materials, the recommended trends in BS7910 standard may under-predict the fatigue crack growth rates in the as-received and pre-strained materials. Therefore, greater care is required to account for material pre-straining

effects on the fatigue design and life assessment of offshore structures with sufficient safety margins against failure.

5.8 Acknowledgements

This work was supported by grant EP/L016303/1 for Cranfield, Oxford and Strathclyde Universities, Centre for Doctoral Training in Renewable Energy Marine Structures - REMS (http://www.rems-cdt.ac.uk/) from the UK Engineering and Physical Sciences Research Council (EPSRC).

5.9 References

[1] Velarde J, Kramhøft C, Sørensen JD, Zorzi G. Fatigue reliability of large monopiles for offshore wind turbines. Int J Fatigue [Internet]. 2020 May;134:105487. Available from: https://doi.org/10.1016%2Fj.ijfatigue.2020.105487

[2] Esteban MD, Couñago B, López-Gutiérrez JS, Negro V, Vellisco F. Gravity based support structures for offshore wind turbine generators: Review of the installation process. Ocean Eng [Internet]. 2015 Dec;110:281–91. Available from: https://doi.org/10.1016%2Fj.oceaneng.2015.10.033

[3] Negro V, López-Gutiérrez J-S, Esteban MD, Matutano C. Uncertainties in the design of support structures and foundations for offshore wind turbines. Renew Energy [Internet]. 2014 Mar;63:125–32. Available from: https://doi.org/10.1016%2Fj.renene.2013.08.041

[4] Igwemezie V, Mehmanparast A, Kolios A. Current trend in offshore wind energy sector and material requirements for fatigue resistance improvement in large wind turbine support structures {\textendash} A review. Renew Sustain Energy Rev [Internet]. 2019 Mar;101:181–96. Available from: https://doi.org/10.1016%2Fj.rser.2018.11.002

[5] Jacob A, Oliveira J, Mehmanparast A, Hosseinzadeh F, Kelleher J, Berto F. Residual stress measurements in offshore wind monopile weldments using neutron diffraction technique and contour method. Theor Appl Fract Mech [Internet]. 2018;96(June):418–27. Available from: https://doi.org/10.1016/j.tafmec.2018.06.001

[6] Orlando L. Review of Design Procedures for Monopile Offshore Wind Structures. 2015.

[7] Pérez-Collazo C, Greaves D, Iglesias G. A review of combined wave and offshore wind energy. Renew Sustain Energy Rev [Internet]. 2015 Feb;42:141–53. Available from: https://doi.org/10.1016%2Fj.rser.2014.09.032

[8] Anandavijayan S, Mehmanparast A, Brennan F. A numerical analysis of the effects of manufacturing processes on material pre-strain in offshore wind monopiles. In: Procedia Structural Integrity. 2018.

[9] Lotsberg I. Fatigue Design of Marine Structures. Cambridge University Press; 2016.

[10] Mehmanparast A, Davies CM, Dean DW, Nikbin K. Effects of plastic pre-straining level on the creep deformation, crack initiation and growth behaviour of 316H stainless steel. Int J Press Vessel Pip [Internet]. 2016 May;141:1–10. Available from: https://doi.org/10.1016%2Fj.ijpvp.2016.03.013

[11] Baek J hyun, Kim Y pyo, Kim C man, Kim W sik, Seok C sung. Effects of pre-strain on the mechanical properties of API 5L X65 pipe. Mater Sci Eng A. 2010;527(6):1473–9.

[12] Zhang YH, Maddox SJ, Manteghi S. Verification of Class B S-N curve for fatigue design of steel forgings. Int J Fatigue [Internet]. 2016;92:246–61. Available from: http://dx.doi.org/10.1016/j.ijfatigue.2016.07.015

[13] Kwon J, Jeong D, Choi I, Kim Y, Woo N, Kim S. Fatigue behavior of api x-80 steels. ASME Int Mech Eng Congr Expo Proc. 2012;3(PARTS A, B, AND C):1211–8.

[14] Bhargava AK, Sharma C. Mechanical Behaviour of Materials. 2011.

[15] de Jesus AMP, Matos R, Fontoura BFC, Rebelo C, da Silva LS, Veljkovic M. A comparison of the fatigue behavior between S355 and S690 steel grades. J Constr Steel Res [Internet]. 2012 Dec;79:140–50. Available from: https://doi.org/10.1016%2Fj.jcsr.2012.07.021

[16] Forni D, Chiaia B, Cadoni E. High strain rate response of S355 at high temperatures. Mater Des [Internet]. 2016 Mar;94:467–78. Available from: https://doi.org/10.1016%2Fj.matdes.2015.12.160

[17] Pawliczek R, Prażmowski M. Study on material property changes of mild steel S355 caused by block loads with varying mean stress. Int J Fatigue [Internet]. 2015 Nov;80:171–7. Available from: https://doi.org/10.1016%2Fj.ijfatigue.2015.05.019

[18] Hagiwara N, Masuda T, Oguchi N. Effects of Prestrain on Fracture Toughness and Fatigue-Crack Growth of Line Pipe Steels. J Press Vessel Technol [Internet]. 2001 Apr;123(3):355–61. Available from: https://doi.org/10.1115%2F1.1379531

[19] Chiou YC, Yang JK. The effects of pre-deformation on the subsequent fatigue behaviors of SUS 430 Stainless Steel in load-control. Int J Solids Struct [Internet]. 2012;49(23–24):3263–8. Available from: http://dx.doi.org/10.1016/j.ijsolstr.2012.06.023

[20] Le Roux JC, Taheri S, Sermage JP, Colin J, Fatemi A. Cyclic deformation and

fatigue behaviors of stainless steel 304L including mean stress and pre-straining effects. Am Soc Mech Eng Press Vessel Pip Div PVP. 2008;3:411–20.

[21] Guo YB, Ho HC, Chung KF, Elghazouli AY. Cyclic deformation characteristics of S355 and S690 steels under different loading protocols. Eng Struct. 2020;221(June).

[22] Forni D, Chiaia B, Cadoni E. Strain rate behaviour in tension of S355 steel: Base for progressive collapse analysis. Eng Struct [Internet]. 2016 Jul;119:164–73. Available from: https://doi.org/10.1016%2Fj.engstruct.2016.04.013

[23] ASTM E647−13. Standard Test Method for Measurement of Fatigue Crack Growth Rates. Am Soc Test Mater. 2014;1–50.

[24] Mehmanparast A, Brennan F, Tavares I. Fatigue crack growth rates for offshore wind monopile weldments in air and seawater: {SLIC} inter-laboratory test results. Mater Des [Internet]. 2017 Jan;114:494–504. Available from: https://doi.org/10.1016%2Fj.matdes.2016.10.070

[25] Mehmanparast A. The Influence of Inelastic Damage on Creep,Fatigue and Fracture Toughness. Dep Mech Eng. 2012;PhD(September).

[26] Brandi R, Rossetto P. Fatigue design of offshore structures. Weld Int. 1987;1(12):1155–61.

[27] Eurocode 3: Design of Steel Structures - Part 1-9: Fatigue . 2011;1(2005).

[28] The British Standards Institution. BS 7608: Code of practice for fatigue design and assessment of steel structures. 2014;

[29] A. Hobbacher. IIW document IIW-1823-07 FATIGUE DESIGN OF WELDED. 2008;

[30] HSE. Offshore technology report 2001/083 - Comparison of Fatigue Provisions in Codes and Standards. 2002; Available from: http://www.hse.gov.uk/research/otopdf/2001/oto01083.pdf

[31] BSI. BS 7608: Code of practice for fatigue design and assessment of steel structures. 1993;

[32] ISO. ISO 13819-2: Petroleum and Natural Gas Industries - Offshore Structures - Part 2: Fixed Steel Structures. 1999;

[33] HSE. Offshore Installations: Guidance on Design, Construction and Certification. 1993;

[34] NORSOK. Design of Steel Structures. 1998;

[35] Wu H, Hamada S, Noguchi H. Pre-strain effect on fatigue strength characteristics of SUH660 plain specimens. Int J Fatigue [Internet]. 2013;55:291–8. Available from: http://dx.doi.org/10.1016/j.ijfatigue.2013.06.021

[36] Anandavijayan S, Mehmanparast A, Brennan F. A numerical analysis of the effects of manufacturing processes on material pre-strain in offshore wind monopiles. Procedia Struct Integr [Internet]. 2018;13:953–8. Available from: https://doi.org/10.1016%2Fj.prostr.2018.12.178

[37] BS 7910. BSI Standards Publication Guide to methods for assessing the acceptability of flaws in metallic structures. BSI Stand Publ. 2015;(UK):490.

6. The effects of material pre-straining on the failure assessment of offshore wind monopile structures

Satya Anandavijayan[1], Ali Mehmanparast[1]*, Feargal Brennan[2] and Amir Chahardehi[3]

[1] Offshore Renewable Energy Engineering Centre, Cranfield University, MK43 0AL, UK

[2] Naval Architecture, Ocean & Marine Engineering Department, University of Strathclyde, G4 0LZ, UK

[3]Atkins Energy, Westminster, London, SW1E 5BY, UK

*Corresponding author: a.mehmanparast@cranfield.ac.uk

Abstract

Inspection is an important aspect to be considered in the operation and maintenance of offshore wind monopile structures. The failure assessment diagram approach is a method which has been developed over the past 50 years, and most commonly used is the method outlined in BS7910. This approach suggests three levels of failure assessment, each increasing in complexity to determine whether a flaw may be deemed as "acceptable". It is near impossible to have a flawless structure, and these flaws can initiate at the surface, before forming a through thickness crack. This can be something which is introduced into the structure during the fabrication process, alongside material pre-straining. The aim of this study is to investigate the effects of material pre-straining on the behaviour of defect and failure assessment of offshore wind monopile structures. Using data from tensile, fracture toughness, and fatigue crack growth tests, failure assessment has been carried out to determine the influence of material pre-straining on the structural integrity of monopiles. The effects of free corrosion in seawater, over a range of loading conditions, have been factored into calculations to give conservative estimates of remaining life in the presence of a crack. From the study, it has been concluded that material pre-straining can retard fatigue crack growth, although the failure assessment data points lie closer to the failure assessment line with increasing pre-straining.

Keywords: failure assessment diagram, engineering critical assessment, fitness for purpose assessment, material pre-straining, offshore wind monopile, S355

Nomenclature

a	Length or depth of surface crack-like flaw
a_f	Final crack length
a_i	Initial crack length
b	Thickness
c	Crack length
K_r	Fracture ratio
K_I	Stress intensity factor

K_{IC}	Fracture toughness considering ductile tearing
J_e	*J*-integral
J_{el}	Value of *J* using elastic analysis
L_r	Load ratio
E	Youngs Modulus
Y	Non dimensional shape function
v	Poisson's ratio
C	Paris constant *C*
σ_{UTS}	Ultimate tensile stress
σ_y	Yield stress
σ_{ref}	Reference Stress
m	Paris constant *m*
t	Monopile thickness

6.1 Introduction

Cracks and flaws commonly arise during fabrication or in service around features such as cable entry holes or welds (1). Structural integrity assessment plays a key role in the design and inspection of offshore wind monopile structures. However, there is minimal experience regarding this compared to the tried and tested oil and gas standards. It is, however, recommended that inspection of the wind turbine is considered, considering the maintenance and operation history (2). The failure assessment diagram (FAD) methodology is an efficient way to assess the likelihood of material failure in the presence of cracks. As the monopile ages, it is of priority to determine the critical flaw size for intervention and life extension. Cracks are commonly detected via non-destructive techniques such as eddy current, magnetic particle inspection, ultrasonic testing, alternating current field measurement and visual inspection (3).

The FAD approach was originally derived from a two-criterion approach, which states that structures or components can fail by either plastic collapse or brittle fracture. If the service assessment point falls within the boundaries given by the failure assessment line, the structure is considered safe. This method by Dowling and Townley enables plastic

instability calculations using LEFM calculations (4)(5). Although there are many guides for failure assessment, the most commonly used are BS7910 and API 579 (6)(7).

The concept has been widely developed over the past 50 years and the PD6493 procedure is now known as BS7910 (8). B7910 differs from PD6493 as it includes changes to the fracture mechanics and fatigue assessment procedures, as well as additional procedures for defect assessment in high temperatures.

B7910 is the standard commonly used to determine the failure assessment of structures, with three alternative assessment approaches available for structural integrity assessment, increasing in complexity with each level of assessment. The document includes 22 annexes, many originating from the widely known R6 failure assessment diagram concept. Each approach utilises a failure assessment line (FAL) which is specified by an equation, with a cut of value of $L_{r,max}$. An acceptable flaw would have its K_r and L_r values lying under this failure assessment line. This approach allows for different materials and geometries. (9).

Option 1 failure assessment is the simplest of the three failure assessment methods (also known as the “simplified assessment” procedure), and does not require detailed stress-strain data, resulting in lower estimations.

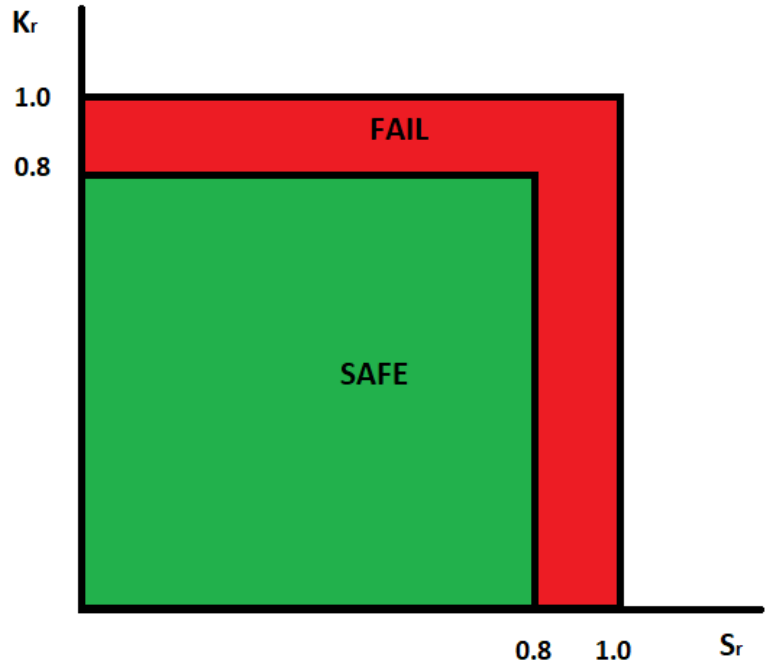

Figure 44 - Option 1 FAD

Option 2 failure assessment, known as the "normal assessment" procedure, incorporates full uniaxial tensile data. There are two levels available: Levels 2A and 2B, dependent on the type of tensile data available for the material. This option also accounts for yield discontinuity.

Option 3 failure assessment is specific to the particular material, geometry and loading conditions and can be determined using both elastic and elastic-plastic analyses of the flawed structure, as a function of primary and secondary stresses. This is considered an alternative approach to options 1 and 2. While it may predict structural behaviour more accurately, it may require more detailed analysis such as finite element analysis to determine driving force.

In the standard BS7910 Level 2A/3A general failure assessment diagram is presented as:

$$K_r = (1 - 0.4L_r^2)[0.3 + 0.7exp(-0.65L_r^6]$$

Equation 39 – BS7910 equation for the calculation of K_r at Level 2A/3A

Where:

$$K_r = \frac{K_I}{K_{IC}} = \sqrt{\frac{J_{elastic}}{J_{total}}}$$

Equation 40 – Correlation between Kr and J integral

Or alternatively K_r can be calculated by:

$$K_r = \frac{K_I}{K_{IC}}$$

Equation 41 – Calculation of K_r

Where:

$$K_{IC} = \frac{K^2(1-v^2)}{E}$$

Equation 42 – Calculation of K_{IC}

J_{IC} can be converted to K_{mat} by:

$$K_{mat} = \sqrt{\frac{E}{1-v^2}} * J_{IC}$$

Where E is the young's modulus

v is the Poisson's ratio

And

$$L_r = \frac{total\ applied\ load\ giving\ rise\ to\ \sigma^P\ stresses}{plastic\ collapse\ load\ of\ the\ flawed\ structure}$$

Equation 43 – Calculation of L_r

Or

$$L_r = \frac{\sigma_{ref}}{\sigma_{yield}}$$

Equation 44 – Numerical calculation of L_r

Where σ_{ref} reference stress corresponds to the membrane stress (only primary stresses have been considered)

Stable ductile tearing under fatigue can be introduced into the failure assessment procedure by incorporating fatigue crack growth data. Thus, the total crack growth Δa_{tot} can be calculated by summation of the initial crack size and cyclic crack growth.

$$L_r = \frac{\sigma_{ref}}{\sigma_{yield}}$$

$$K_I = Y\,\sigma\sqrt{\pi a}$$

$$K_r = \frac{K_I}{K_{IC}}$$

$$K_{IC} = \frac{K^2(1-v^2)}{E}$$

Fatigue crack growth calculations have been performed by integrating the Paris equations to find the number of cycles (10). For stage one calculations (part through thickness), a_i has been taken as 1mm. For stage two calculations (through thickness), a_i is the final crack length from stage one calculations.

Equation 25 – Integration of Paris law

$$\frac{da}{dN} = C\Delta K^m = C(Y\Delta\sigma\sqrt{\pi a})^m$$

$$\therefore \int_0^{N_f} dN = \int_{a_i}^{a_f} \frac{da}{CY^m\Delta\sigma^m(\pi a)^{\frac{m}{2}}}$$

$$N_f = \frac{1}{CY^m\Delta\sigma^m\pi^{\frac{m}{2}}}\,a_f\left[\frac{a^{-\frac{m}{2}+1}}{-\frac{m}{2}+1}\right]$$

$$= \frac{1}{CY^m\Delta\sigma^m\pi^{\frac{m}{2}}}\left[\frac{a_f^{1-\frac{m}{2}} - a_i^{1-\frac{m}{2}}}{1-\frac{m}{2}}\right]$$

A case study using data for the Thames Estuary where the London Array wind farm is located has been used to illustrate this (11). The monopile used for the study was 59mm thick with a diameter of 5.2m. For example, using an initial through thickness crack size of 80mm (which would correspond to the average final crack length from stage one

calculations), the expected lifetime of the monopile before failure would be estimated in as received material as 3.2 years, during normal operating conditions. However, if the plastic pre-straining present within the thickness of the monopile can is 10%, this new lifetime would decrease to 2.2 years. As the level of material pre-straining will differ through the thickness of the material, a worst case scenario approach should be taken, and thus the lifetime of 2.2 years should be used.

However, the accidental limit state is an extreme scenario which is commonly utilised in industry, to consider the effects of any potential accidents such as unexpected loading on the structure. This is typically calculated to be a stress of around 75% of the material yield strength and therefore is assumed to be 75% of the mean yield value measured from tests for illustrative purposes.

Table 15 - Loading conditions for consideration

	Membrane Stress (MPa)
Normal	97
Extreme Wave	167
Extreme Wind	216
Cut-out wave + Extreme Wind	127
Wind-wave Misalignment	167
Accidental Limit State	387

A potential place for flaws to initiate and propagate are around the cable holes of offshore wind monopiles (12). These are typically machine cut into the can at a 45° angle, followed by grinding to avoid sharp edges. Since this is an area of stress concentration, cracks can still initiate and propagate from the edges, and these cracks soon develop into surface cracks, and then propagate through the thickness of the monopile can (Figure 45). Once the crack has reached the thickness of the monopile can, the crack then propagates and "unzips" its way around the monopile circumference. A typical limit for this unzipping before failure is believed to be around a quarter of the monopile circumference (9). Since the flaw is being recharacterized at each stage, it is of best practice to create a failure assessment diagram for each stage.

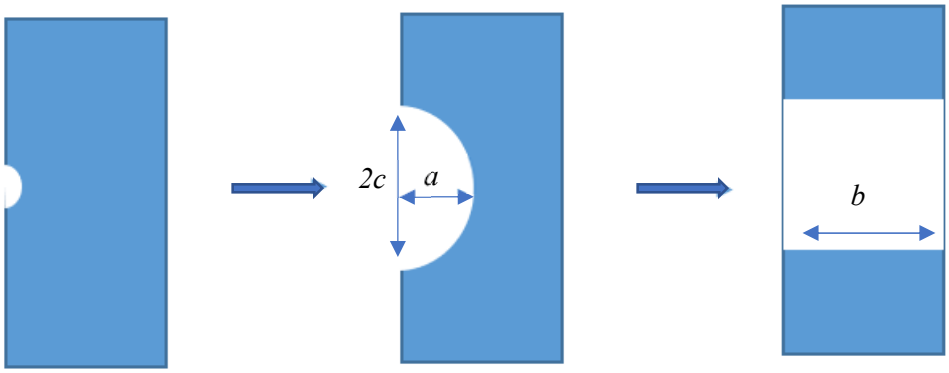

Figure 45 - Recharacterisation of flaws

6.2 Calculation Methodology for S355 experimental data

Experimental test data for as received and pre-tensioned S355 specimens at ambient temperature has been analysed. Data has been extracted from a total of 28 specimens (C(T) and dog-bone) which have been prepared and pre-strained at 0%, 5% and 10%, before tensile, fracture toughness, and fatigue crack growth experiments have been performed. Fracture toughness and fatigue crack growth C(T) specimens have been previously side grooved to 30% prior to testing. Crack growth has been monitored using the unloading compliance technique and has been validated by specimen break open and performing fractography. Fatigue crack growth tests have been conducted in air, and to compensate for this, an environmental reduction factor (ERF) of 2 has been incorporated into fatigue crack growth calculations for direct comparison to results from SLIC seawater tests (13)(14). Incorporating such a factor into the fatigue crack growth equation allows for an estimation of crack growth in seawater conditions, using data from experiments conducted in air.

The experimental test results and SLIC interlaboratory test results have been fed into Option 2 FAD assessments over a range of different loading regimes a monopile may be subjected to over the course of its operation. These loading conditions range from “normal” to accidental limit state to assess the flaw over different scenarios. In addition, Paris law constants derived from the fatigue crack growth test data from both the

experimental testing and SLIC interlaboratory tests have been used to examine the effects of pre-straining on the fatigue crack growth of flaws. There are differences in fatigue crack growth rate between the results of the present study and those of SLIC, and this is believed to be due to the differences in specimen geometry between the two studies. It would be believed that the results from the present study would be more applicable for the future thicknesses of monopiles, due to the increased level of constraint in the specimens. Results from the SLIC data would be believed to be applicable for the current generation of monopiles, however the present study may be more applicable to the future monopile thicknesses, which are believed to reach thicker wall thicknesses.

Both FAD and fatigue crack growth assessments have been performed to cover two stages: stage one will look at the propagation of an initial flaw size of a = 1mm and $2c$ = 5mm propagating through the full thickness of the monopile can (60mm). Once a full thickness crack of a = 60mm has been achieved, the defect assessment is continued in the second stage. Stage two defect assessment looks at maximum flaw size of the through thickness crack, "unzipping" through the circumference of the monopile can and its limits. The initial crack length for through thickness crack growth will start using the final crack length from the previous assessment. Using the values from Table *15*, the maximum allowable flaw size was calculated by rearranging Equation 5 to form:

$$a_f = \frac{1}{\pi} * \left(\frac{\sigma_{ref}}{K_{IC}}\right)^2$$

Equation 45 – Calculation of a_f

Comparisons of data from assessments have been made comparing the effects of material pre-straining on defect assessment and fatigue crack growth rate. Fatigue crack growth calculations have been presented in terms of months until failure. Free corrosion conditions have been assumed for all data sets for comparative purposes. As BS7910 recommends Paris constants of mean + 2 standard deviations to be used in fatigue crack growth calculations, these have been the values used in all calculations (9). Table 17 lists the Paris law constants used in the software. Paris law constants from previous chapters have been converted from mm/cycle to m/cycle for ease of input into Crackwise 6 software. ΔK values have also been converted from MPa$\sqrt{m}$ to N/mm$^{3/2}$.

For illustrating the method of using FAD, a realistic S-N life of 250 years for the parent material is assumed here. The cyclic loading that results in this S-N life has been used for the calculation of crack growth rates. In industry, monopiles are typically designed for a lifetime of 25 years of service, however a design fatigue factor (DFF) of 3 is commonly utilised due to welds, but for parent plate this would be around 10. Thus, it can be assumed that the average monopile is designed for a lifetime of 250 years.

Design calculations for structures in the North Sea typically use a number of 7.5 million load cycles per year, which is believed to be consistent with the annual number of cyclic wave loadings in the North Sea. Therefore, monopile structures are typically designed to withstand approximately 1.875 x 10^9 wave cycles. Back engineering using S-N curves from DNV C203 (15) can be performed to calculate the stress range to be used in fatigue crack growth calculations. Using the assumption of 1.875 x 10^9 cycles, the B2 SN curve for gas cut non welded joints in seawater with free corrosion can be extrapolated, giving a corresponding equivalent average fatigue stress range of approximately 9.9 MPa. Due to limitations in experimental data for Paris law constants for prestrained material in seawater, a detail in air must be considered.

Table 16 - Material properties of S355 for FAD assessment

	0%	5%	10%
Yield Stress (MPa)	417	468	516
Ultimate Tensile Strength (MPa)	517	532	545
Young's Modulus (MPa)	222000	222000	222000
Poisson's Ratio	0.3	0.3	0.3
K_{IC} (MPa.√m)	458.05	439.84	417.65

Fracture toughness values presented in Table *16* are an average of K_{IC} obtained from previous experiments.

Table 17 - Paris constants for fatigue crack growth analysis

	0%	5%	10%

	Present Study	SLIC	Present Study	SLIC	Present Study	SLIC
C	3.81-11	1.25E-12	8.15E-11	1.25E-12	8.26E-11	1.25E-12
m	2.795	3.86	2.567	3.86	2.544	3.86

6.3 Results and Analysis

6.3.1 Surface to Through Thickness Crack

The first FAD analysis which was conducted was for the propagation of the crack from the surface through the thickness of the monopile. To construct the failure assessment diagrams and calculate the fatigue crack growth, TWI Crackwise 6 was used. For this study, an initial crack size of a = 1mm and $2c$ = 5mm was assumed. The final crack length (a) was 60mm.

Failure assessment diagrams for stage one failure assessment are presented in Figure 46, Figure 48, Figure 50 for as received, 5% and 10% pre-straining respectively. In all three pre-straining conditions, all the data points for each loading condition sit within the failure assessment line. From these figures it can be seen for all pre-straining levels, that for each the data points using experimental test results with environmental reduction factor (ERF) lie much closer to the failure assessment line compared to those from the SLIC project. For this reason, it could be argued that the experimental test results with the experimental reduction factor (ERF) are more conservative. However, the gap between the present study with ERF and SLIC data points close as the pre-straining level increases. For 5% and 10%, the accidental limit state data points for both present study and SLIC data sit dangerously close to the FAL (failure assessment line). In this instance immediate intervention would be strongly recommended in the event of a fault condition. Table 18 presents the number of months required for the initial crack to fully propagate through the thickness. From the values presented in the table, it can be clearly seen that the results utilising the environmental reduction factor (ERF) of 2 are much more conservative than those using SLIC project Paris constants, and this trend is further illustrated in the curves in Figure 47, Figure 49 and Figure 51. In addition to this, the accidental limit state condition has a slightly shorter lifetime before the through thickness crack has propagated through the full thickness. Most interestingly, it would appear that an increase in material

pre-straining results in an increase in duration for the crack to propagate through the thickness. As material pre-straining increases, the increase in expected duration also increases. This may be an important factor to consider in overall inspection planning, as if a known level of material pre-straining is present, this could potentially achieve more time in between inspections. However, the opposite is seen in the case of the accidental limit state. Unlike all other loading conditions, the accidental limit state duration before failure decreases with pre-straining. In this instance, it would be recommended that immediate intervention takes place, as pre-straining decreases the fatigue life duration.

Table 18 – Estimated life (months) of crack in stage one for each pre-straining level

	0%		5%		10%	
	Present Study	SLIC	Present Study	SLIC	Present Study	SLIC
Normal	28.6	51	29.4	51	31.4	51
Extreme Wave	28.6	51	29.4	51	31.4	51
Extreme Wind	28.4	50.9	29.4	51	31.4	51
Cut-out Wind + Extreme Wave	28.6	51	29.4	51	31.4	51
Wind-wave Misalignment	28.6	51	29.4	51	31.4	51
Accidental Limit State	27.5	50.5	28.1	50.6	29.7	50.5

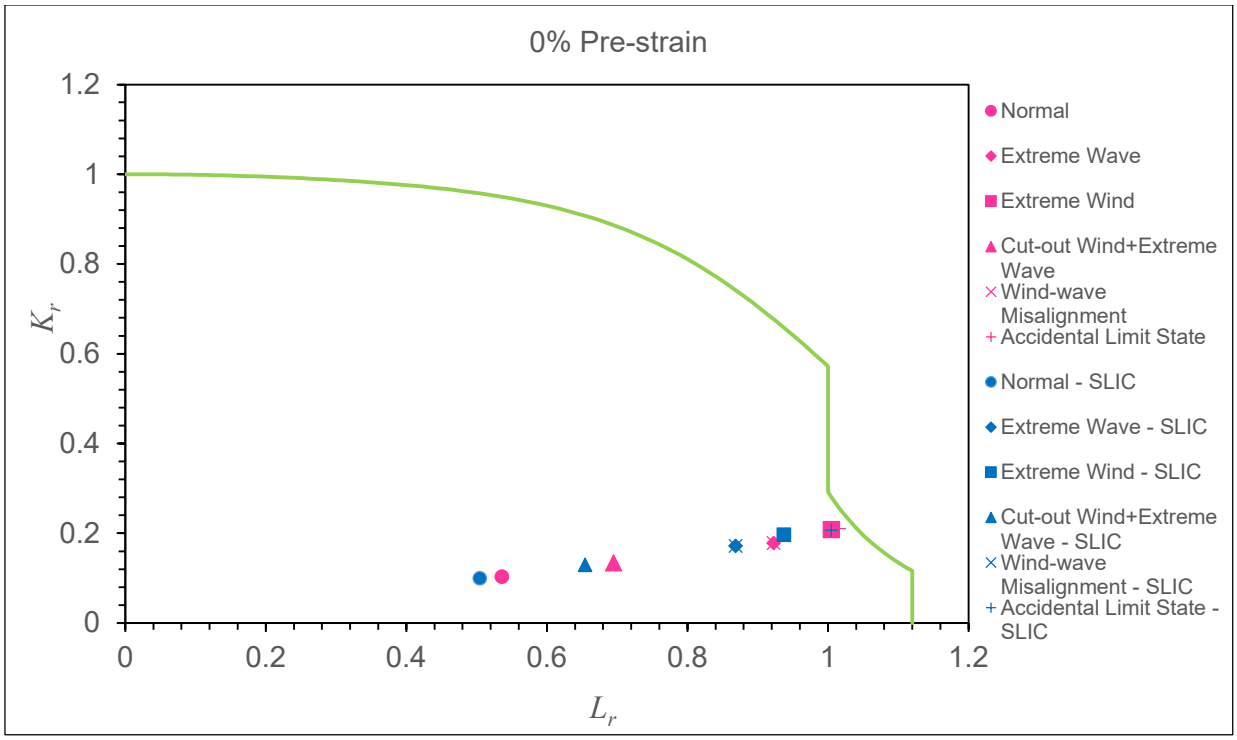

Figure 46 – FAD for surface to through thickness crack for 0% pre-straining condition

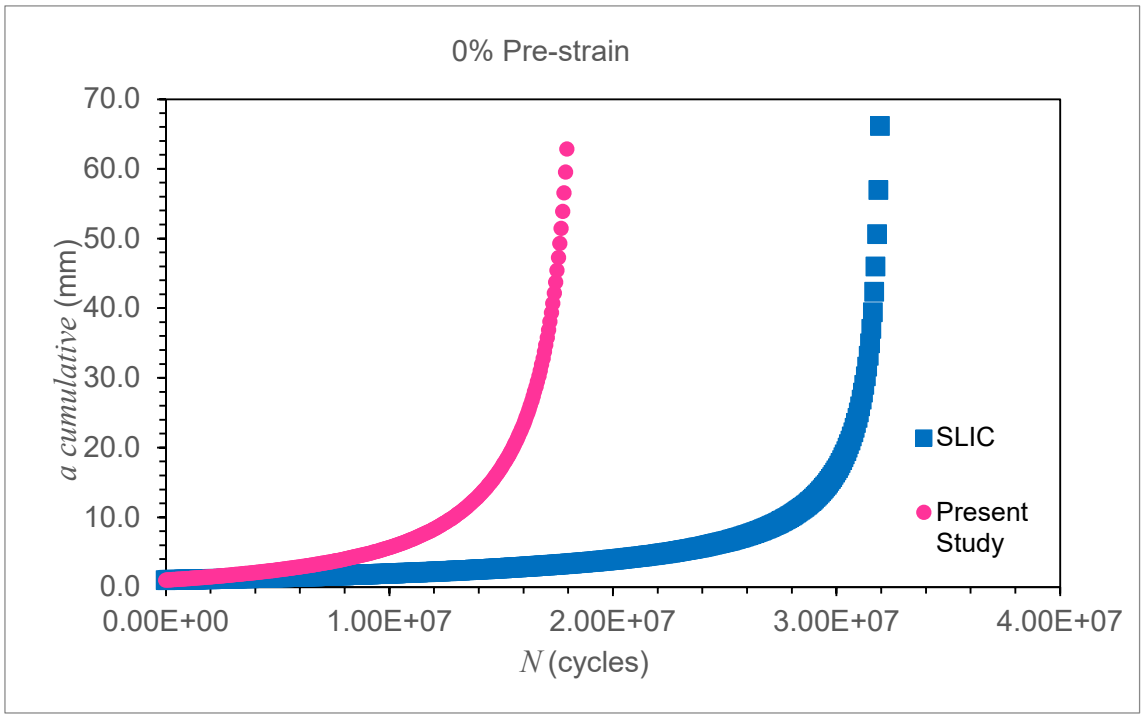

Figure 47 – Fatigue crack growth rates for 0% pre-strain for present study vs SLIC data

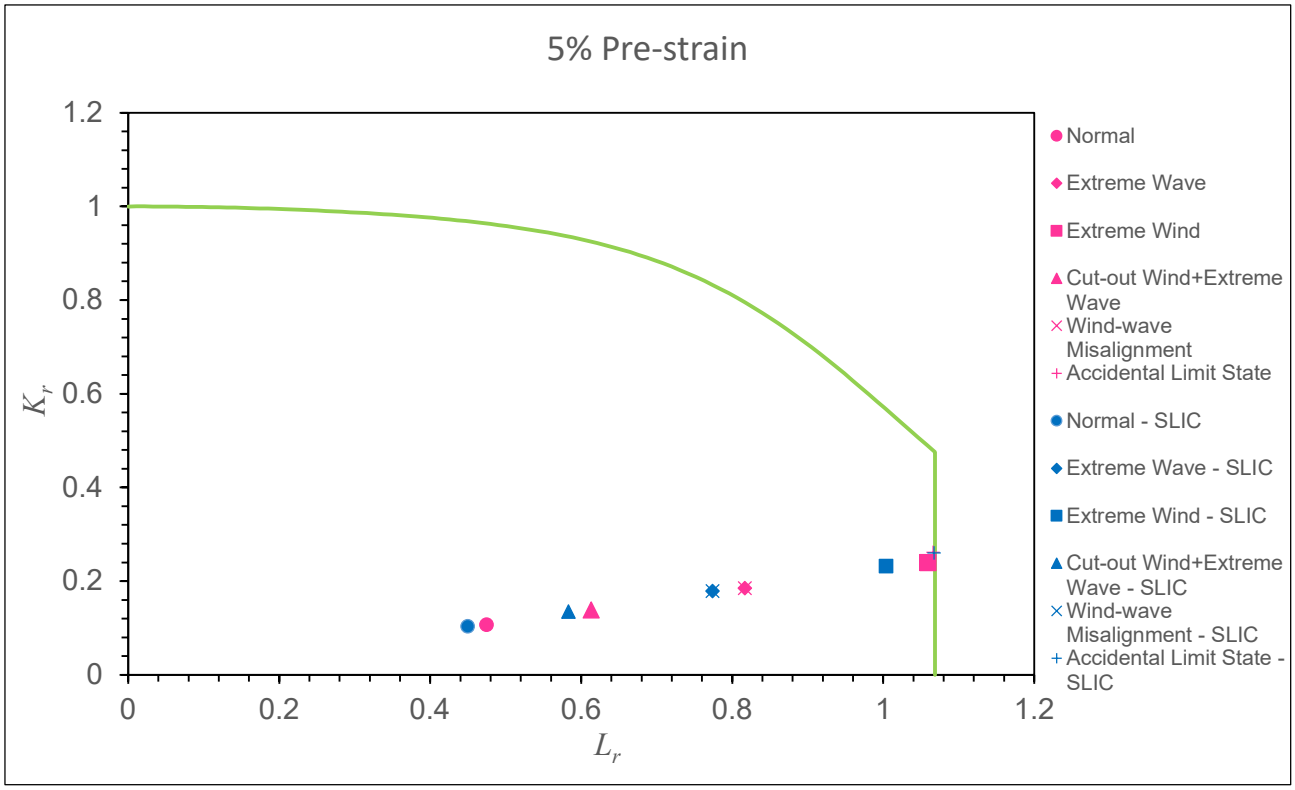

Figure 48 - FAD for surface to through thickness crack for 5% pre-straining condition

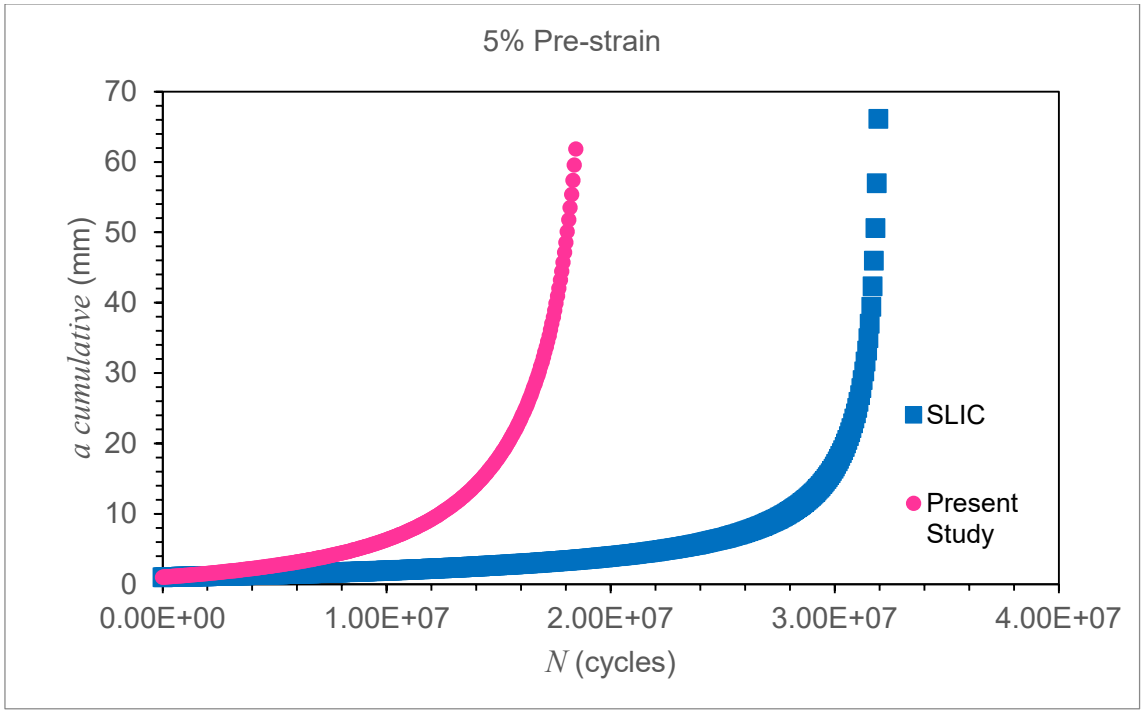

Figure 49 - Fatigue crack growth rates for 5% pre-strain for present study vs SLIC data

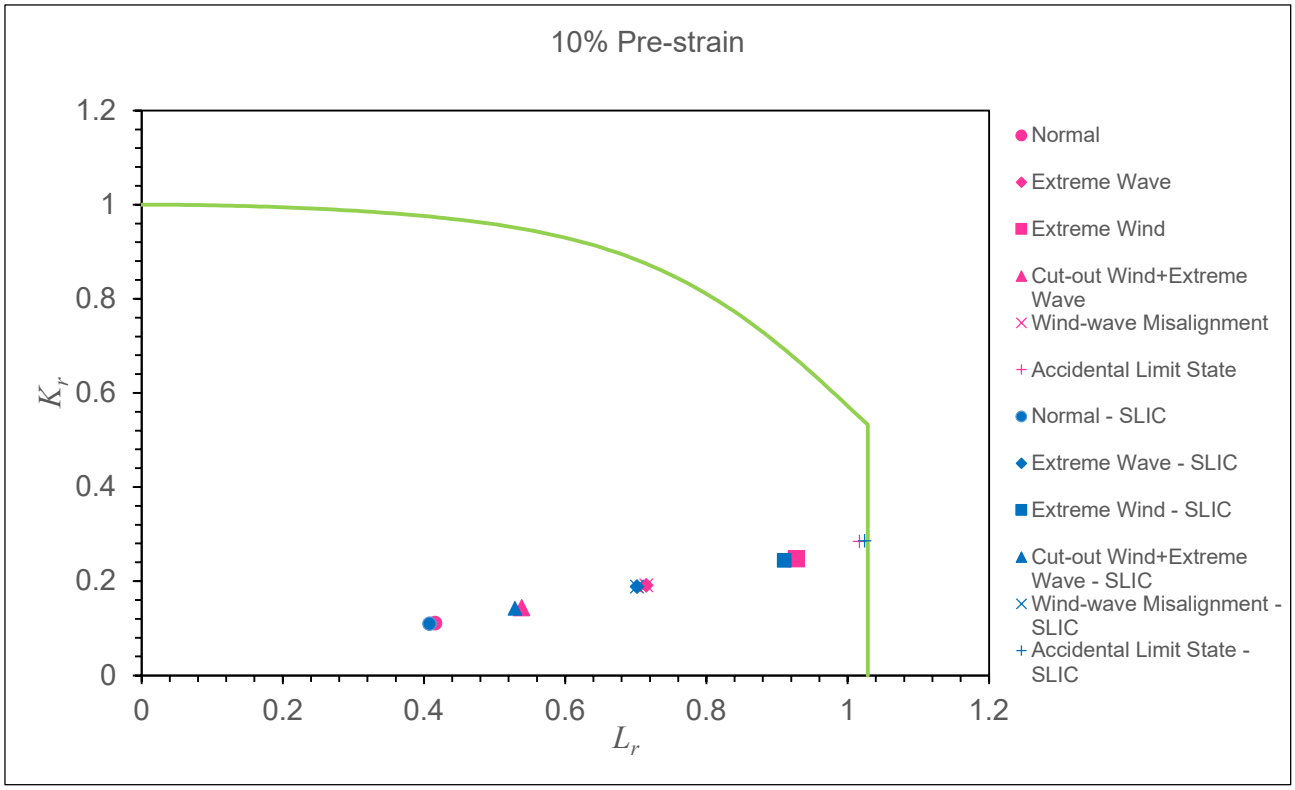

Figure 50 - FAD for surface to through thickness crack for 10% pre-straining condition

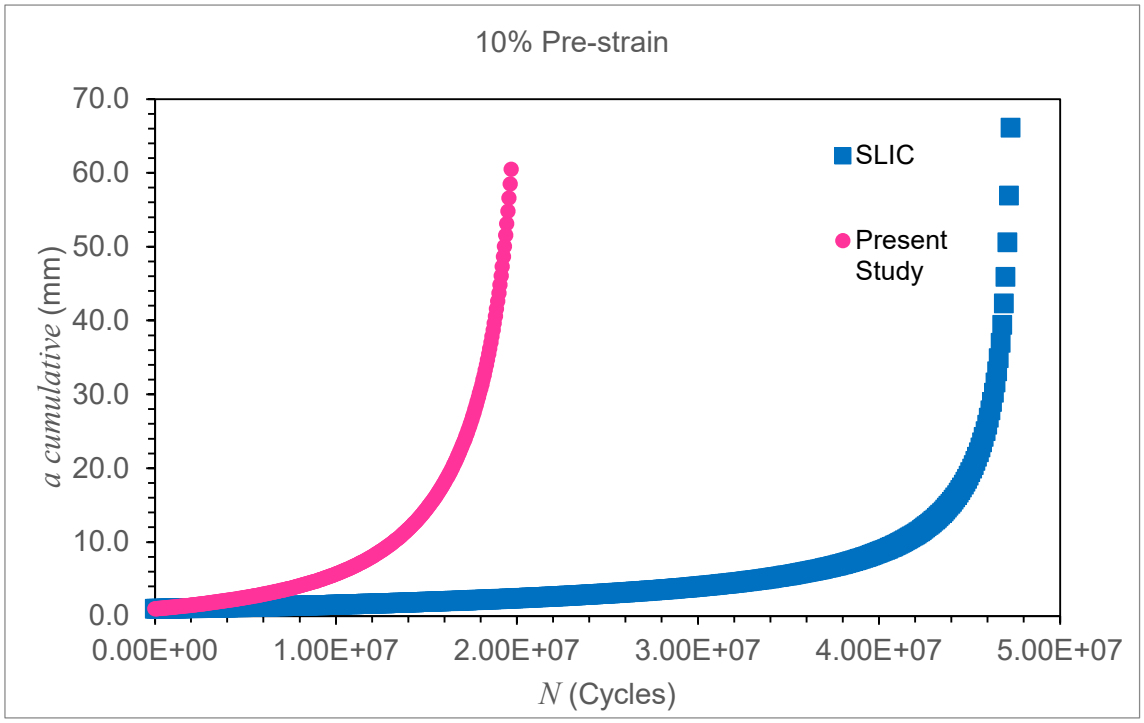

Figure 51 - Fatigue crack growth rates for 10% pre-strain for present study vs SLIC data

6.3.2 Through Thickness Crack Propagation

Stage two failure assessment involves determining the maximum crack length the crack can propagate around the circumference prior to catastrophic failure. The industry best practice does not recommend a crack size larger than 25% of the circumferential monopile length due to loss of accuracy (9), and therefore for a monopile of diameter of 5.2m, this maximum crack length would be calculated as 4.08m. Following on from the initial stage one FAD assessment, the initial crack length for stage two would average around 0.08m, as this was the final crack length at the end of the first analysis. At this stage, it can be seen that the monopile is still deemed "safe" to continue being in operation, as all data points are well within the failure assessment line.

Calculated maximum flaw sizes for each loading condition have been presented in Table 19. Assuming the maximum flaw size is 4.08m for a 5.2m diameter monopile, it is interesting to note that the maximum allowable flaw differs with each loading condition. For example, from the FAD calculations, for normal operating conditions, a maximum flaw size of 4.08m would be considered a lower limit as the FAD has calculated max flaw sizes exceeding this length, of maximum crack sizes of 5.93-7.12m. However, for more extreme limit states, this may be considered under-conservative. For example, in the case of Extreme Wind, for as received material it has been estimated that the critical flaw size is less than half of this figure, ranging from 1.19-1.43m. Another interesting point to note is that as material pre-straining increases, the maximum flaw size will decrease, without significant difference in fatigue crack growth over 5%, compared to the difference between 0% and 5% pre-straining. In addition, it must be taken into account that BS7910 solutions assume that a defect is in the centre of an infinite body, however, this may not be true for individual circumstances (9). In industrial context, these are very large values and are not limiting considerations, as a repairability limit which is much shorter than these lengths should prevail.

Table 19 – Maximum flaw size with respect to pre-straining and loading condition

	Max Flaw Size (m)		
	0%	5%	10%
Normal	7.13	6.57	5.93
Extreme Wave	2.41	2.22	2.00

Extreme Wind	1.43	1.32	1.19
Cut-out wave + Extreme Wind	4.24	3.91	3.53
Wind-wave Misalignment	2.41	2.22	2.00
Accidental Limit State	0.71	0.50	0.37

Table 20 – Estimated crack duration for each pre-straining condition (months)

	0%	5%	10%
Normal	38.0	31.3	26.2
Extreme Wave	35.6	27.8	22.7
Extreme Wind	32.8	25.0	20.3
Cut-out Wind + Extreme Wave	38.6	30.4	25.0
Wind-wave Misalignment	35.6	27.8	22.7
Accidental Limit State	27.8	18.5	13.5

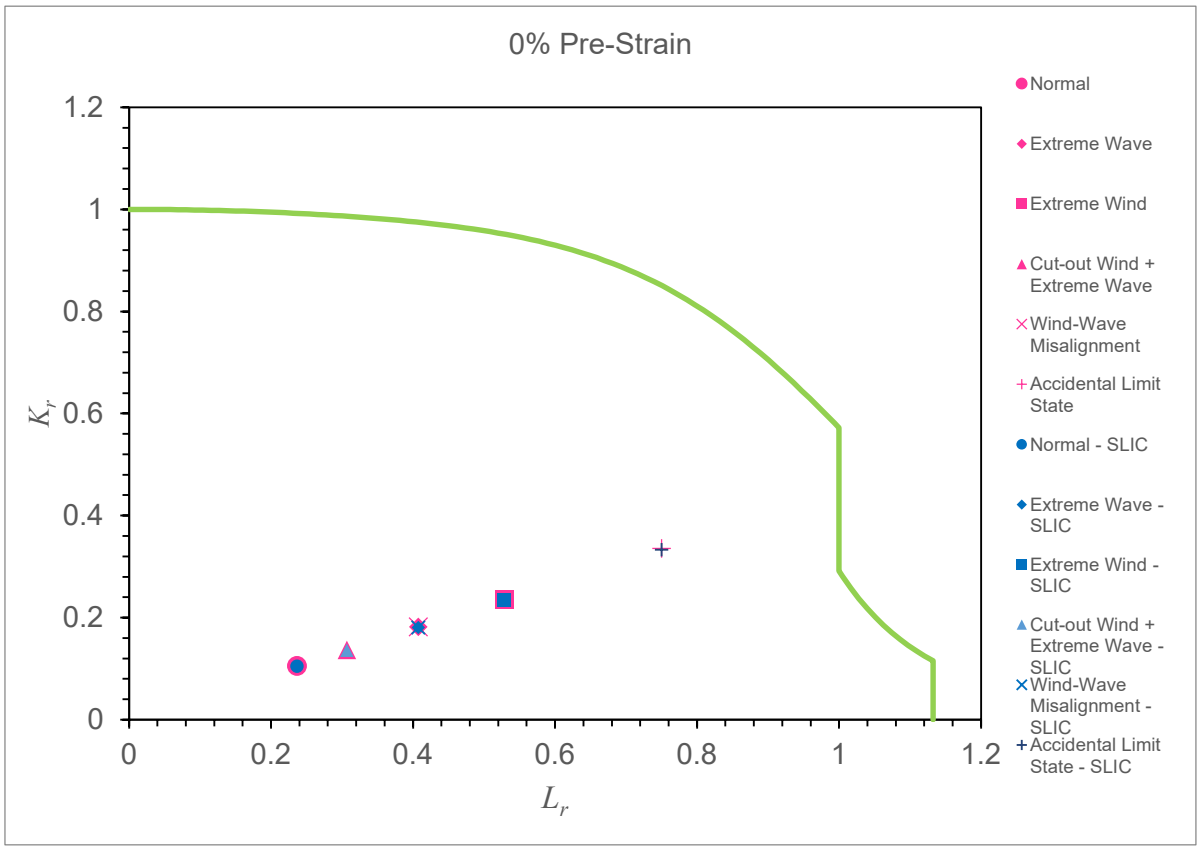

Figure 52 – Through thickness FAD for 0% pre-straining condition for present study and SLIC data

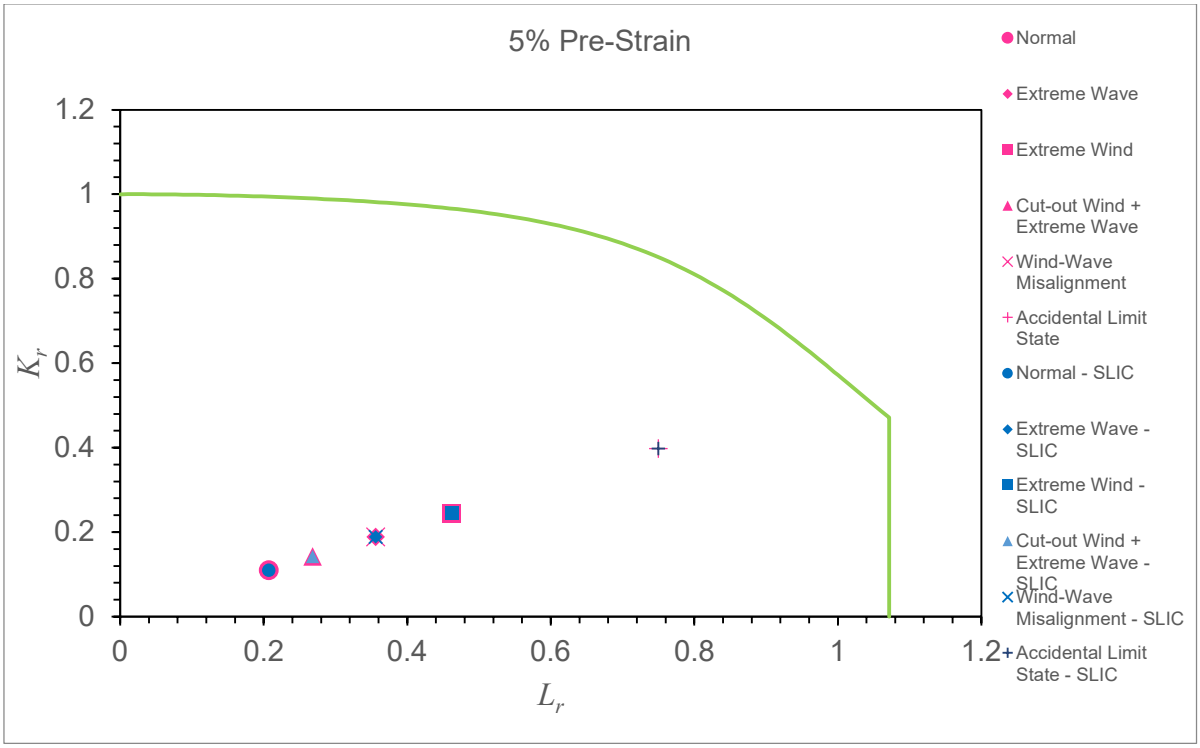

Figure 53 - Through thickness FAD for 5% pre-straining condition for present study and SLIC data

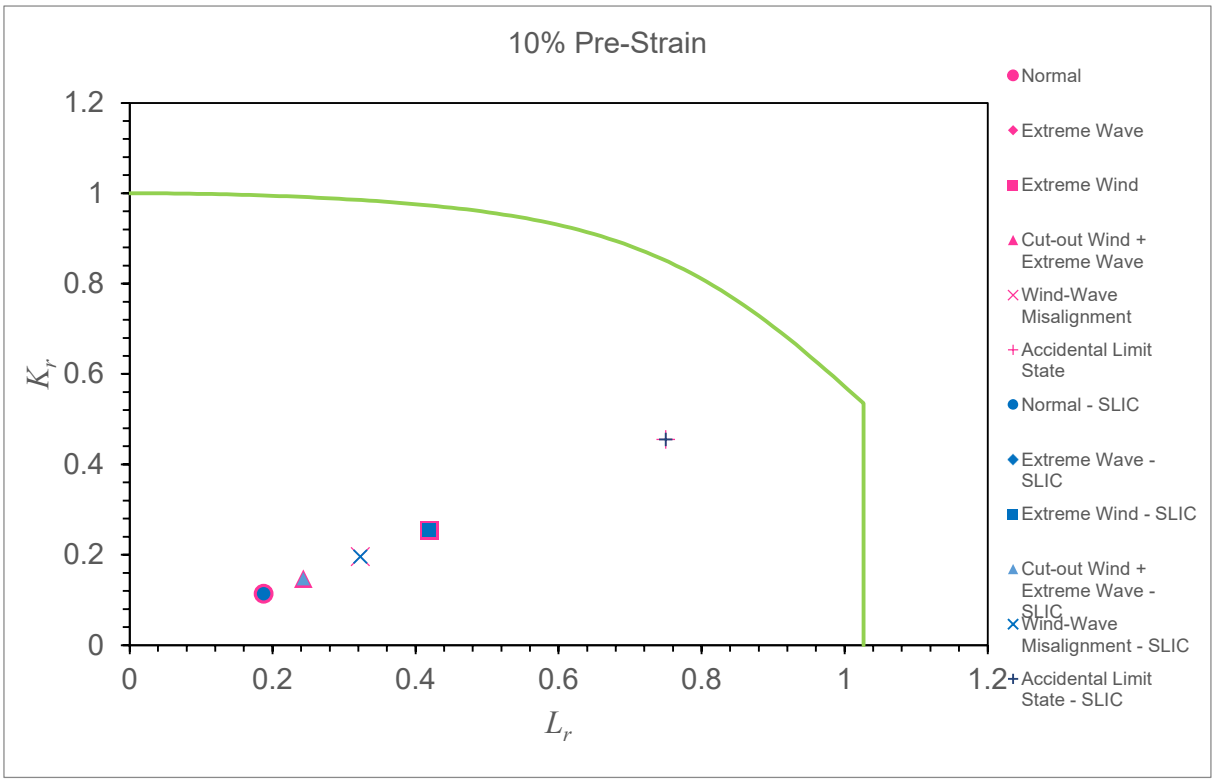

Figure 54 - Through thickness FAD for 10% pre-straining condition for present study and SLIC data

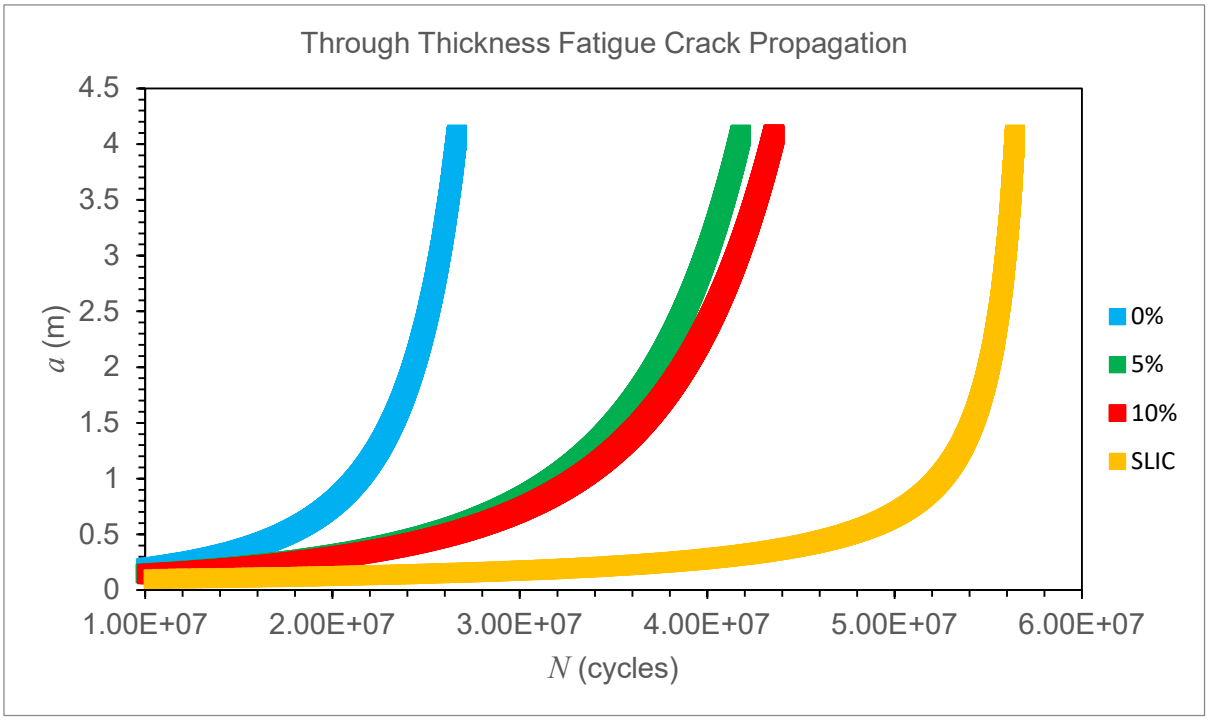

Figure 55 – Fatigue crack propagation curves for all levels of pre-straining vs SLIC data

From the analysis, it has been concluded that material pre-straining results in a decrease in fracture toughness, and thus there is a noticeable impact on integrity. With pre-straining, the duration for a fatigue crack to propagate to the limits will shorten, as illustrated by Table 18. This impact on integrity suggests that in the presence of a known flaw, the fatigue crack growth rate will override the predicted fatigue lifetime. Thus, regular inspection intervals are crucial to the structural integrity of monopile structures, with an emphasis on identifying the presence of a flaw as early as possible to avoid catastrophic failure.

6.4 Discussion

A key parameter in the calculation of stress intensity factor is the shape function, which can vary due to the wide range of solutions for elliptical and semi-elliptical cracks. The shape function suggested by Newman and Raju (16) is proposed for semi-elliptical cracked geometries under tensile stress, and takes the following form:

$$K = \sigma_t \sqrt{\frac{\pi a}{Q}} F\left(\frac{a}{t}, \frac{a}{c}, \frac{c}{b}, \Phi\right)$$

Equation 46 – Newman and Raju proposed shape function

$$Q = 1 + 1.464\left(\frac{a}{c}\right)^{1.65} \; for \; \left(\frac{a}{c} \leq 1\right)$$

Equation 47 – Calculation of Q

$$F = \left[M_1 + M_2\left(\frac{a}{t}\right)^2 + M_3\left(\frac{a}{t}\right)^4\right] g f_\Phi f_w$$

Equation 48 – Calculation of F

Where;

$$M_1 = 1.13 - 1.09\left(\frac{a}{c}\right)$$

$$M_2 = -0.54 + \frac{0.89}{0.2 + \left(\frac{a}{c}\right)}$$

$$M_3 = 0.5 - \frac{1.0}{0.65 + \left(\frac{a}{c}\right)} + 14(1.0 - \frac{a}{c})^{24}$$

Equation 49 – Calculation of parameters for F (16)

Where a is the crack depth, *c* is the half crack length, *t* is the plate thickness, *b* is the half width of the plate and *Φ* is the circular crack tip angle inside the semi-ellipse. This is the solution outlined in BS7910, where it is stated that flat plate solutions can be employed for circumferential external flaws in cylinders (9).

However, a paper by Bocher et. Al (17), suggests that in the case of offshore wind monopile structures, the Newman and Raju shape functions may be outdated, and instead the following equations were derived using finite element simulations:

$$Y = A\left(\frac{a}{c}\right)^2 + B\left(\frac{a}{c}\right) + C$$

$$A = -0.17622\left(\frac{a}{t}\right)^2 + 1.32106\left(\frac{a}{t}\right) - 0.02133$$

$$B = 0.54961\left(\frac{a}{t}\right)^2 - 2.76865\left(\frac{a}{t}\right) - 0.28716$$

Equation 50 – Shape function proposed by Bocher et al

$$C = -0.3833\left(\frac{a}{t}\right)^2 + 1.50500\left(\frac{a}{t}\right) + 0.96933$$

However, the proposed update for monopile structures comes with its limitation. The Bocher et al shape function is only valid for monopiles where $R_{out}/t \geq 20$, $0.2 \leq a/t \leq 0.8$, and $0.4 \leq a/c \leq 1.0$. In the current case study, this equation would not be valid, as a/t exceeds 1.0, as through thickness crack propagation FAD ensures the crack is the same length as the thickness of the monopile. Due to the large radius of curvature, a flat plate solution has been considered for this case study. However, the Newman and Raju shape functions have shown inaccuracies in this particular application. For example, Figure 56 shows a comparison of crack growth estimation for as received material in seawater, using a shape function of $Y = 1$, Newman and Raju for hollow cylinder, Newman and Raju for finite plate in tension and the new empirical equation for monopiles. From the figure, it is apparent that the new empirical shape function curve lies in between the two proposed by Newman and Raju. An assumption of $Y=1$ shows faster crack growth rates and may be assumed to be conservative.

The values from Newman and Raju for finite plate under tension can be seen to slightly underestimate the number of cycles in comparison to the new empirical shape function, and in the case of small diameter hollow cylinders this could be a difference of 10% overestimation. In the context of this case study, $Y = 1$ has been assumed for the through thickness crack propagation. Crackwise 6, which has been utilised to calculate the surface cracking in stage one FAD, employs the Newman and Raju equations as standard, and for much more accurate results, it may be suggested that in the case of monopiles the shape function should be updated for better accuracy of results (17).

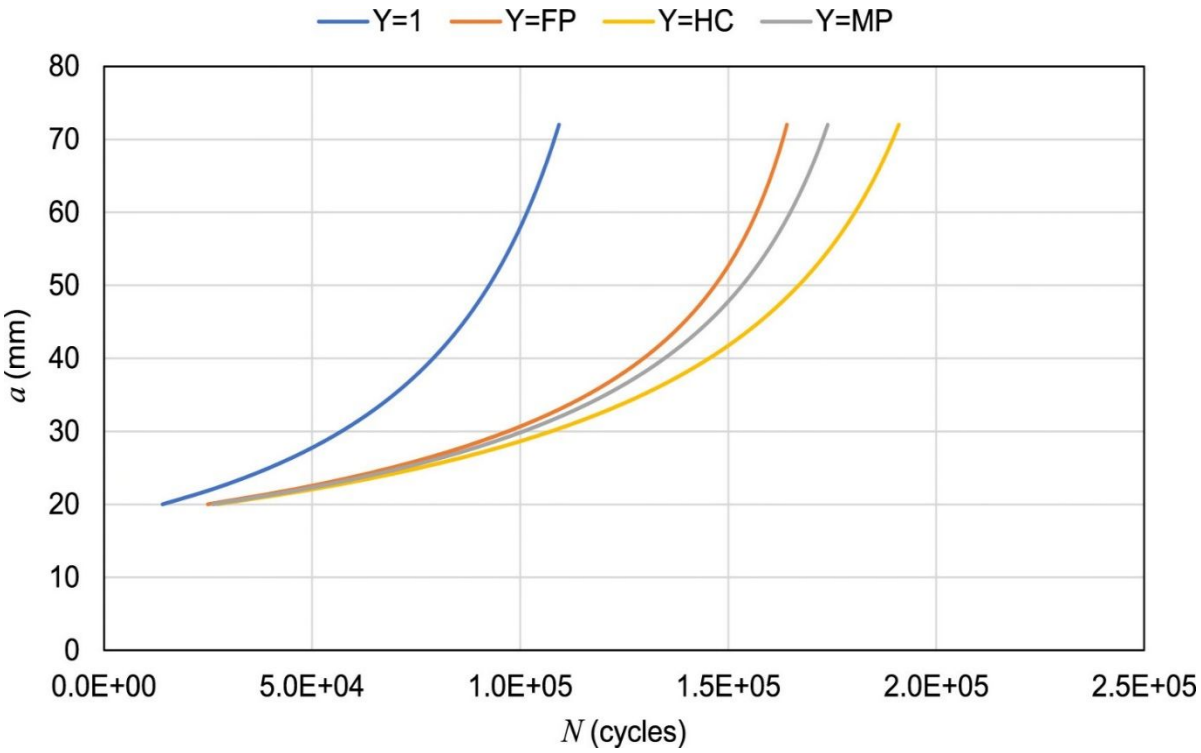

Figure 56 - Comparison of fatigue crack growth curves given by Bocher et al (17)

It is to be noted that all calculations have been conducted for free corrosion conditions. This is to provide a conservative assessment, and to cater for the fact that the SLIC interlaboratory testing was conducted in free corrosion conditions, and thus make a fair and comparable assessment. However, in reality, cathodic protection systems are typically used to protect the structure from corrosion. Using BS7910 Paris law constant values for cathodic protection, the following remaining useful life estimations were calculated for through thickness cracks at pre-straining conditions of 0%, 5% and 10%, at accidental limit state, for an R ratio of 0.1 (Table 21). The same methodology for fatigue crack growth calculations was applied as mentioned before, with an initial crack length of 80mm with a limit of 25% of the monopile circumference applied. The significant difference in remaining useful life between those calculated in free corrosion conditions and those calculated in cathodic protection conditions can be attributed to the fact that it is expected that a corrosive environment would significantly accelerate the rate of fatigue crack growth, which is reflected by their respective Paris constants.

Table 21 - Remaining useful life estimation of cracks after accidental limit state with cathodic protection

Pre-strain %	Fatigue Life (years)
0	88.5
5	87.3
10	85.7

From the table, the remaining life estimation for monopiles with cathodic protection are less than half the design lifetime of 250 years by utilising cathodic protection. Additionally, from real life scenarios it has been noted that cathodic protection systems are affected by factors such as tidal, current, wave height and storm frequency, salinity, temperature, dissolved oxygen, suspended solids, marine growth, and bed conditions, which can affect the cathode current density and current output thus affecting the efficacy of such systems (18). Due to these issues, it may be advisable to pay more attention to the worst case scenario, which is free corrosion when devising inspection and maintenance plans.

As SLIC interlaboratory testing was only conducted on base metal, additional tests would need to be carried out on pre-strained S355 samples in free-corrosion conditions, to determine if there could be any further impact of the structural integrity of offshore wind monopiles in seawater due to the effects of material pre-straining.

6.5 Conclusions

Failure assessment diagrams and fatigue crack growth rates were constructed and calculated using experimental fatigue crack growth, fracture toughness and tensile data from the present study over pre-strains of 0%, 5% and 10%. An environmental reduction factor (ERF) of 2 was incorporated into calculations to account for the fact tests were conducted in air and were to be compared to studies conducted in seawater free corrosion conditions from SLIC interlaboratory tests. Failure assessment diagrams were presented in two stages: from surface crack to through thickness, and from through thickness crack to maximum flaw size (with an upper limit of 25% of the monopile circumference). In stage one failure assessment diagrams, it can be seen for all pre-straining levels the data points using present study results with ERF lie much closer to the failure assessment line compared to those from the SLIC project, thus present study results with the experimental

reduction factor are more conservative. However, the gap between the present study and SLIC data points close as the pre-straining level increases. An increase in material pre-straining results in an increase in duration for the crack to propagate through the thickness and thus there is an increase in expected duration. For stage two failure assessment, it is interesting to note that the maximum allowable flaw differs with each loading condition. Another interesting point to note is that as material pre-straining increases, the maximum flaw size will decrease, with a shortening in duration for fatigue crack propagation. Thus, regular inspection intervals are crucial to the structural integrity of monopile structures, with an emphasis on identifying the presence of a flaw as early as possible to avoid catastrophic failure.

6.6 Acknowledgements

This work was supported by grant EP/L016303/1 for Cranfield, Oxford and Strathclyde Universities, Centre for Doctoral Training in Renewable Energy Marine Structures - REMS (http://www.rems-cdt.ac.uk/) from the UK Engineering and Physical Sciences Research Council (EPSRC).

6.7 References

1. Lie ST, Yang ZM, Gho WM. Validation of BS7910:2005 failure assessment diagrams for cracked square hollow section T-, Y- and K-joints. International Journal of Pressure Vessels and Piping [Internet]. 2009;86(5):335–44. Available from: http://dx.doi.org/10.1016/j.ijpvp.2008.11.015

2. DNVGL. Support structures for wind turbines. Dnvgl-St-0126 [Internet]. 2018;(July):208. Available from: https://rules.dnvgl.com/docs/pdf/DNVGL/ST/2018-07/DNVGL-ST-0126.pdf

3. Stutzmann J, Ziegler L, Muskulus M. Fatigue Crack Detection for Lifetime Extension of Monopile-based Offshore Wind Turbines. Energy Procedia [Internet]. 2017;137:143–51. Available from: https://doi.org/10.1016/j.egypro.2017.10.341

4. Lie ST, Yang ZM. BS7910: 2005 failure assessment diagram (FAD) on cracked circular hollow section (CHS) welded joints. 5th International Conference on Advances in Steel Structures, ICASS 2007. 2007;3(4):527–32.

5. Dowling AR, Townley CHA. The effect of defects on structural failure. A two-criteria approach. International Journal of Pressure Vessels and Piping. 1975;3(2):77–107.

6. Fajuyigbe A, Brennan F. Fitness-for-purpose assessment of cracked offshore wind turbine monopile. Marine Structures [Internet]. 2021;77(November 2020):102965. Available from: https://doi.org/10.1016/j.marstruc.2021.102965

7. Anderson TL, Osage DA. API 579: A comprehensive fitness-for-service guide. International Journal of Pressure Vessels and Piping. 2000;77(14–15):953–63.

8. Wiesner CS, Maddox SJ, Xu W, Webster GA, Burdekin FM, Andrews RM, et al. Engineering critical analyses to BS 7910 - in UK guide on methods for assessing the acceptability of flaws in metallic structures. International Journal of Pressure Vessels and Piping. 2000;77(14–15):883–93.

9. BS 7910. BSI Standards Publication Guide to methods for assessing the acceptability of flaws in metallic structures. BSI Standards Publication. 2015;(UK):490.

10. Darcis P, Santarosa D, Recho N, Lassen T. A fracture mechanics approach for the crack growth in welded joints with reference to BS 7910. European Conference on Fracture 15 - Advanced Fracture Mechanics for Life and Safety Assessments. 2004;(August):1–8.

11. Arany L, Bhattacharya S, Macdonald J, Hogan SJ. Design of monopiles for offshore wind turbines in 10 steps. Soil Dynamics and Earthquake Engineering. 2017;92:126–52.

12. ORE Catapult. Offshore Wind Farm Substructure Monitoring and Inspection Operations and Maintenance. 2017;(June):1–31.

13. Mehmanparast A, Brennan F, Tavares I. Fatigue crack growth rates for offshore wind monopile weldments in air and seawater: {SLIC} inter-laboratory test results. Materials & Design [Internet]. 2017 Jan;114:494–504. Available from: https://doi.org/10.1016%2Fj.matdes.2016.10.070

14. HSE. OTO-99058 a - Fatigue design curves for welded joints in air & seawater under variable amplitude loading. 2000.

15. Brandi R, Rossetto P. Fatigue design of offshore structures. Welding International. 1987;1(12):1155–61.

16. Raju JC, Newman IS. Stress Intensity factor Equations for Cracks in Three-Dimensional bodies Subjected to Tension and Bending Loads. NASA Technical memorandum. 1984;(May).

17. Bocher M, Mehmanparast A, Braithwaite J, Shafiee M. New shape function solutions for fracture mechanics analysis of offshore wind turbine monopile foundations. Ocean Engineering. 2018;160(May):264–75.

18. Wyatt B. Offshore windfarm monopile cathodic protection: Deficiencies in standards & specifications. European Corrosion Congress, EUROCORR 2015. 2015;2:1306–20.

7. Discussion and Future Work

7.1 Discussion

Defect assessment is a critical aspect of the operation and maintenance of structures in a wide range of industries, including the oil and gas, renewables, and nuclear industries. For example, in the pipeline industry, pipelines are usually assessed against quality control limits, which may seem arbitrary at the time of assessment, but may propagate into much larger defects. It is at this point that it is critical to carry out a "fitness for purpose" assessment to determine the best course of action (1). In the case of oil and gas pipelines, corrosion, dents, cracking, and weld defects are major issues, and thus over the past few decades a large body of work surrounding these topics have been undertaken (2). Fracture mechanics principles are the basis of the general procedures, and the guidelines commonly followed are BS7910 and API 579. The steps for failure assessment are typically (3):

1. Definition and categorisation of all loads and stresses, with the most arduous loading conditions being evaluated
2. Determination of tensile properties of material
3. Selection of appropriate failure assessment diagram
4. Flaw characterisation (shape)
5. Selection of analysis category
6. Fracture toughness definition
7. Flaw size specifications
8. Calculation of L_r
9. Calculation of K_r
10. Plotting failure assessment data on diagram
11. Calculate fatigue crack growth of flaw during service
12. Determine significance of results
13. Make necessary changes/refinements

It is to be understood that BS7910 has been developed primarily for application in industries such as oil and gas, where the relevant structures under integrity assessment are structures such as pipelines carrying crude oil. In the case of offshore wind monopile structures, the context is different and thus the priorities of the inspection will differ. For example, in the oil and gas industry, a through thickness crack would likely result in a

leak in the pipeline. Therefore, the second FAD assessment of calculating the maximum through thickness crack length before the structure collapses, would be irrelevant. In the case of jacket structures, leak before detection systems are in place to alert engineers that a through thickness crack has taken place. However, in the case of offshore wind monopile structures, such leak detection systems cease to exist. The introduction of such leak detection systems similar to those employed for jacket structures may be of importance for the structural integrity of monopile structures.

Development of shape function solutions for through thickness crack propagation can help ensure more accurate failure assessment estimations. Currently, although there are many shape function solutions available, BS7910 recommends the use of Newman and Raju shape functions (4). However, more current works suggest that the use of this shape function in the application of monopile structures may be outdated. New updated shape functions for use in offshore wind monopile structures have been suggested by Bocher et al (5), however, these shape functions come with limitations. The Bocher et al shape function is only valid for monopiles where $R_{out}/t \geq 20$, $0.2 \leq a/t \leq 0.8$, and $0.4 \leq a/c \leq 1.0$. These may be suitable for use in calculation of stage one FAD, however, for through thickness crack FAD this is unsuitable. Further work would need to be conducted to develop shape function solutions for $a/t = 1.0$. Comparisons between Newman and Raju and the new proposed shape functions show that Newman and Raju appear to produce conservative results. Due to the use of Newman and Raju shape functions for the FAD analysis in this study, it can be agreed that the results in this study may be conservative (faster crack growth rates) to a certain degree. This may be due to the fact that for small cracks it may be fair to consider an infinite flat plate, however when crack sizes increase this becomes scale dependent. Flat plates are geometrically different to curved plates, and thus a difference in shape factor is to be expected. However, for convenience, a flat plate is usually assumed.

In a paper by Fajuyigbe and Brennan, further issues with the failure assessment approach outlined in BS7910 have been highlighted. From the results, it was observed that crack depths over 80% of the monopile thickness gave overly conservative L_r values, with over estimations for K_r values. This suggests that certain flaws may be deemed as unacceptable by the BS7910 failure assessment method, when, in fact, there may still be a reasonable amount of fatigue life present. Although in thinner walled monopile structures this may

not prove much of an issue, as the trend is leaning towards larger and thicker monopile structures this difference can prove significant (6).

A limiting crack size of 25% of the monopile circumference has been taken as the maximum critical flaw size for through thickness cracks. Comparisons to critical crack sizes predicted by the FAD method have shown that this estimate may be lower than the critical crack length. For example, for a monopile in “normal” operating conditions, the critical crack length can be 7.12m. However, using the 25% circumference “rule”, this critical crack length is reduced to 4.08m. This figure is almost half the calculated estimate, and thus can be said to be extremely conservative. It can be argued that in “normal” operating conditions, the proposed inspection plan may not be cost efficient. However, in the case of more extreme conditions, the same limiting crack size is under-conservative, with limiting crack sizes in certain cases being just over 1m. It is therefore of extreme importance to understand the wave and wind loading conditions of the environment properly, as this can have significant impact on the critical crack lengths, as well as the inspection and maintenance schedule, affecting the overall cost of energy.

For this study, free corrosion conditions have been assumed. However, in its application appropriate cathodic protection systems would be installed to ensure the structural integrity of the monopile system. Free corrosion conditions have been assumed to identify the worst-case scenario. Comparisons of data from the present study with the environmental correction factor to the fatigue crack growth predictions for free corrosion from BS7910 for through thickness conditions suggest that BS7910 may not be conservative enough for offshore wind monopiles (Figure 57). This may be due to the fact that BS7910 is widely used for structures of much thinner wall thicknesses such as pipes or jacket braces. Therefore, the standard may need to be updated for thicker wall thicknesses such as those found in offshore wind monopile structures.

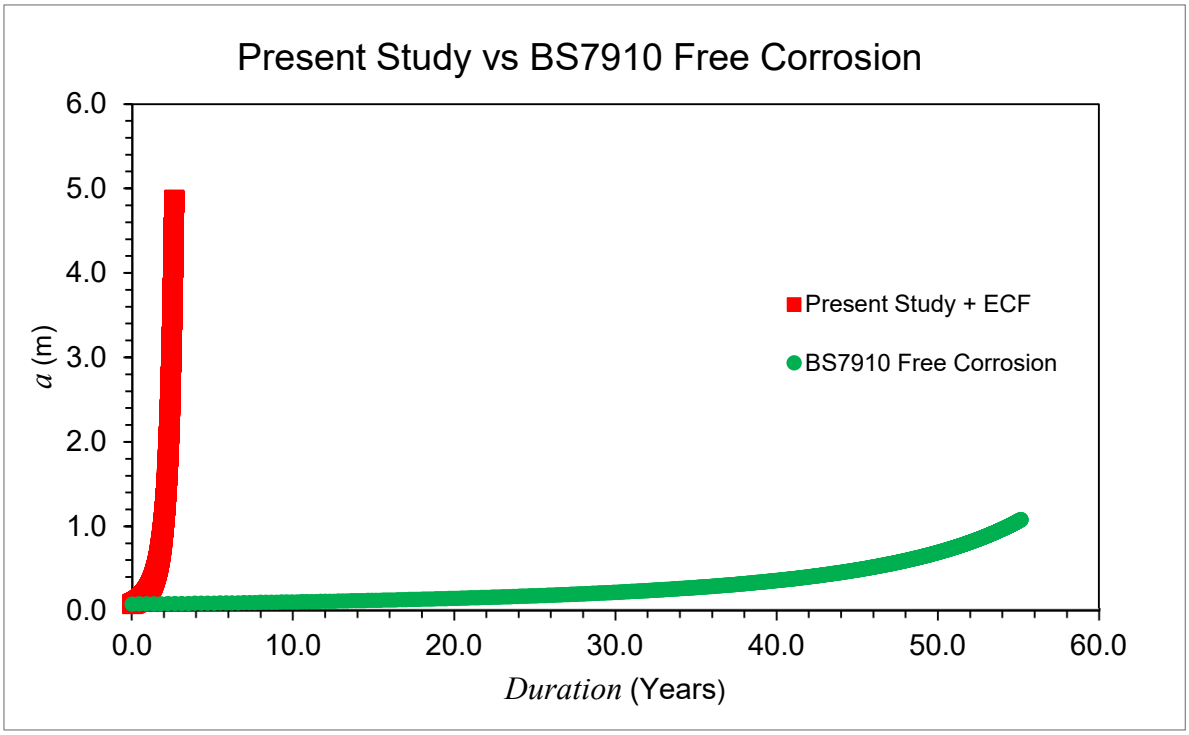

Figure 57 – comparison of fatigue crack growth rates from present study to those suggested in BS7910 for free corrosion

DNV GL for Support structures for wind turbine structures suggests that intervals between inspections should not exceed one year, with longer intervals acceptable for less critical components. However, it is suggested that the entire wind farm should undergo at least one inspection over a five-year period, and inspection intervals can be modified based on the findings. However, annual fatigue crack inspection may be waived depending on the accessibility for inspection and repair, provided the correct safety factors have been applied during engineering design (7). However, this recommendation may be problematic on reflection, from the results of this study. As previously discussed, fatigue cracks may be initiated from cable entry holes, with cracks propagating from the edge, to the surface through the thickness. As inspection around the edges of cable entry holes may prove difficult due to components such as flanges etc in the way, it should not be recommended to completely waive any inspection practice. It would be recommended that inspection around the circumference from the cable entry holes are conducted, however, from the analysis in the failure assessment chapter, it can be advised that initial cracks may not be of immediate importance. However, once cracks have propagated through the thickness, they may be much more visible, and thus it is important to intervene as early as possible. From the results it has been seen that even in free corrosion conditions

it may take years for the cracks to reach their maximum limits. Therefore, an overall defect assessment of offshore wind monopile structures should be conducted at least annually.

For large structures such as monopiles, operation management contributes massively to life cycle costs, due to the number of inspections or maintenance strategies put in place to avoid unscheduled interventions. DNV-OS-J101 recommends the following formula to calculate inspection intervals (8)(9):

$$Inspection\ interval = calculated\ fatigue\ life * \frac{{\gamma_m}^5}{1.25^5}$$

When:

γ_m
$= 1.25, no\ check\ for\ fatigue\ cracks\ is\ needed, corresponding\ to\ an\ assumption$

$$of\ no\ access\ to\ the\ structural\ detail$$

γ_m
$= 1.15, inspections\ for\ fatigue\ cracks\ necessary\ every\ 13\ years\ (if\ design\ life\ is\ 20\ years)$

γ_m
$= 1.0, inspections\ for\ fatigue\ cracks\ necessary\ every\ 7\ years\ (if\ design\ life\ is\ 20\ years)$

Therefore, overdesign of monopiles can reduce maintenance costs, but this saving may be offset by the cost of the extra volume of S355 used in monopile cans. However, relating back to the case study using the Thames Estuary met ocean data in chapter 8, the worst-case inspection intervals of 7 years may not be soon enough, especially in free corrosion conditions (in the worst-case scenario of inefficient cathodic protection systems). To achieve inspection intervals of 7 years, the base price of steel would need to be reduced from £690/ton to £100/ton to break even, and even further down to £80/ton to achieve zero inspection intervals (8). When material pre-straining occurs in S355 steel, the tensile properties are seen to increase – with yield stress being one of the major changes with increasing pre-straining. It may be possible that while designing offshore wind monopile structures, that thinner wall thicknesses can be employed due to the increase in material strength. This difference in wall thickness would therefore decrease the overall material

costs of monopiles, and thus reduce the maintenance costs of wind farms, thus reducing the overall cost of energy.

From Figure 58, it can be seen that for 5% pre-strain, it takes just under 3 years for a fatigue crack to propagate to its maximum through thickness flaw size in “normal” conditions. However, for limit states such as extreme wind, the maximum flaw size is much smaller, at around 1.32m. Reading from the figure, this would take around 1.5 years to reach this maximum flaw size, thus an inspection interval of 5 years would be much too short. In the case of normal operating conditions, DNV suggests an inspection interval of 7 years for a fatigue design factor of 1. Even in this case, it would be too late as it would take under 3 years to reach the critical crack length. For surface cracks, it takes approximately 2 and a half years to propagate to this level, so it is entirely possible for a catastrophic failure to have occurred before the first inspection interval itself. As the figure shows exponential growth of through thickness cracks especially after year 2, it may be a suggestion to revise inspection intervals from 7 years to 4 years to avoid sudden failure. It would also be advised to annually inspect the crack, if no intervention has taken place before then, but it would be advised to wait no longer than a year to avoid disastrous consequences.

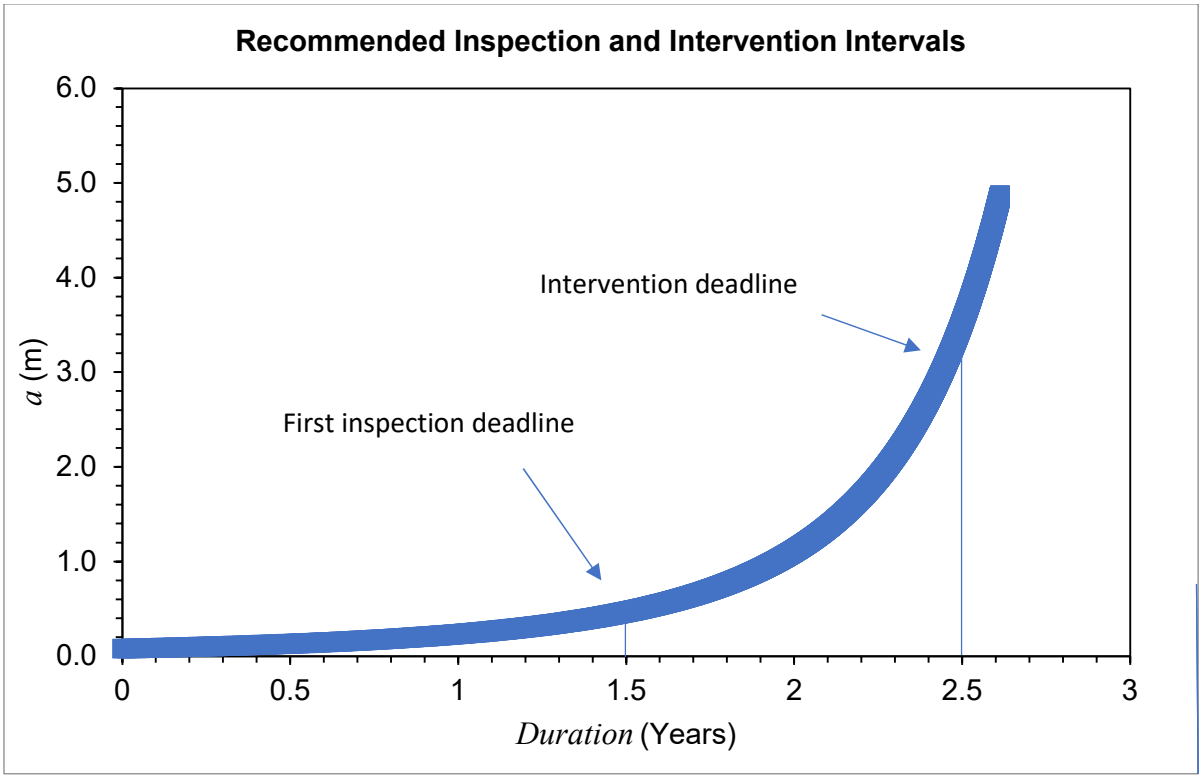

Figure 58 – Suggested minimum inspection intervals for 5% pre-strain monopile structures

7.2 Future work

While S-N curves for 0% and 5% pre-strained S355 have been derived, further work needs to be undertaken to produce the complete set of S-N curves for 10% pre-straining condition. In addition, further data points for all S-N curves would be of benefit, to ensure extra confidence in the S-N curves, as the S-N curves presented in this study may be considered indicative rather than final. Figure 59 shows comparisons of the S-N data from this study to the mean and design curves from DNV. From comparisons it appears that the codes and standards allow room for error in their predictions, compared to the results found in this study.

Normalised S-N curves of the experimental test results from the present study have been produced in Figure 60. Experimental test data was normalised by calculating the factor of applied stress divided by the material's yield stress. After normalisation, it can be seen that the S-N curves for 0% and 5% exhibit a change in slope regardless of the stress level, with the slope of the S-N curve in the high stress region above yield being the same as the intermediate stress regions below yield.

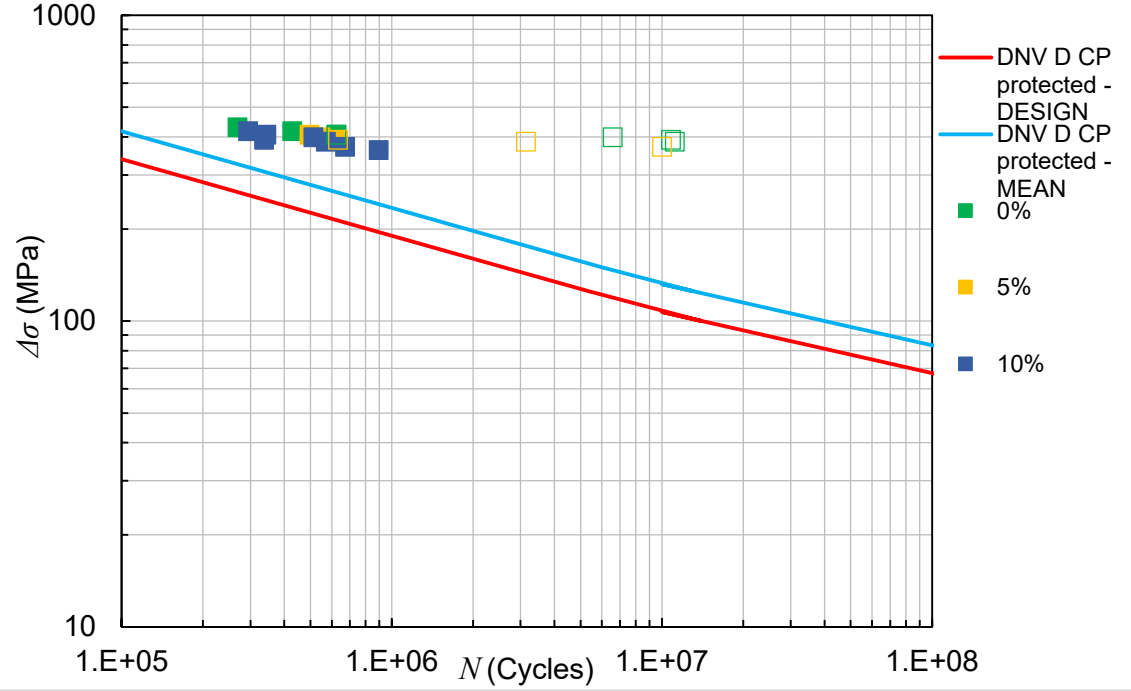

Figure 59 – Comparison of experimental S-N curves to codes and standards

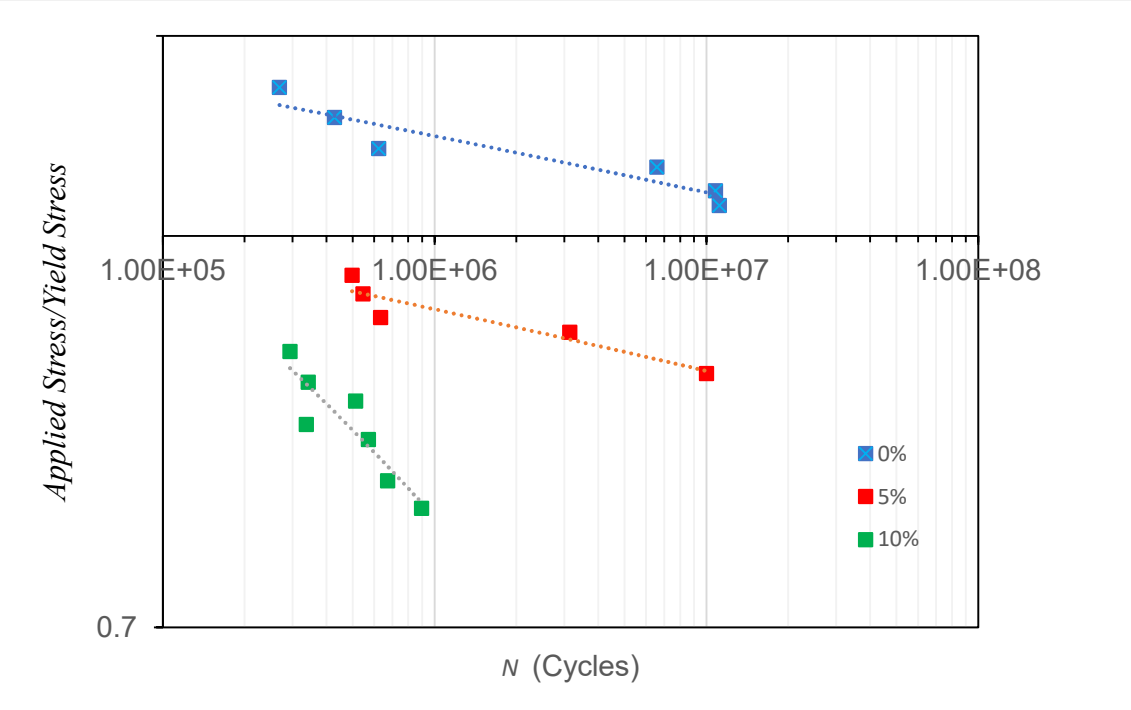

Figure 60 - Normalised S-N curves for present study experimental test data

In the failure assessment chapter, an environmental reduction factor of 2 was applied to the test results from the present study to make direct comparisons with test results in free corrosion seawater conditions cited in literature. However, it is unknown if material pre-straining would impact this environmental correction factor suggested by SLIC.

Therefore, for much more accurate structural integrity assessment, it would be of significant importance to conduct an experimental programme looking into the effects of material pre-straining on the fatigue crack growth rates of S355 in seawater conditions.

As this research has looked at the worst case and relevant scenario, pre-tensioning has been the only condition that has been considered. As chapter 5 suggests, material pre-straining through the thickness will differ, from compressive pre-strains on the inner surface of the monopile, to tensile pre-strains on the external surface of the monopile. As this is the surface subject to wave and wind loading, this was the condition under consideration as it may be more relevant to the external surface defects of monopiles. But to create a full picture of the behaviour of a monopile, both external and internal monopile surfaces must be considered. Therefore, an experimental test programme should be devised to investigate the effects of pre-compression on S355, and how that may impact the monopile behaviour.

In chapter 5, a finite element model to determine the effects of various fabrication factors on the monopile forming process was developed. From the findings of this thesis, it has been concluded that material pre-straining increases the yield stress, decreases the engineering strain at failure, decreases the fatigue life and fracture toughness while the fatigue crack growth behaviour is largely unchanged. Depending on the specific needs of the manufacturer, this model can be used to modify the monopile behaviour. The finite element model used for this study was limited to a certain range of loading (up to 900kN), on a 60mm thickness plate. Overall, it would appear that keeping the level of material pre-straining minimal would be beneficial to the structural integrity of the monopile, however in design calculations a higher yield stress may be preferable. The exact load levels for forming of offshore wind monopile cans are unknown, as this information is highly confidential, and so it is difficult to fully predict what the exact levels of pre-straining may be, posing further limitations. However, equipped with the findings of this paper, fabricators in possession of this information can make much more informed decisions on how the applied load levels, friction, distance between rollers etc can impact the overall behaviour of the monopile can. Creation of a database allowing fabricators and engineers access to predicted values of fracture toughness, S-N fatigue, fatigue crack growth and tensile properties over a wide range of pre-straining conditions can enable

much more informed decisions, allowing overall savings in terms of maintenance and inspection of offshore wind monopiles.

Comparisons of the upper bound fatigue crack growth trends on 0%, 5% and 10% pre-strained S355 have been compared with recommended fatigue crack growth trends for base metal in BS7910. It has been observed that the present study data when corrected for free corrosion gives crack growth rates that are faster than those recommended in BS7910. Further work should be undertaken to examine the fatigue crack growth rates in pre-compressed S355 material with the crack growth trends recommended in BS7910. The correction to free corrosion environment was achieved by application of the environmental reduction factor recommended in SLIC to mimic the impact of seawater on test results. Comparisons of test results from the present study with the applied correction factor to seawater test data produced by the SLIC project showed differences in fatigue crack growth predictions. The absence of fatigue crack growth rates for pre-straining in seawater, due to time and availability constraints, may pose the possibility that the results from the fitness for service assessment may be over predictive.

Using the Equation 38 J_{IC} values can be predicted using the finite element model for fabrication of offshore wind monopiles.

$$J_{IC} = -0.0145\varepsilon_p + 0.8618$$

Equation 51 – Empirical equation correlating J_{IC} with plastic strain for S355G10+M

These values can then be plugged into further FAD assessments for defect assessment. However, further work needs to be conducted with a wider range of experimental data including tensile and compressive pre-strains to ensure the equation is an accurate relationship between J_{IC} and plastic strain. A wider range of experimental test results were not possible during the duration of this project due to time constraints. From Figure 31 it can be seen that a higher yield stress relates to a higher J_{IC} value, and it may be beneficial to conduct a range of fracture toughness and tensile tests over a wider range of pre-straining levels to gain a more accurate correlation between the two. Future work would involve the potential development of a J_{IC} finite element prediction model to eradicate the necessity for further fracture toughness experiments.

7.3 References

1. Cosham A, Hopkins P. The pipeline defect assessment manual. Proceedings of the International Pipeline Conference, IPC. 2002;B(0):1565–81.

2. Cosham A, Hopkins P. The effect of dents in pipelines - Guidance in the pipeline defect assessment manual. International Journal of Pressure Vessels and Piping. 2004;81(2):127–39.

3. Milne I, Ainsworth RA, Dowling AR, Stewart AT. Assessment of the integrity of structures containing defects. International Journal of Pressure Vessels and Piping. 1988;32(1–4):3–104.

4. BS 7910. BSI Standards Publication Guide to methods for assessing the acceptability of flaws in metallic structures. BSI Standards Publication. 2015;(UK):490.

5. Bocher M, Mehmanparast A, Braithwaite J, Shafiee M. New shape function solutions for fracture mechanics analysis of offshore wind turbine monopile foundations. Ocean Engineering. 2018;160(May):264–75.

6. Fajuyigbe A, Brennan F. Fitness-for-purpose assessment of cracked offshore wind turbine monopile. Marine Structures [Internet]. 2021;77(November 2020):102965. Available from: https://doi.org/10.1016/j.marstruc.2021.102965

7. DNVGL. Support structures for wind turbines. Dnvgl-St-0126 [Internet]. 2018;(July):208. Available from: https://rules.dnvgl.com/docs/pdf/DNVGL/ST/2018-07/DNVGL-ST-0126.pdf

8. Ioannou A, Wang L, Brennan F. Design Implications towards Inspection Reduction of Large Scale Structures. Procedia CIRP. 2017;60:434–9.

9. Veritas DN. Design of Offshore Wind Turbine Structures October 2007. Computer. 2009;(November):1–142.

8. Conclusions and Contribution to Knowledge

8.1 Conclusions

An experimental programme involving mechanical, uniaxial fatigue, interrupted fatigue, fatigue crack growth and fracture toughness tests on S355GS+10 structural steel with 0%, 5% and 10% tensile pre-strain states has been conducted. From the test results, it was observed that the fatigue life of S355 significantly decreases with an increase in material pre-straining, especially at lower stress levels where there was over an order of magnitude reduction in fatigue life found in 10% pre-strained material. Tensile tests on interrupted fatigue specimens damaged at 50% and 80% of the total number of cycles to failure, showed that if the applied stress level is lower than the yield stress, the fatigue damage has fairly insignificant results on the material's mechanical behaviour. Material pre-straining had very little significant impact on the fatigue crack propagation of S355 in pre-tension. However, further work needs to be conducted to examine the effects of pre-compression on fatigue crack propagation behaviour.

Although S-N fatigue design curves produced in international standards provide a lower fatigue life prediction for steels, the recommended trends in BS7910 may tend to under-predict fatigue crack growth rates in as-received and pre-strained materials. Therefore, it is important to account for material pre-straining effects on fatigue design and life assessment of offshore structures with sufficient safety margins put in place against failure.

Fracture toughness tests were performed on structural steel samples which had material pre-strain introduced into them by performing interrupted tensile tests stopping at stress levels corresponding to 5% and 10% plastic strain at room temperature. From these samples, C(T) specimens were fabricated for use in room temperature fracture toughness tests. Fractography analysis concluded that the test set up was in good alignment, with good agreement between unloading compliance crack length estimations and actual crack length measurements. Analysis of P vs LLD plots from each pre-straining level was conducted and the results showed that as the peak load increased with pre-strain level, there was a decrease in load line displacement value. This is believed to be due to a decrease in ductility while the yield strength increases as a result of pre-straining. R-curves were produced, and it was observed that the J_{IC} fracture toughness can decrease

up to 15% compared to the parent material. Material hardening due to pre-straining can reduce the ability to absorb energy due to the increase dislocation density, thus a change in fracture toughness can be observed. Using the obtained results, an empirical formula was determined which correlated yield stress and fracture toughness values with pre-straining level for S355G10+M structural steel, and this formula could improve the structural integrity assessment of offshore wind monopile structures which are subject to plastic pre-straining during the fabrication process. Further investigation needs to be conducted to improve the life assessment of monopiles made of a wider range of structural steels and pre-straining levels.

Using the experimental test results, failure assessment diagrams were constructed, with fatigue crack growth durations calculated at 0%, 5% and 10% pre-strain. Incorporating an environmental reduction factor (ERF) of 2 to the crack growth calculations enabled a clear comparison of test results in air to test results in seawater. Failure assessment diagrams were presented in two stages; from surface crack to through thickness, and from through thickness crack to maximum flaw size (with an upper limit of 25% of the monopile circumference). In stage one failure assessment diagrams, it was seen for all pre-straining levels the data points using present study results from the present study with ERF lay much closer to the failure assessment line compared to those from the SLIC project, thus present study results with the experimental correction factor were concluded to be more conservative. However, the gap between the present study and SLIC data points became smaller as the pre-straining level increased. Increases in material pre-straining resulted in a slight increase in duration for the crack to propagate fully through the thickness. In stage two failure assessment, it was observed that the maximum flaw size changed with loading condition, and material pre-straining also decreased the maximum flaw size. Therefore, it can be concluded that regular inspection intervals are of extreme importance to the structural integrity of monopile structures, with early identification of flaws being of crucial importance in the avoidance of catastrophic failure.

Using finite element analysis, a parametric study was conducted to determine the effects of various fabrication and manufacturing process on the resulting plastic strain values of S355. For a plate of 60mm thickness, it was observed that a 500kN load produced minimal plastic strain, however a load of 900kN presented a plastic strain of 1.41%. Increasing the friction coefficient from 0.2 to 1.0 resulted in a decrease in plastic strain, with a roller

diameter decrease of 0.2m resulting in an increase in an increase in plastic strain. Increasing the roller diameter however had minimal effects on plastic strain levels. An increase in plate length resulted in an overall increase in plastic strain levels. However, the most significant change in plastic strain was obtained by changing the wall thickness. Reducing the wall thickness by 5mm resulted in a two-fold increase in plastic strain, while increasing the wall thickness reduced the plastic strain by over a magnitude of 2. Altering the wall thickness also affected radius of curvature at a load level of 900kN, with a 5mm increase in wall thickness halving the overall radius, and a 5mm decrease doubling in overall radius.

8.2 Contributions to Knowledge

Through the testing and analysis in this work it has been deduced that:

- Material pre-straining results in degradation of fracture toughness in S355G10+M structural steel.
- Fatigue damage does not largely affect the mechanical properties of S355G10+M.
- Material pre-straining affects the mechanical properties of S355G10+M with an increase in yield stress, ultimate tensile strength and decrease in engineering strain at failure observed.
- Fatigue crack growth rates are not significantly affected by material pre-straining.

In addition, the following contributions to knowledge were made:

- A finite element model was developed to determine the effects of various fabrication factors on the level of material pre-straining present in S355.
- Engineering critical assessments were undertaken to understand the effects of material pre-straining on the critical crack length and duration of time to achieve this, with comparisons being made to similar research conducted in the field.

Appendix A – Test Matrices

A.1 Finite Element Analysis Test Matrix

	Plate Thickness	Diameter/Curvature			Length of Plate			Distance Between Rollers			Rolling Force		
Plate Thickness		Case 1	Case 2	Case 3	Case 10	Case 11	Case 12	Case 19	Case 20	Case 21	Case 28	Case 29	Case 30
		Case 4	Case 5	Case 6	Case 13	Case 14	Case 15	Case 22	Case 23	Case 24	Case 31	Case 32	Case 33
		Case 7	Case 8	Case 9	Case 16	Case 17	Case 18	Case 25	Case 26	Case 27	Case 34	Case 35	Case 36
Diameter/Curvature					Case 37	Case 38	Case 39	Case 46	Case 47	Case 48	Case 55	Case 56	Case 57
					Case 40	Case 41	Case 42	Case 49	Case 50	Case 51	Case 58	Case 59	Case 60
					Case 43	Case 44	Case 45	Case 52	Case 53	Case 54	Case 61	Case 62	Case 63
Length of Plate								Case 64	Case 65	Case 66	Case 73	Case 74	Case 75
								Case 67	Case 68	Case 69	Case 76	Case 77	Case 78
								Case 70	Case 71	Case 72	Case 79	Case 80	Case 81
Distance Between rollers											Case 82	Case 83	Case 84
											Case 85	Case 86	Case 87
											Case 88	Case 89	Case 90
Rolling Force													

A.2 Experimental Test Matrix

2.1 As Received

Test Type	Test ID	Pre-Straining Condition (%)	Specimen Geometry
T	T-0%-1	AR	Dogbone
T	T-0%-2	AR	Dogbone
IT	IF-0%-0.5	AR	Dogbone
IT	IT-0%-0.8	AR	Dogbone
SN	0%-SN-1	AR	Dogbone
SN	0%-SN-2	AR	Dogbone
SN	0%-SN-3	AR	Dogbone
SN	0%-SN-4	AR	Dogbone
SN	0%-SN-5	AR	Dogbone
SN	0%-SN-6	AR	Dogbone
FCG	CT-0%-1	AR	C(T)
FCG	CT-0%-2	AR	C(T)
FCG	CT-0%-3	AR	C(T)
FT	JIC-0%-1	AR	C(T)
FT	JIC-0%-2	AR	C(T)
FT	JIC-0%-3	AR	C(T)

2.2 5% Pre-strain

Test Type	Test ID	Pre-Straining Condition (%)	Specimen Geometry
T	T-5%-1	5	Dogbone
T	T-5%-2	5	Dogbone
IT	IF-5%-0.5	5	Dogbone
IT	IT-5%-0.8	5	Dogbone
SN	5%-SN-1	5	Dogbone
SN	5%-SN-2	5	Dogbone
SN	5%-SN-3	5	Dogbone
SN	5%-SN-4	5	Dogbone
SN	5%-SN-5	5	Dogbone
FCG	CT-5%-1	5	C(T)
FCG	CT-5%-2	5	C(T)
FCG	CT-5%-3	5	C(T)
FCG	CT-5%-4	5	C(T)
FT	JIC-5%-1	5	C(T)
FT	JIC-5%-2	5	C(T)
FT	JIC-5%-3	5	C(T)
FT	JIC-5%-4	5	C(T)

2.3 10% Pre-strain

Test Type	Test ID	Pre-Straining Condition (%)	Specimen Geometry
T	T-10%-1	10	Dogbone
T	T-10%-2	10	Dogbone
IT	IF-10%-0.5	10	Dogbone
IT	IT-10%-0.8	10	Dogbone
SN	10%-SN-1	10	Dogbone
SN	10%-SN-2	10	Dogbone
SN	10%-SN-3	10	Dogbone
SN	10%-SN-4	10	Dogbone
SN	10%-SN-5	10	Dogbone
SN	10%-SN-6	10	Dogbone
SN	10%-SN-7	10	Dogbone
FCG	CT-10%-1	10	C(T)
FCG	CT-10%-2	10	C(T)
FCG	CT-10%-3	10	C(T)
FCG	CT-10%-4	10	C(T)
FT	JIC-10%-1	10	C(T)
FT	JIC-10%-2	10	C(T)
FT	JIC-10%-3	10	C(T)
FT	JIC-10%-4	10	C(T)

Appendix B - Specimen Extraction and Geometries

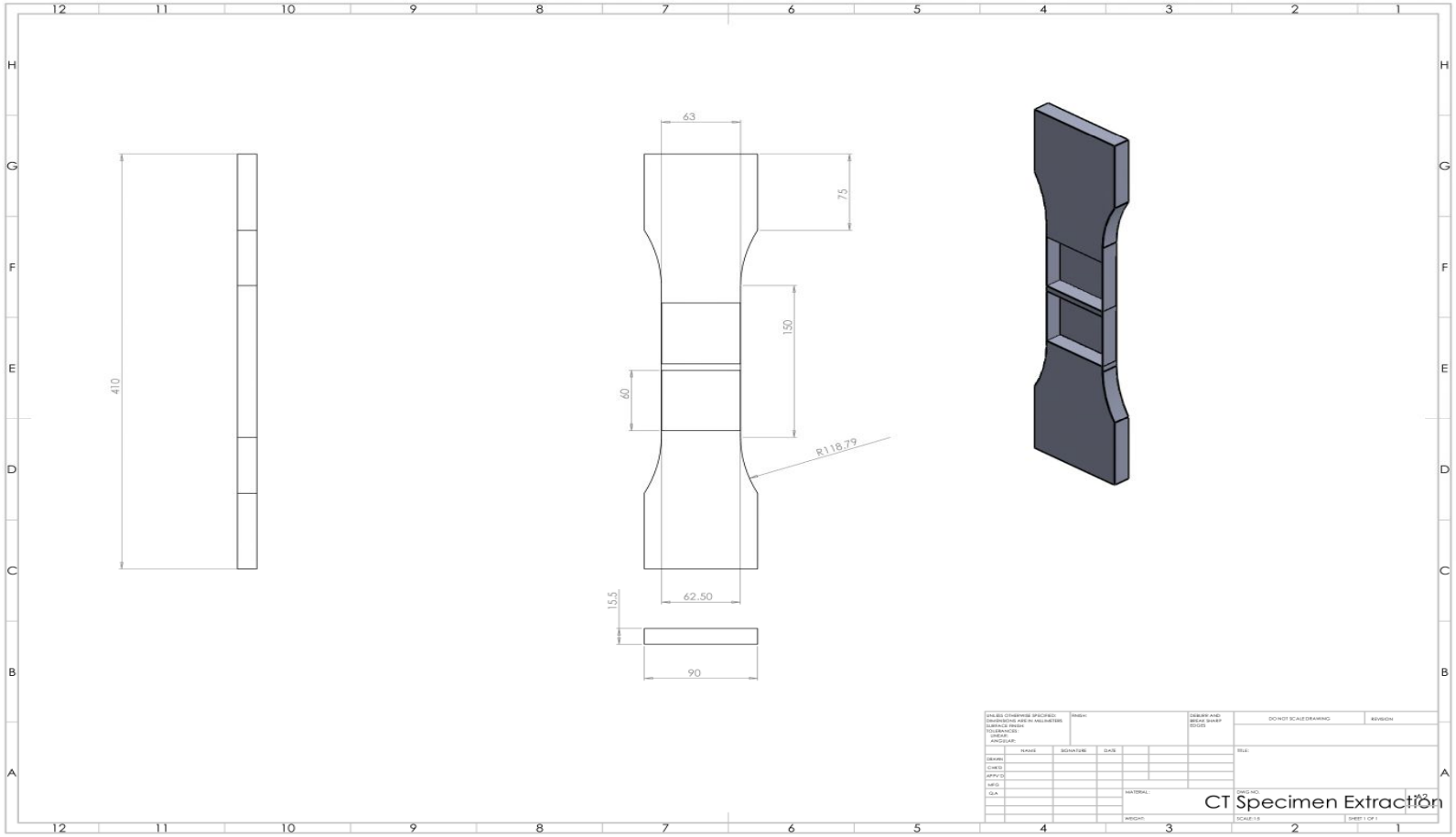

Figure 61 – Specimen extraction plan for C(T) specimens

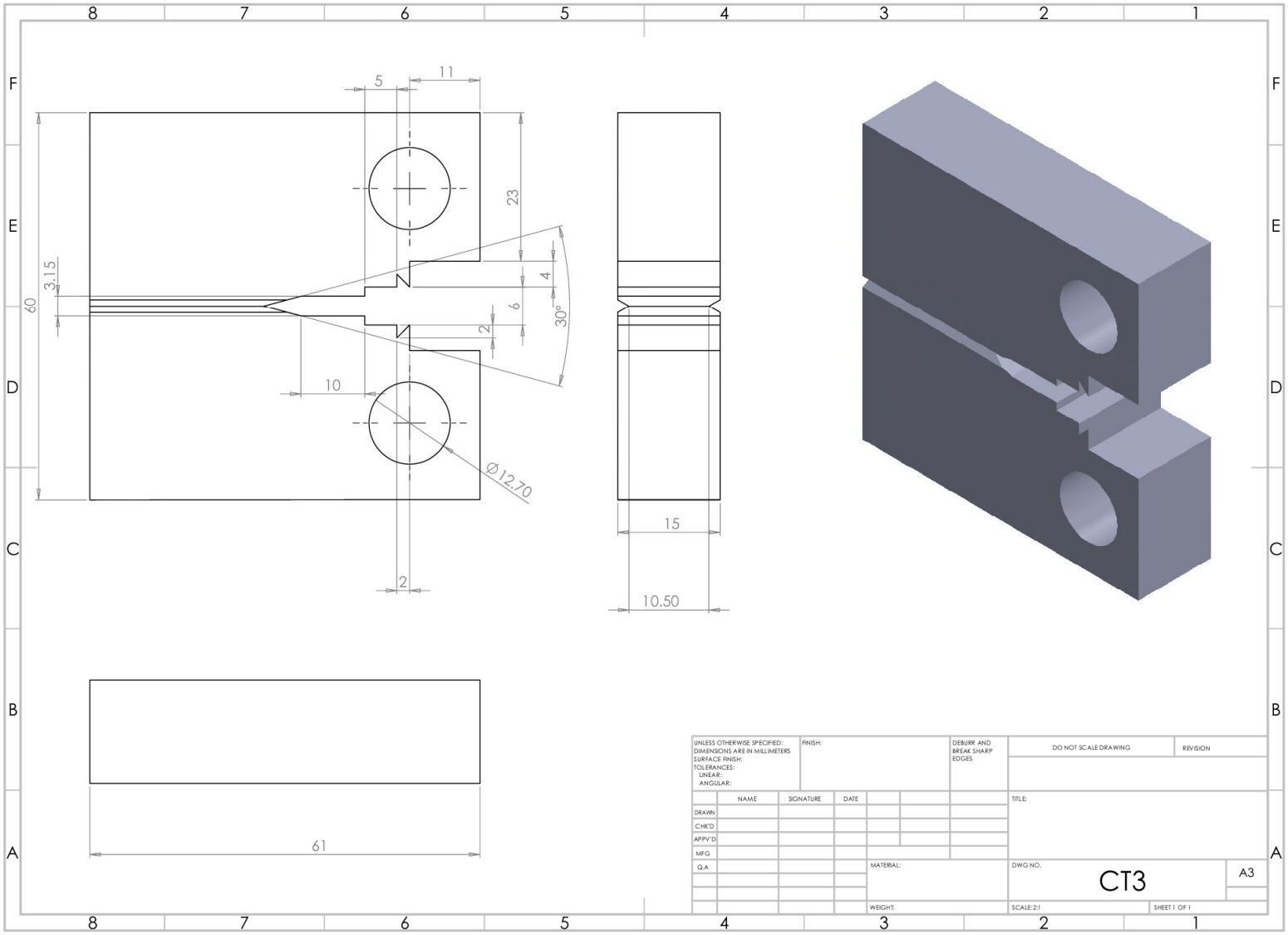
5
11
23
3.15
60
4
6
2
30°
10
Ø12.70
2
15
10.50
61
UNLESS OTHERWISE SPECIFIED:
DIMENSIONS ARE IN MILLIMETERS
SURFACE FINISH:
TOLERANCES:
LINEAR:
ANGULAR:
FINISH:
DEBURR AND BREAK SHARP EDGES
DO NOT SCALE DRAWING
REVISION
NAME
SIGNATURE
DATE
DRAWN
CHK'D
APPV'D
MFG
Q.A
MATERIAL:
WEIGHT:
TITLE:
DWG NO.
CT3
A3
SCALE:2:1
SHEET 1 OF 1

Figure 62 – C(T) Specimens used in fatigue crack growth and fracture toughness testing

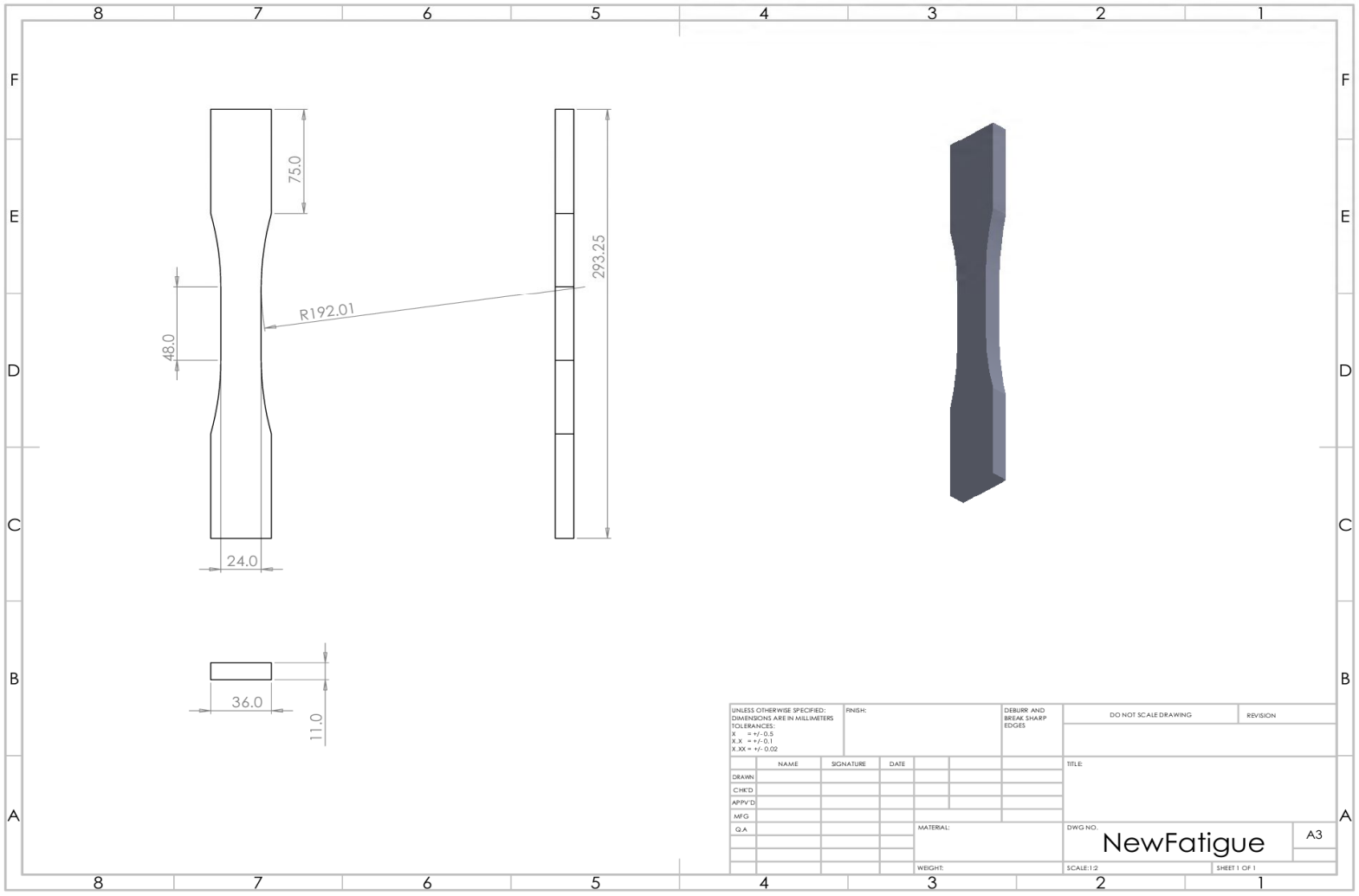

Figure 63 – Dogbone specimens used in S-N and tensile test

Appendix C – Fracture Toughness Testing

Experiments conducted on C(T) specimens with 25% side grooving resulted in a smaller than expected data set. Thus, the values from the R curves did not cross the exclusion line to determine the correct fracture toughness values. Fracture toughness tests were repeated on 30% side grooved specimens to gather more data points to produce valid r curves.

However, from Figure 69 it can be seen that pre-straining does affect the fracture toughness data. For a given crack length Δa, the energy absorbed during fracture by the as received specimen is noticeably higher than that for pre-strained specimens. This may be due to the hardening of the material during pre-straining, leading to a higher yield strength and lower ductility.

C.1 As Received (0%)

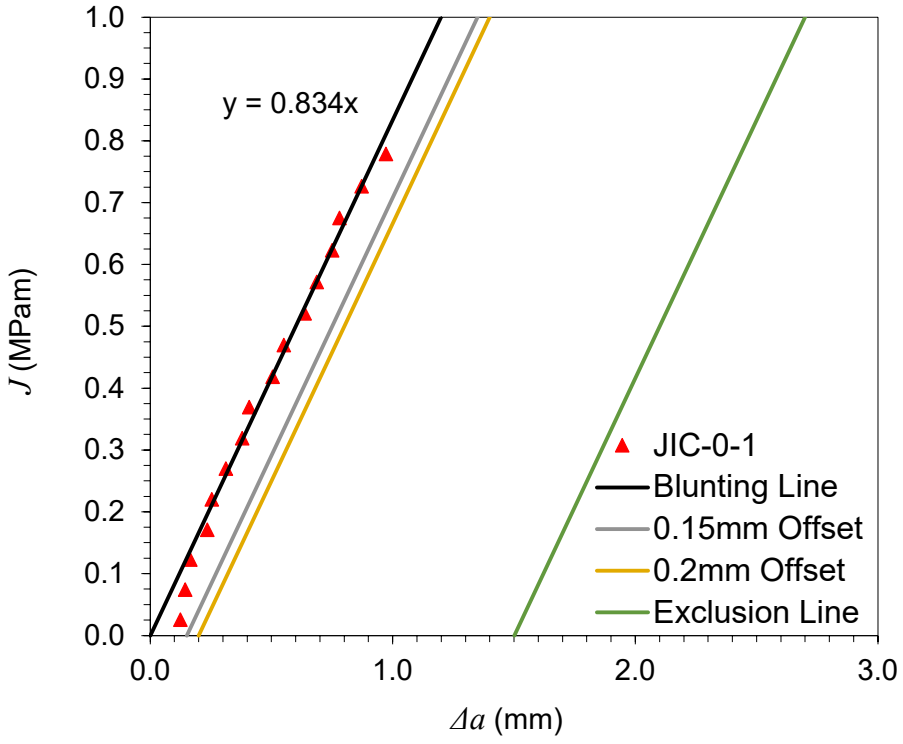

Figure 64 – R curve for as received material

C.2 5% Pre-Strain

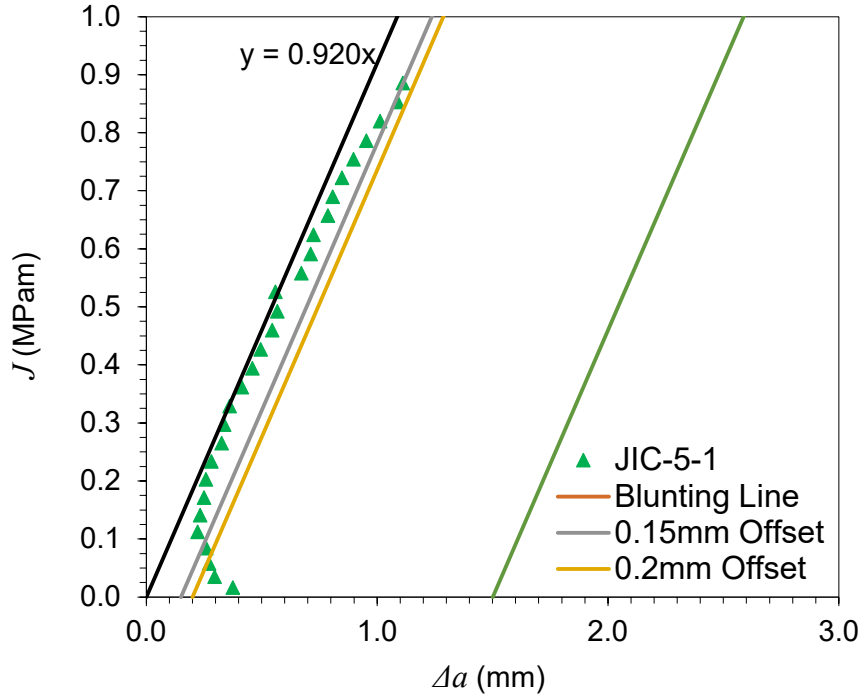

Figure 65 – R curve for 5% pre-strain

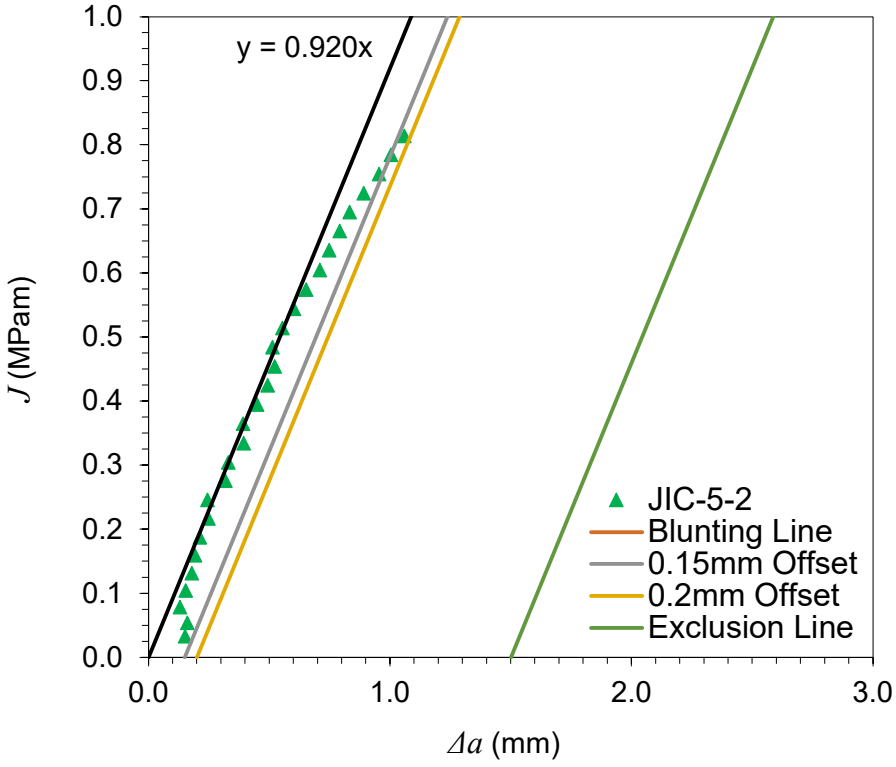

Figure 66 – R curve for 5% pre-strain

C.3 10% Pre-Strain

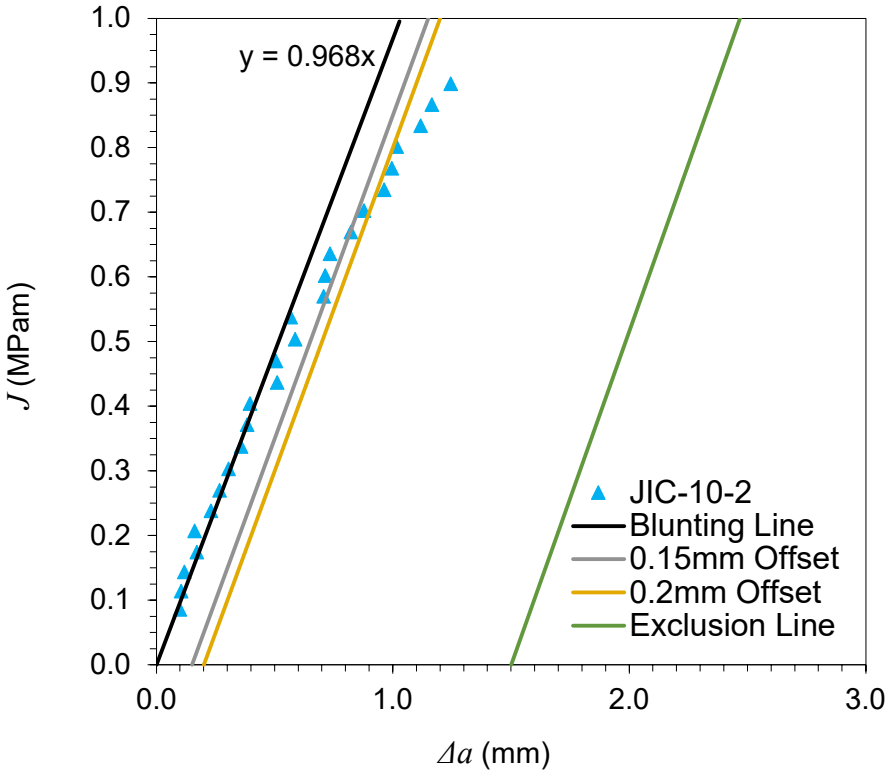

Figure 67 – R curve for 10% pre-strain

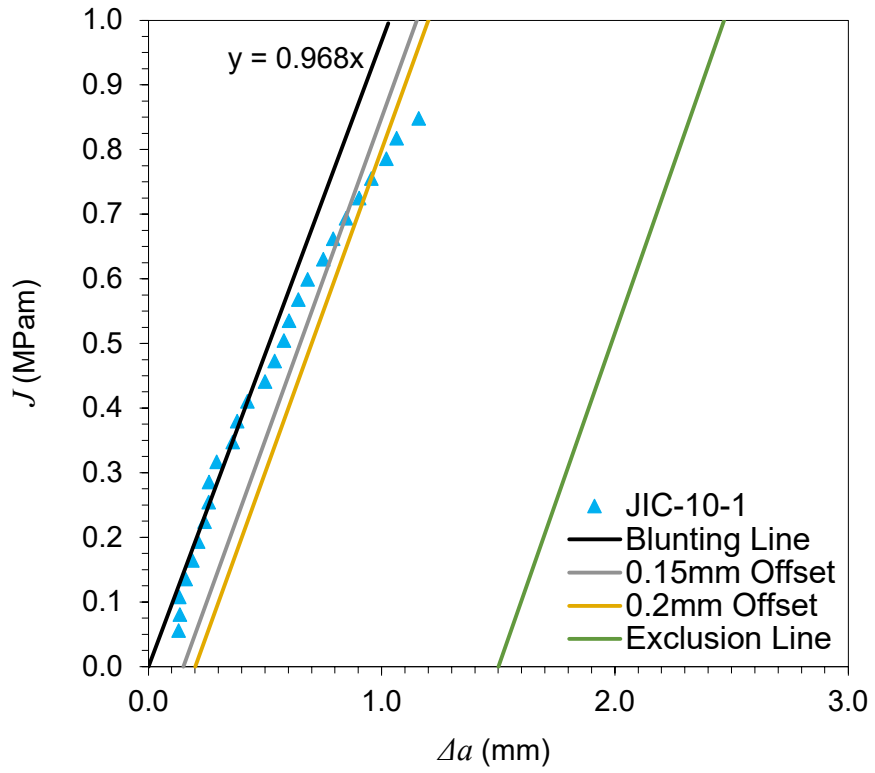

Figure 68 – R curve for 10% pre-strain

C.4 Comparison of R Curves

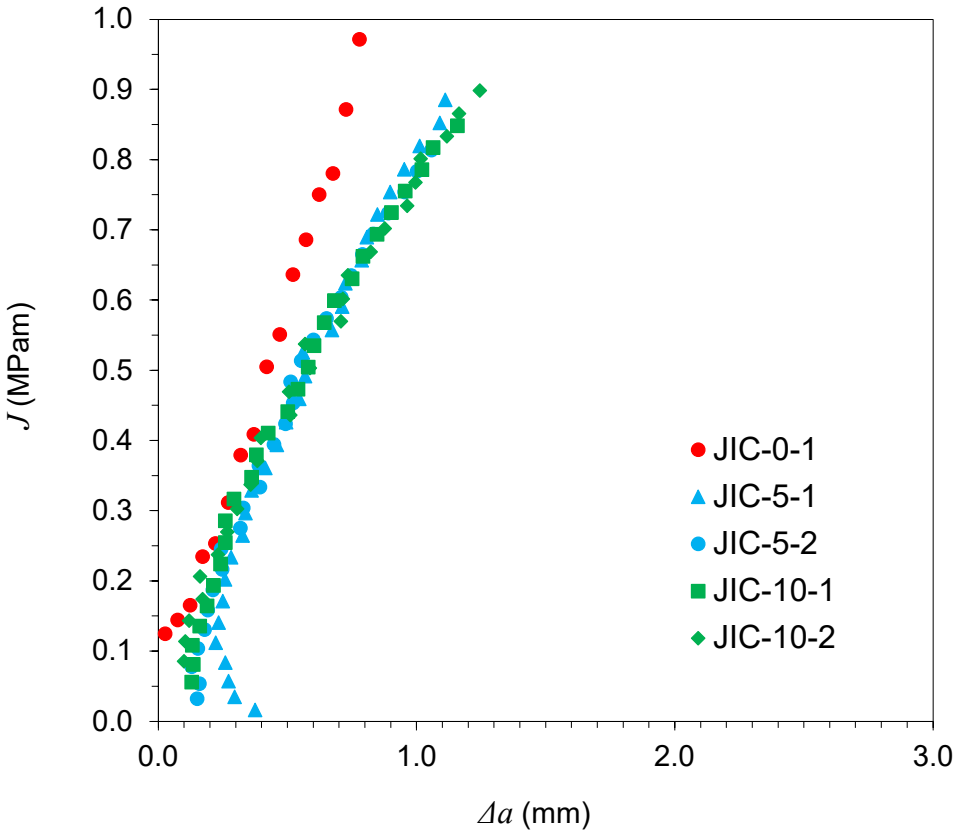

Figure 69 – R curves for as received, 5% and 10% pre-strained S355